BRUNEL UNIVERSITY LONDON

Advanced Signal Processing Techniques for Multimodal Ultrasonic Guided Wave Response

by

Sina Fateri

Submitted in fulfilment of the requirements for the degree of

Doctor of Philosophy

in the

Centre for Electronic Systems Research (CESR)

College of Engineering, Design and Physical Sciences

10.10.2015

BRUNEL UNIVERSITY LONDON

Abstract

College of Engineering, Design and Physical Sciences

Doctorate of Philosophy

By Sina Fateri

Ultrasonic technology is commonly used in the field of Non-Destructive Testing (NDT) of metal structures such as steel, aluminium, etc. Compared to ultrasonic bulk waves that travel in infinite media with no boundary influence, Ultrasonic Guided Waves (UGWs) require a structural boundary for propagation such that they can be used to inspect and monitor long elements of a structure from a single position.

The greatest challenges for any UGW system are the plethora of wave modes arising from the geometry of the structural element which propagate with a range of frequency dependent velocities and the interpretation of these combined signals reflected by discontinuities in the structural element. In this thesis, a technique is developed which facilitates the measurement of Time of Arrival (ToA) and group velocity dispersion curves of wave modes for one dimensional structures as far as wave propagation is concerned. A second technique is also presented which employs the dispersion curves to deliver enhanced range measurements in complex multimodal UGW responses. Ultimately, the aforementioned techniques are used as a part of the analysis of previously unreported signals arising from interactions of UGWs with piezoelectric transducers.

The first signal processing technique is presented which used a combination of frequency-sweep measurement, sampling rate conversion and the Fourier transform. The technique is applied to synthesized and experimental data in order to identify different wave modes in complex UGW signals. It is demonstrated that the technique has the capability to derive the ToA and group velocity dispersion curve of the wave modes of interest.

The second signal processing technique uses broad band excitation, dispersion compensation and cross-correlation. The technique is applied to synthesized and experimental data in order to identify different wave modes in complex UGW signals. It is demonstrated that the technique noticeably improves the Signal to Noise Ratio (SNR) of the UGW response using *a priori* knowledge of the dispersion curve. It is also able to derive accurate quantitative information about the ToA and the propagation distance.

During the development of the aforementioned signal processing techniques, some unwanted wave-packets are identified in the UGW responses which are found to be induced by the coupling of a shear mode piezoelectric transducer at the free edge of the waveguide. Accordingly, the effect of the force on the piezoelectric transducers and the corresponding reflections and mode conversions are studied experimentally. The aforementioned signal processing techniques are also employed as a part of the study. A Finite Element Analysis (FEA) procedure is also presented which can potentially improve the theoretical predictions and converge to results found in experimental routines. The approach enhances the confidence in the FEA models compared to traditional approaches.

The outcome of the research conducted in this thesis paves the way to enhance the reliability of UGW inspections by utilizing the signal processing techniques and studying the multimodal responses.

Key words *- (NDT), Ultrasonic Guided Wave (UGW), Dispersion Curve, Dispersion Compensation, Wave Mode Identification, Piezoelectric Transducer, Mode Conversion*

To Mum and Dad,

Mrs. Mitra Talebiyan & Mr. Manouchehr Fateri

Contents

List of Figures

List of Tables

List of Abbreviations

ACFM   *Alternating Current Field Measurement*

ASW   *Amplitude Sweep Wave form*

CCF   *Cross-Correlation Function*

DPI   *Dye Penetrant Inspection*

DFT   *Discrete Fourier Transform*

DTFT   *Discrete Time Fourier Transform*

ECT   *Eddy Current Testing*

FEA   *Finite Element Analysis*

FE   *Finite Element*

FSS   *Frequency Sweep Spectrum*

FFT   *Fast Fourier Transform*

FIR-LSIF   *Finite Impulse Response Least Squares Inverse Filter*

FSE   *Frequency-Sweep Examination*

IDC   *Iterative Dispersion Compensation*

JADE   *Joint Approximate Diagonalization of Eigen-matrices*

LDV   *Laser Doppler Vibrometer*

PZT   *Lead Zirconium Titanate*

MPI **M**agnetic **P**article **I**nspection

MLS **M**aximal **L**ength **S**equences

MRD **M**inimum **R**esolvable **D**istance

NDT **N**on-**D**estructive **T**esting

PEC **P**ulsed **E**ddy **C**urrent

SNR **S**ignal to **N**oise **R**atio

SCNR **S**ignal to **C**oherent **N**oise **R**atio

SH **S**hear **H**orizontal

SV **S**hear **V**ertical

SSP **S**plit **S**pectrum **P**rocessing

SVD **S**ingular **V**alue **D**ecomposition

TFR **T**ime-**F**requency **R**epresentations

ToA **T**ime of **A**rrival

TFSS **T**otal **F**requency **S**weep **S**pectrum

UGW **U**ltrasonic **G**uided **W**aves

UT **U**ltrasonic **T**esting

v_{ph} **P**hase **v**elocity

v_{gr} **G**roup **v**elocity

List of Symbols

p .... *Frequency-sweep number*

q .... *Numbering system for L(0,q) wave mode*

$\tilde{q}$ .... *Frequency increment, Hz*

R .... *Sampling rate conversion ratio*

R_{xx} .... *Auto-correlation function*

R_{yx} .... *Cross-correlation function*

R_{α} .... *Adaptive sampling rate conversion ratio*

t .... *Time, Sec.*

t_1 .... *Time of the final frequency, Sec.*

t_{FSE} .... *Lowest experienced rate converted time shift, Sec.*

t_{ToA} .... *Time of Arrival, Sec.*

t'_{FSE} .... *Maximum rate converted time shift, Sec.*

$\tilde{T}$ .... *Period of the signal, Sec.*

T' .... *Sampling time, Sec.*

T_s .... *Input sampling interval, Sec.*

T'_s .... *Output sampling interval, Sec.*

Δt_{FSE} .... *The shift between f_0 and adjacent vertical sample, Sec.*

u .... *Sample Signal*

u^R .... *Signal propagating forwards*

U_0 .... *Amplitude, V*

v_{gr} .... *Group velocity, m/Sec.*

v_{ph} .... *Phase velocity, m/Sec.*

w .... *Window function*

W_s .... *Windowed sine wave*

x .... *Distance, m*

z .... *Number of column in the matrix*

β . . . .*Numbering system for F(β,q)* wave mode

Θ_0 . . . . *Initial phase, Rads*

λ . . . .*Wavelength, m*

τ . . . . *Rate converted time, Sec.*

$\tilde{\tau}$ . . . .*STFT time, Sec.*

ω . . . .*Angular Velocity/Frequency, Rads/Sec.*

Statement of Original Authorship

The work contained in this thesis has not been previously submitted to meet requirements for an award at this or any other higher education institution. To the best of my knowledge and belief, the thesis contains no material previously published or written by another person except where due reference is made.

Signature: _____

Date: _____

Acknowledgements

"The passion for innovation never dies..."

Karl F. Benz, 1844-1929

Chapter 1

Introduction

1.1 Chapter overview

This introductory chapter delivers a brief report on the background to the rest of the thesis, including the motivation for research, basic concepts of Ultrasonic Guided Wave (UGW) inspection and its commercial applications. The general methodology implemented during the research and contributions to knowledge are described here. A list of publications arising from the Ph.D. is given and the thesis outline is provided to help guide the reader through the document.

1.2 Introduction

By definition, Non-Destructive Testing (NDT) is the testing of materials, for surface or internal flaws or metallurgical inconsistencies, without interfering in any way with the integrity of the material or its suitability for service. The most commonly used methods in industry are:

- Radiography

- Magnetic Particle Inspection (MPI)

- Dye Penetrant Inspection (DPI)

- Ultrasonic Defect Detection

    - Traditional Ultrasonic Testing (UT)

    - *Ultrasonic Guided Waves (UGW) testing*

- Electromagnetic Testing

  - Eddy Current Testing (ECT)

  - Pulsed Eddy Current (PEC)

  - Alternating Current Field Measurement (ACFM)

This thesis focuses on UGWs which have been used over the last few years to determine the health of industrial and structural components of varied geometries. Principally, UGWs have been used for detection of flaws, corrosion and metal loss. In the case of one dimensional structures[1] *e.g.* pipes, the features in the structure give rise to UGW reflections which can be used to estimate the parameters including *total cross sectional area* and *through wall depth* of the defect. One of the leading companies in UGW testing technology is Plant Integrity Limited (P_i, *a TWI company*)[2] which provides equipment and site-based inspection services to major industrial sectors, such as petrochemical industry, for inspection of critical pieces of infrastructure *e.g.* pipelines.

1.3   Motivation for research

The structural failure of one-dimensional geometries such as pipes, rods, bars, *etc.* can have disastrous consequences as follows,

- Posing health and safety risks to the public

- Explosions or escaped noxious gases in pipelines

- Causing damage to the environment

- Enormous financial costs from repairs, fines, *etc.*

It is therefore crucial that these geometries have an effective inspection method by which to inspect their integrity. Rods are used to meet a variety of demands in different fields, such as ground anchors, rock bolts, cables, cranes, bridges, elevators, concrete structures and electricity transfer networks. Throughout their

---

[1]Throughout the thesis 'one dimension structures' are considered as structures where the wave modes propagate along an axis of the waveguide. Therefore, one axis (one dimension) is dominant when the wave propagation is of concern. In this case, rods, bars, pipes, rails may be considered as one dimensional structures.

[2]Guided Ultrasonics Ltd. (GUL) and OLYMPUS Corporation are two other companies employing UGW technology for inspection of pipelines. Further information can be found in Section 1.4.1

service lifetime, these geometries are exposed to various operational effects which might cause damage to them. Fatigue damage, melting and corrosion cracking are types of defects caused by aging, stress, lightning strikes, wind-induced vibrations and environmental conditions [1], [2], [3], [4], [5].

Sixty-percent (%60) of the world's primary fuel is provided by oil and gas [6] which is transported in pipelines. They are manufactured and operated to well-established standards [7], because the products they carry can pose a major risk to the public and environment.

Figure 1.1 shows the Trans-Alaskan pipeline in the United States as an example. The failure of the pipeline poses a huge risk [8] to the environment and surroundings[3]. Consequently, good design and construction practices are required to maximize the structural integrity of pipelines in order reduce the majority of the aforementioned potential hazards. However, pipelines are threatened by defects and damage that occur in-service *e.g.* corrosion, erosion, cracks, *etc.* as they commonly operate in hostile environments (underground or subsea). These in-service defects are the major cause of pipeline failures [6] and inspecting pipelines for defects is a major concern for the oil and gas industry. UGW monitoring systems [9] permit the examination of the full volumetric shape of the pipelines for many metres (up to 100 m) from a single point of access.

One of the major concerns of the industry is providing a reliable and preferably automated technique for analysis of the structural integrity of these structures in order to avoid posing health and safety risks to the public, causing damage to the environment and huge financial costs [12]. UGW inspection is one of many NDT methods found to be suitable for this purpose and currently being used in several industrial sectors *e.g.* oil and gas. The commercial applications of UGW

Figure 1.1: An image of the Trans-Alaskan pipeline (left) and after failure (right) [10], [11]

---

[3]In 2007, severe internal corrosion resulted in failure of the Trans-Alaskan pipeline and leakage of over 200,000 gallons of crude oil into clean water. British Petroleum was obliged to pay a $12 million fine and $4 million as a community service payment.

technology and the current challenges are discussed in Sections 1.4.1 and 1.4.2.

1.4 Ultrasonic guided waves

UGW technology is used to perform NDT, which has a number of advantages over conventional UT. It offers a means by which long (up to 100 m), uniform elements of a structure, able to support the propagation of acoustic energy with minimal attenuation and can be assessed from a single position. UGW commonly operates at much lower frequencies (kHz range) with correspondingly longer wavelengths compared to conventional UT which operates in MHz range. In components of appropriate geometries where the thickness is of the same order as the wavelength (such as pipes), UGWs interact with the surfaces of the body and are bounded to propagate along the length of the specimen [13]. The Pulse-echo method is often used in both UT and UGW for *in situ* applications. The transducer excites a wave which propagates into the material, interacts with a discontinuity (*e.g.* defect), reflects back to the source where the signal is recorded. Pulse-echo UGWs have been effectively applied to the inspection of industrial pipelines, where defects such as gross corrosion can be detected up to 100 m from the transducer position [13]. Employing the UGW inspection technique can decrease maintenance costs and inspection time which is accordingly a reduction in services downtime.

1.4.1 Commercial applications of UGW

The most common commercial application of UGWs is the *in situ* inspection of industrial pipelines [4]. The equipment conventionally consists of three subsystems: the transducer array which encircles the pipe and is pneumatically forced against the surface by means of an inflatable bladder, the ultrasonic pulser-receiver, and the human interface often utilising a standard laptop/personal computer. Multiple rings (from 1 to 3 rings) of shear mode transducers [9] are placed around the pipe circumferentially (as illustrated in Figure 1.2) and a windowed[5] tone burst signal of normally between 20 and 100 kHz will be excited via the transducer. After the transducer excitation (pulse-echo technique), UGW propagates along the length of the pipe where the wave is sensitive to the changes in the pipe's cross sectional

---

[4]Recently the research has been expanded to other structures such as rods, bars, cables, plates, *etc.* where there is huge commercial interest in ultrasonic guided wave inspections for these applications.

[5]Hann and Hamming windows are normally used by Teletest Focus® for excitation in the *in situ* applications of pipelines

System Name	Developing Institution	Supplier	Transduction Method	Frequency Range
Teletest Focus®	TWI	Plant Integrity Ltd. (P_i)	PZT	20-100 kHz
Wave Maker®	Imperial College London	Guided Ultrasonics Ltd. (GUL)[6]	PZT	15-80 kHz
MsSR®	South West Research Institute (SWRI)	NDT Consultants Ltd.	Magnetostrictive coil	2-256 kHz
UltraWave LRT®	OLYMPUS corporation	Olympus Scientific Solutions	PZT	20-100 kHz

Table 1.1: Details of the available commercial equipment

area *e.g.* welds, defects, *etc.* These features of the pipe cause portions of incident wave to be reflected back to the transducer and/or mode converted into other types of wave modes, which can be recorded or stored for signal processing and further analysed.

The current state of the art of commercial implementations of UGW technology are summarized in Table 1.1. These products follow the same principles where pulse-echo techniques are used to monitor long distances of pipeline for corrosion, from a single access location. The Teletest®, Wavemaker® and OLYMPUS® systems share a common method of transduction, whereby a ring or multiple rings of Lead Zirconium Titanate (PZT)[7] transducers [9], [14], [15] covers the circumference of a pipe. The transducers are coupled to the surface with a pneumatic force applied by means of an inflatable air bladder around the array in order to provide traction for the shear transducer (see Figure 1.2). However, the MsSR® system employs magnetostriction for transduction on the pipe surface. An iron-cobalt alloy strip is

---

[6]MISTRAS Group Ltd. also employs UGWs to perform inspection of structures using GUL equipment (http://www.mistrasgroup.com/services/advancedndt/aut/gul.aspx).

[7]Lead Zirconium Titanate (PZT) is a ceramic perovskite material that exhibits the piezoelectric effect. The electric charge that stores in solid materials *e.g.* crystals in response to applied mechanical stress is called piezoelectricity which means the electricity produced as a result of pressure. The piezoelectric effect is a reversible process. The internal generation of a mechanical strain resulting from an applied electrical field (the inverse piezoelectric effect) is used in production of ultrasonic sound waves.

Figure 1.2: Teletest Focus® UGW monitoring system–Mk–4 [16], [17]

bonded around the pipe where a coil is then wrapped over the top of the strip [13]. This can be pulsed with very high currents to induce displacements in the strip and the reception can be achieved by the reversed process. The Teletest® UGW monitoring system was originally made for the inspection of pipelines however, different array designs using the same tool could be adopted for different types of structures *e.g.* linear transducer arrays for plates.

1.4.2 Current challenges

Although many recent techniques are evolving into promising inspection tools, several challenges still exist. The major challenges are listed as follows:

- UGWs tend to scatter energy when an additional coating layer is applied to the structure. In this case the rate of attenuation increases significantly, which may reduce the inspection range.

- UGW gives rise to multiple wave modes within its operating frequency region with a dispersive nature as their velocities can be frequency dependent. Dispersion degrades the resolution of the UGW response since it causes the signals to spread out in time/space and consequently contribute to the coherent noise.

- Signal interpretations are often difficult due to multimode propagation and mode conversion caused by the geometric features of the structure under investigation. These facts cause the signals to be superposed and consequently confuse the inspection.

These limitations influence system design, software adaptions and the inspection reliability which consequently affect the overall performance of UGW inspections [18].

1.5   Aims and objectives

Application of NDT plays a vital role in evaluating issues which may result in loss of life, economic costs and pollution. Since the UGW signal interpretations are often difficult due to multimodal propagation and mode conversion at the features of the structure under investigation, the overall aim of this research is to determine the cause of complex multimodal response and develop novel signal processing techniques in order to increase the resolution of the UGW inspection and monitoring systems. Therefore, the integrity of the structures could be measured with greater confidence allowing a more accurate prediction of remaining structural lifetime and consequently a reduction in structural integrity failure, pollution, *etc.* Specific objectives of the research were as follows:

- To investigate the current state of the art in signal processing for UGW testing of structures.

- To develop novel methods in order to enhance the resolution of UGW inspection.

- To develop novel methods in order to identify the wave modes of interest in multimodal UGW signal.

- To incorporate the findings into an algorithm that paves the way for wave mode identification.

- To study the behaviour of the UGWs interacting with the piezoelectric transducers.

- To make appropriate recommendations for future studies of the subject.

1.6   Research methods

As discussed in Section 1.4.2, in the context of *current challenges*, the signal inter-
pretations are often challenging due to multimodal propagation nature of UGWs
and mode conversions. A signal processing technique is therefore developed using
the combination of sampling rate conversion, Fourier transform and the concept of
Frequency Sweep Spectrum (FSS) to identify different wave modes in a complex
UGW response including several superposed signals. Specifically, accurate quan-
titative information such as: total number of existing wave modes in a particular
frequency range, number of constituent wave-packets in a superposed signal, group
velocity of a wave mode by extracting the ToA are provided by the application of
the technique. Thus the extraction of the aforementioned quantitative informa-
tion can ease the detection process of geometric features of the structure under
investigation. The technique employs multiple cycle Hann windowed sinusoidal
pulse train excitations at a range of UGW frequencies which are equally incre-
mented. It proposes to identify signals with similar group velocities but different
gradient of group velocity dispersion curve arising from independent wave modes.
It is shown that the rate converted time shift, caused by sampling rate conversion
for each signal, can adjust their operating frequency to the frequency of interest.
Consequently, this promotes sequential rate converted time shifts to the individual
acquisitions at each frequency increment. Hence, the technique can exploit the
different rates of shift in rate converted time which facilitates the identification of
different wave modes in the superposed signals. It is also best suited for one dimen-
sional structures *e.g.* rods, bars, pipes, rails, *etc.* as it requires frequency-sweep
measurements using the pulse echo technique.

Another signal processing technique is presented using a broadband chirp excita-
tion, dispersion compensation and cross-correlation. The technique is also applied
to synthesized and experimental data in order to identify different wave modes in
complex UGW signals. It is demonstrated that the technique noticeably improves
the SNR of the UGW response. It is also able to derive accurate quantitative infor-
mation about the ToA and consequently the propagation distance. This proposed
technique in this study combines the dispersion compensation technique with pulse
compression where the dispersed signals are iteratively compensated for dispersion
for a range of propagation distances. Then the compensated signals are cross-
correlated with the excitation signal in order to extract the correct propagation
distance.

Furthermore, after the development of the aforementioned signal processing tech-

niques, some unwanted wave-packets were identified which were reported and investigated in detail. Unlike the recent studies that were mainly focused on the mode conversion of longitudinal and/or torsional wave modes from defects, joints, thickness variations, *etc.* the main attention has been given to the possible reflections and mode conversions from the source of UGW excitation *i.e.* the coupled transducer. Therefore, the reflections and mode conversions of UGWs from the transducers were investigated and studied via Finite Element Analysis (FEA), experimentation and 3D Laser Doppler Vibrometry (3D-LDV) scans. It is shown that considerable amount of reflections and mode conversions can occur due to the presence of the coupled transducers thus may potentially become a disruptive matter in field inspections and contribute to the coherent noise. According to the published literature, these reflections and mode conversions from the transducers have not been studied and/or reported in the field of UGW.

Two types of FEA approaches are used to investigate the reported phenomenon: initially using a single point/node of excitation and ultimately a 3D-geometric transducer excitation which was developed concurrently by S. Lowe and published in [**SF 05**]. Currently the FEA approach for UGW propagation is performed using selected nodes in the geometry which simulates a 'point excitation'. In laboratory experiments UGW excitations are applied using piezoelectric transducers which have different acoustic impedance and material properties to the waveguide, however; the nodes in FEA have the same acoustic impedance and material properties. An alternative approximation by using a 3D-geometric transducer excitation for an accurate UGW response is discussed.

1.7 Contributions to knowledge

The objectives have been achieved using a combination of laboratory experiments, Finite Element (FE) modelling to evaluate the propagation of UGWs through the waveguide. The characteristics were studied and signal processing techniques were researched, leading to two distinct contributions to knowledge in signal processing. During the technique implementation, unwanted wave-packets appearing in the UGW response were reported and investigated in depth which led to two other contributions to knowledge in guided wave reflection and mode conversion from coupled transducers. The detailed description of the contributions are listed below,

1. A novel signal processing technique to identify wave modes in multimodal UGW signals. This method shows promise for structural feature detection in

complex UGW inspections. It has been empirically demonstrated that the proposed technique is useful for Time of Arrival (ToA) extraction and wave mode identification of superposed UGWs. The technique obtains the number of present wave modes with accurate quantitative information allowing a portion of the group velocity dispersion curve to be computed.

2. A novel signal processing technique has been developed using broadband excitation, dispersion compensation and cross-correlation. The technique considerably improves the SNR of the UGW response and enables the extraction of the ToA and propagation distance of individual wave modes using *a priori* knowledge of the group velocity dispersion curve. The technique was quantitatively compared with the technique described above and useful recommendations are given for the *in situ* applications of UGWs.

3. Report and study of coupling dependent guided wave reflections and mode conversions from coupled transducers. It was demonstrated that the coupled piezoelectric transducers can cause reflection and mode conversion which may potentially add extra challenge to signal interpretations by contributing to the coherent noise. The phenomenon was studied in depth using FEA parametric studies and various experimental procedures. Useful recommendations are given for the field inspections of pipelines and future research directions are clarified.

4. In order to model the aforementioned phenomenon, an FEA procedure was proposed to study the coupling dependant reflections and mode conversions. The FE model proposes an approach which is shown to enhance the accuracy of the modeling-based UGW response therefore reaching a closer agreement between the theoretical predictions and experimental results.

1.8 Organisation of thesis

Chapter 2 provides an overview of the fundamentals of the elastic waves, UGWs and related concepts *e.g.* dispersion phenomenon, mode conversion, *etc.* This chapter also covers the fundamentals of signal processing for UGWs. Chapter 3 covers the developers of UGW and the recent published literature on signal processing in the field. Two novel signal processing techniques for wave mode identification in multimodal UGW signals are presented in Chapter 4 and Chapter 5. The performances of the two proposed techniques are quantitatively compared

and useful recommendations are given for the *in situ* applications in Chapter 5. The coupling dependent reflections and mode conversions from transducer coupling was reported and studied on an aluminium rod in Chapter 6. This has been further investigated on pipe applications within this chapter. The conclusions of the research are then discussed in Chapter 7, where the contributions to the knowledge are thoroughly reviewed in the wider context of the published literature, before the recommendations for future research work.

1.9 Publications arising from the Ph.D.

Journal papers:

[**SF 01**] S. Fateri, N. V. Boulgouris, A. Wilkinson, W. Balachandran, "Frequency-Sweep Examination for Wave Mode Identification in Multimodal Guided Wave Signal," *IEEE Transactions on Ultrasonic, Ferroelectric and Frequency Control (IEEE-TUFFC)*, vol. 61, no. 9, pp. 1515-24, 2014.

[**SF 02**] S. Fateri, S. Lowe, B. Engineer, N. V. Boulgouris "Investigation of Ultrasonic Guided Waves," *IEEE Sensors Journal,* vol. 15, no. 8, pp. 4319-28, 2015.

[**SF 03**] S. Fateri, M. K. Yucel, M. Legge, A. Wilkinson, "An Iterative Dispersion Compensation Technique for Chirp Based Multimodal Ultrasonic Guided Waves," *Submitted to IEEE Transactions on Ultrasonic, Ferroelectric and Frequency Control (IEEE-TUFFC),* 2015.

[**SF 04**] S. Fateri, N. V. Boulgouris, A. Wilkinson, "A Two Dimensional Fast Fourier Transform for Guided Wave Analysis," *The Journal of British Institute for Non-Destructive Testing Insight,* vol. 56, no. 9, 2014.

[**SF 05**] S. Lowe, S. Fateri, R. Sanderson, N. V. Boulgouris, "Finite Element Modelling of the Interaction of Ultrasonic Guided Waves with Bonded Piezoelectric Transducers," *The Journal of British Institute for Non-Destructive Testing (BINDT)- Insight*, vol. 56, no. 9, 2014.

[**SF 06**] M. K. Yucel, S. Fateri, M. Legg, A. Wilkinson, V. Kappatos and T-H. Gan, "Coded Wave Forms for High Resolution Ultrasonic Guided Wave Response," Accepted in *IEEE transactions on Industrial Informatics*, July, 2015.

Conference papers:

[**SF 07**] M. K. Yucel, S. Fateri, M. Legge, A. Wilkinson, V. Kappatos and T-H. Gan, "Pulse Compression Based Iterative Time of Flight Extraction of Dispersed Ultrasonic Guided Waves," *IEEE International Conference on Industrial Informatics (INDIN)*, Cambridge, United Kingdom, July, 2015.

[**SF 08**] S. Fateri, N. V. Boulgouris, "Inspection of Defects Near Welds in Cylindrical Structures," in *The Young Welding International Conference (YPIC)*, Budapest, Hungary, Sept. 2014.

[**SF 09**] S. Fateri, "Wave Mode Identification in Long Range Ultrasonic Inspections using Incremental Frequency Examination," in *7th Annual Student Research Conference*, Brunel University London, United Kingdom, June 23-26, 2014.

[**SF 10**] S. Fateri, N. V. Boulgouris, P. Mudge, "A Two Dimensional Fast Fourier Transform for Guided Wave Analysis," in *American Society for Non-Destructive Testing (ASNT)* 23rd *Research Symposium*, Minneapolis, United States of America, March 24-27, 2014.

[**SF 11**] S. Fateri, "An Automatic Mode Separation Technique for Multimodal Guided Wave Analysis," in 1st *International Conference on Welding and Non-Destructive Testing*, Karaj, Iran. February 25-26, 2014.

[**SF 12**] S. Fateri, "Wave Mode Separation in Long Range Ultrasonic Inspections," in *6th Annual Student Research Conference*, Brunel University, London, United Kingdom, June 23-26, 2013.

Note: These publications are referred to in the thesis by the 'SF XX' labelling system indicated above, so as to help highlight their presence throughout the thesis.

Chapter 2

Background Theory of Ultrasonic Guided Waves

2.1 Chapter overview

This chapter covers the theoretical background necessary for the following chapters. It provides the reader with the principles of elastic waves and UGWs which are repeatedly referred to throughout the thesis. The fundamental background of signal processing in UGWs is covered within this chapter. This is required for Chapters 4 and 5 which introduce novel signal processing techniques for wave mode identification in multimodal UGW signals. In addition, it covers the basic definition for wave propagation, dispersion and mode conversion phenomenon which are necessary for Chapter 6 reporting and studying the coupling dependant guided wave reflection and mode conversion from transducer coupling.

2.2 Fundamentals of elastic waves

Unlike the electromagnetic wave that is capable of transmitting energy through a vacuum i.e. empty space, mechanical waves require media to transmit its energy from one location to another. Elastic waves are mechanical waves propagating in an elastic medium. This type of propagation initiates from the effect of forces related to volume deformation and shape deformation of medium elements. Wave sources can cause these deformations and movements of medium particles; however this does not result in matter transport.

Wave propagation may vary in character depending on boundaries of an elastic medium. Bulk waves (longitudinal and shear waves) propagate in infinite media.

Surface waves (Rayleigh waves and Love waves) propagate in a three dimensional medium bounded by one surface. Seismic wave phenomenon can be described by propagation of bulk waves and surface waves traveling through the Earth's surface layer.

The interaction of compression and shear waves in a bounded elastic medium with two equidistant surfaces results in the generation of Lamb waves. There are also waves that propagate on media boundary (interface waves) with names derived from their discoverers: in the interface between two solids Stoneley waves propagate, while in the one between a solid and a liquid Scholte waves propagate [19].

2.3 Ultrasonic guided waves

The term 'ultrasonic guided wave' is commonly used when a free boundary restricting an elastic body guides and drives waves. These waves are widely used in NDT. The name of the guided wave is dependent on the medium type and the way energy is transmitted through the medium. The general and specific terminologies [20] are provided in Table 2.1 and Table 2.2.

2.3.1 Longitudinal waves

Longitudinal waves are known as compression, pressure, primary or P waves. Longitudinal waves are categorized by alternating particle motion (*i.e.* compression and stretching character). Figure 2.1 illustrates a sample longitudinal particle motion. It can be observed that the direction of medium line movements representing medium motions is parallel to the direction of wave propagation. These waves in cylindrical structures such as pipe, rod, *etc.* appear as $L(0, i)$, $i = \{1, 2, \ldots\}$ where $L(0, 1)$ [21] is the fundamental longitudinal wave in these types of structures.

Generic terminology	Boundary specific	Structure specific
Ultrasonic Guided Waves	Surface waves	Plate waves
Long Range Ultrasound	Interface waves	Rod waves
		Cylindrical waves

Table 2.1: General guided wave terminologies

Plate Waves	Cylindrical Waves	Interface Waves
Lamb	Longitudinal	Stoneley
Axisymmetric	Flexural	Scholte
Anti-Symmetric	Torsional	Love
Compressional		
Shear Horizontal/Vertical		

Table 2.2: Specific guided wave terminologies

2.3.2 Shear waves

Shear waves are also known as transverse, secondary or S waves. Shear waves are categorized by transverse particle movements in interchanging direction where the direction of particle movements is perpendicular to the direction of propagation. The particle movements in plate like structures can occur horizontally (Shear Horizontal wave, SH; Figure 2.2 (a)) or vertically (Shear Vertical wave, SV; Figure 2.2 (b)). These waves in cylindrical structures such as pipe, rod, *etc.* appear as $T(0,i)$, $i = \{1, 2, \ldots\}$ where $T(0,1)$ is the fundamental torsional wave in these types of structures.

2.3.3 Rayleigh waves

Rayleigh waves (Figure 2.2 (c)) are categorized by elliptical particle motions in the xy vertical plane and motions parallel to the direction of propagation along the
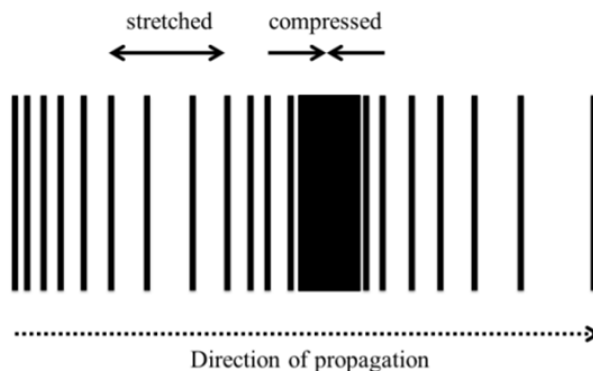
Figure 2.1: Distribution of displacements for a compressional wave, line density represents amplitude

x-axis. A simple example of this type wave is sea wave. Rayleigh waves propagate along surfaces of elastic media of thickness many times greater than the wave amplitude where amplitude of the elliptical particle motions decreases with depth y [19].

2.3.4 Love waves

Love waves (Figure 2.2 (d)) are categorized by particle motions comprising interchanging transverse movements. The direction of medium particle motions is horizontal in the xz-plane and perpendicular to the direction of propagation. The wave amplitude decreases with depth which is similar to Rayleigh waves in this case.

2.3.5 Lamb waves

These waves were named after the discoverer, Horace Lamb. He developed the theory of Lamb wave propagation in 1917 [22]; but unfortunately was not able to generate the waves he discovered in practice. This was accomplished by Worlton [23], who also remarked upon their potential use for damage detection in structures[8].

Lamb waves arise as a result of superposition of multiple reflections of longitudinal and shear (SV) waves from the bounding surfaces of an infinite extent media. Particle motions of these waves are often complex. In plate like structures, two forms of Lamb waves can be generated *i.e.* symmetric denoted as $S_0, S_1, \ldots$ and anti-symmetric, denoted as $A_0, A_1, \ldots$ and the numbers of these forms are infinite depending on the frequency. Figure 2.2 (e) and (f) illustrates the fundamental symmetric (S_0) and anti-symmetric (A_0) Lamb wave modes respectively. Non-axisymmetric waves in cylindrical structures such as pipe, rod, *etc.* are called *flexural waves*. They appear as $F(\beta, q)$, $\beta = \{1, 2, \ldots\}, q = \{1, 2, \ldots\}$ where $F(1, 1)$ is the fundamental flexural wave in these types of structures.

---

[8]Further information of damage detection studies based on the previous published literature is covered in Chapter 3 in the context of *Literature Survey for Ultrasonic Guided Wave Technology.*
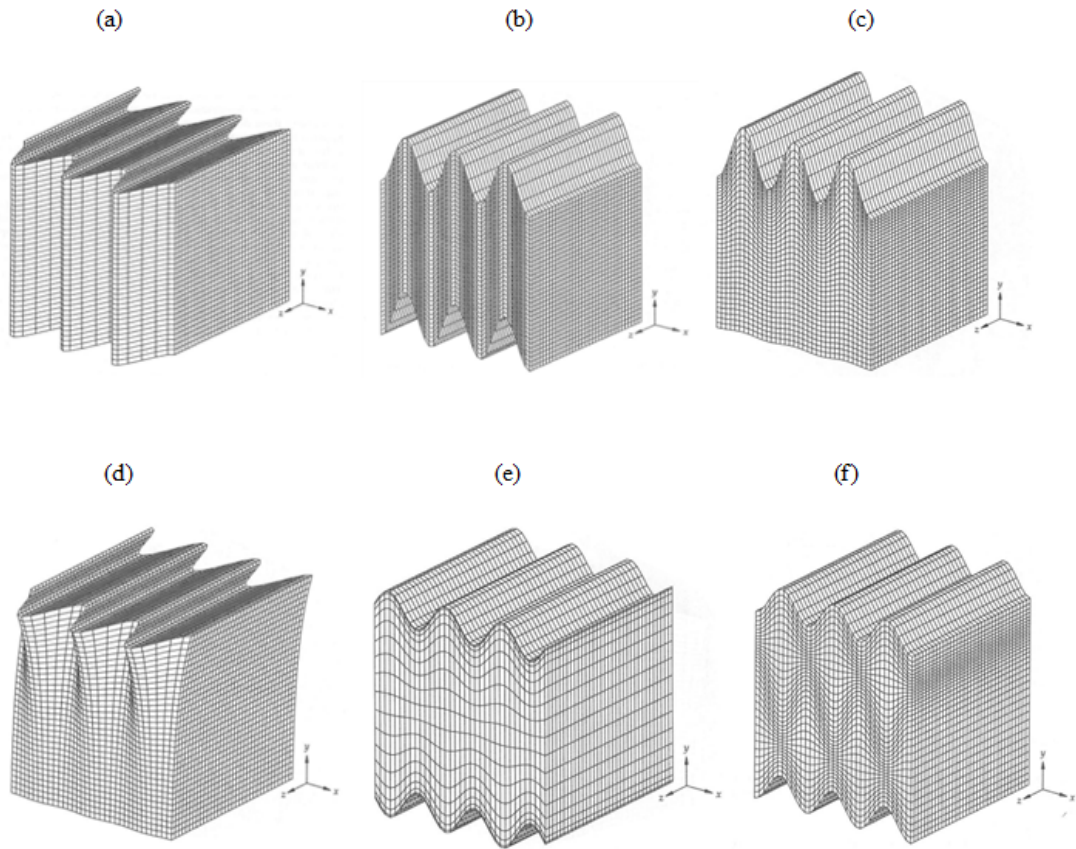
Figure 2.2: Distribution of displacements for the (a) fundamental horizontal shear wave, (b) fundamental vertical shear wave, (c) Rayleigh wave (d) Love wave (e) fundamental symmetric mode of Lamb wave and (f) fundamental anti-symmetric mode of Lamb waves [19]

2.4   Basic definitions of elastic waves

A specific case of a wave as a harmonic initial disturbance can be considered as [19]:

$$u(x,0) = U_0 \cos(kx) \tag{2.1}$$

where k represents wavenumber or the spatial frequency, in (2.2) λ represents wavelength or the spatial period of disturbance and is defined as:

$$\lambda = 2\pi/k \tag{2.2}$$

So, (2.1) can be expressed in a general form as [19]:

$$u(x,t) = \frac{U_0}{2} \left[\cos(kx - \omega t) + \cos(kx + \omega t) \right] \tag{2.3}$$

where U_0 is the amplitude and ω is angular frequency. The first term in square brackets defines the wave propagating to the right/forwards, and the second term defines the wave propagating to the left/backwards.

Assuming that a wave $u^R(x,t)$ is propagating forwards:

$$u^R(x,t) = \frac{U_0}{2} \cos(kx - \omega t) \tag{2.4}$$

The phase of this wave is $\Phi = kx - \omega t$. For the movement of a point with constant phase $kx - \omega t = const$ it is $x = (\omega/k)t + const$. Thus, a point of constant phase moves with velocity:

$$v_{ph} = \omega/k \tag{2.5}$$

The harmonic wave propagating to the right with velocity v_{ph} is presented in Figure 2.3.

2.4.1 Dispersion relation, dispersive and non-dispersive waves

The dependency $\omega(k)$ or the frequency dependant velocity is the so-called dispersion relation. The phase velocity refers to the relationship between spatial frequency k and angular frequency ω of the waves. In the case of non-dispersive waves, this relation is linear *i.e.* $\omega(k) = kv_{ph}$ in a non-dispersive medium, thus the phase velocity possesses a constant value for the entire frequencies.

In addition to the phase velocity, the group velocity is likewise related to wave propagation which refers to the propagation of a group of waves called a wave-
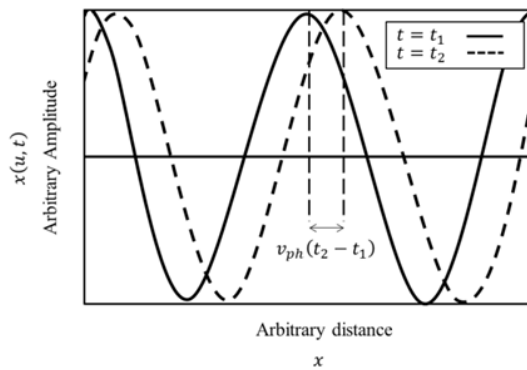
Figure 2.3: Wave propagating with phase velocity (v_{ph})

packet [19].

Assuming that two waves propagating to the right, having the same amplitude, but different frequencies and wave number:

$$u(x,t) = U_0 \left[\sin(k_1 x - \omega_1 t) + \sin(k_2 x - \omega_2 t) \right] \tag{2.6}$$

Therefore, (2.6) can also be expressed as:

$$u(x,t) = 2U_0 \cos\left(\frac{k_1 - k_2}{2} x - \frac{\omega_1 - \omega_2}{2} t \right) \sin\left(\frac{k_1 + k_2}{2} x - \frac{\omega_1 + \omega_2}{2} t \right) \tag{2.7}$$

According to (2.7), the wave packet could be expressed as:

$$u(x,t) = 2U_0 \underbrace{\cos\left(\Delta k x - \Delta \omega t \right)}_{\text{Modulating Wave}} \underbrace{\sin\left(k_0 x - \omega_0 t \right)}_{\text{Carrier Wave}} \tag{2.8}$$

According to (2.8), the wave packet was defined as a modulation of a carrier wave and a modulating wave in the form of a window. Further descriptions of the windowed waves are presented in Section 2.5.1.

The propagation velocity of a modulating wave defines the propagation velocity of a wave packet. Assuming a constant phase:

$$\Delta k x - \Delta \omega t = const \tag{2.9}$$

i.e.

$$x = \left(\Delta \omega / \Delta k \right) t + const \tag{2.10}$$

Thus, the group velocity could be expressed as:

$$v_{gr} = d\omega / dk \tag{2.11}$$

It is notable that for a non-dispersive medium, the group velocity will be equal to the phase velocity. However, in a dispersive medium these velocities vary, which deforms the wave packet during propagation. Thus, the amplitude of the wave packet decreases and the wave packet spreads over time/space. Parameters effecting the dispersion are further discussed in details in Chapter 3 in the context of *Literature Survey for Ultrasonic Guided Wave Technology.*

2.4.2 Dispersion curves

Dispersion curves deliver useful quantitative information to any UGW inspection system. A dispersion curve diagram illustrates the frequency or wavenumber relation to the wave velocity in separate curves for existing wave modes in a frequency region. These are curves of the variation in phase and group velocity (v_{ph}, v_{gr}) over a range of frequencies for each wave mode. The phase velocity dispersion curve for a non-dispersive mode over a particular frequency range, will be flat (constant value) over that bandwidth, therefore, v_{ph} will be quite close to v_{gr} [15]. On the other hand, as was described in Section 2.4.1, dispersive signals have a tendency to spread out over time and space as the phase will be travelling with a different velocity (v_{ph}) to the envelope (v_{gr}) according to their dispersive nature and having frequency dependent velocity. Figure 2.4 represents a phase and group velocity dispersion curve for *8 mm diameter Aluminium rod* plotted by DISPERSE software designed and developed by Imperial College London [24]. The wave modes labelled in Figure 2.4 are designated based on the notations specified by Meitzler in 1961 [21]. Further descriptions for the notations are given in Chapter 3.

2.4.3 Mode conversion of UGWs

The energy of sounds propagating in media can be converted from one form into another form. Mode conversion takes place when a wave encounters a boundary between materials of different acoustic impedances and/or the incident angle is not normal to the interface [25]. For instance, when a longitudinal wave hits an interface at an angle, some of its energy can cause particle movement in the transverse direction to start a shear wave. In addition, when sound waves move across
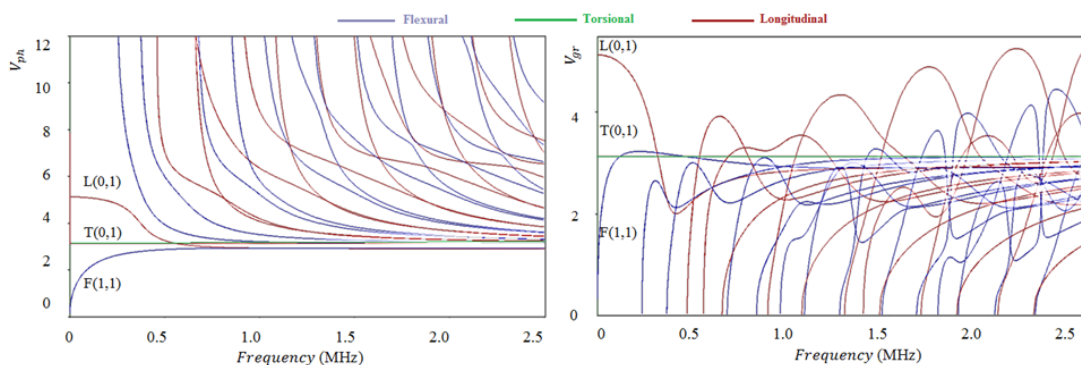
Figure 2.4: Phase (left) and group velocity (right) dispersion curve for *8 mm diameter aluminium rod*

a boundary between materials having different acoustic velocities, refraction takes place at that boundary. The larger the difference in acoustic velocities between the two materials, the more the sound is refracted. Shear waves are not refracted as much as the longitudinal waves due to traveling slower than longitudinal waves. Therefore, the velocity difference between the incident longitudinal wave and the shear wave is not as great as it is between the incident and refracted longitudinal waves.

For UGWs, mode conversion often occurs when a wave-packet encounters a discontinuity and converts into a wave mode with different velocity and displacement characteristic. For example, when a $T(0, 1)$ wave-packet encounters a discontinuity, it will be reflected and converted to its own family of higher order flexural wave modes, $F(\beta, 2)$ at the frequency range of interest.

2.5 Signal processing for UGWs

Signal processing deals with the analysis of signals in the time and space platforms to facilitate better interpretation of the signal. The UGW signals could be pre-processed and/or post-processed before and/or after the inspections. Here, the fundamental of signal processing for UGWs are briefly discussed. The literature review for the signal processing and the recent published research works in the field is thoroughly covered in Chapter 3.

2.5.1 Windowing/ Modulating sine waves

As was defined in (2.7) and (2.8), the wave packet is a superposition of a carrier wave and a modulating wave in the form of a window. Window functions are normally used to reduce the effect of the spectral leakage in frequency domain and restricting the dispersion. Hann window is commonly used in UGW inspections as was justified by Cawley and Alleyne[9] [26]. The thorough description and comparison of different window functions were covered by Nuttal [27]. Accordingly, Hann windowed sine waves were used, in order to implement the research methodology presented throughout the thesis (Chapter 4 and Chapter 6).

This window function was named after the Austrian meteorologist Julius Von Hann. The discrete window function can be defined as:

---

[9]The generation of pure modes requires controlling the excitation bandwidth in both the frequency and wavenumber domains. This is attained in the frequency domain using a tone-burst enclosed in a Hann window as illustrated in Figure 2.5

$$w(t) = 0.5 \left(1 - \cos\left(\frac{2\pi t}{\tilde{L} - 1} \right) \right), 0 \leq t \leq \tilde{L} - 1 \tag{2.12}$$

where $\tilde{L}$ is the window length.

Thus the windowed sine wave could be defined as:

$$W_s(t) = (\sin(\omega t)) \left(0.5 \left(1 - \cos\left(\frac{2\pi t}{\tilde{L} - 1} \right) \right) \right), 0 \leq t \leq \tilde{L} - 1 \tag{2.13}$$

Figure 2.5 illustrates the Hann window, 10-cycle sinusoidal tone burst and the windowed sine in time and frequency domain separately. Since a Fourier Transform assumes periodicity, any cut-off between the last sample and the repeated first sample will result in artefacts in the frequency spectrum (*e.g.* "smearing" of the peaks in Figure 2.5–(right) which is known as spectral leakage. To reduce the effect of spectral leakage a window function could be used which smooths out any such discontinuity and thereby reduces artefacts in the spectrum.

2.5.2 Cross-correlation and auto-correlation

Cross-correlation is a measure of similarity between two signals, while autocorrelation is a measure of how similar a signal is to itself [28]. The autocorrelation function of a signal refers to the reliance of the values of samples at one time on the values of the samples at another time [29].

The autocorrelation function of sampled signal, $x(n)$ can be defined (biased or unbiased) as, Un-Biased:
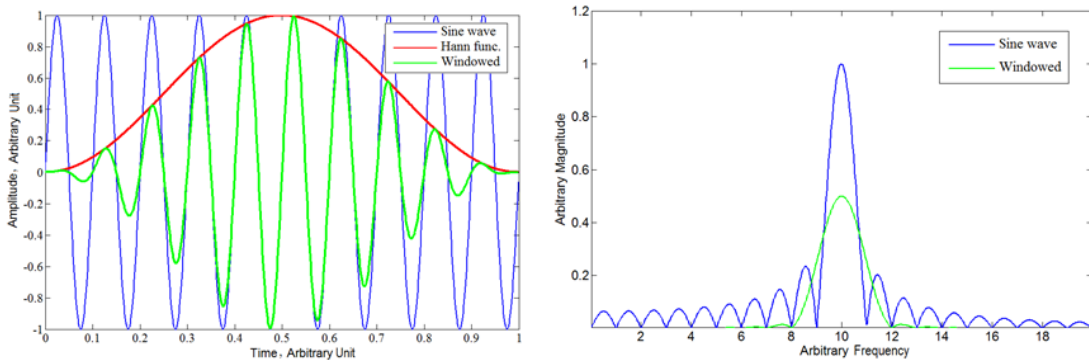
Figure 2.5: (left) time domain Hann window, truncated sine wave and windowed, (right) frequency spectrum of the sine wave and its windowed version

$$R_{xx}(m) = \frac{1}{\tilde{N} - |m|} \sum_{n=1}^{\tilde{N}-\tilde{M}+1} x(n)x(n+m-1) \tag{2.14}$$

and biased:

$$R_{xx}(m) = \frac{1}{\tilde{N}} \sum_{n=1}^{\tilde{N}-\tilde{M}+1} x(n)x(n+m-1) \tag{2.15}$$

$$m = 1, 2, \ldots, \tilde{M} + 1$$

where $\tilde{M}$ is the number of lags.

However, the dependence of the values of one signal on another signal can be computed by the cross-correlation function defined in (2.16):

$$R_{yx}(m) = \frac{1}{\tilde{N}} \sum_{n=1}^{\tilde{N}-\tilde{M}+1} y(n)x(n+m-1) \tag{2.16}$$

$$m = 1, 2, \ldots, \tilde{N} + 1$$

where $\tilde{N}$ is the number of samples.

2.5.3 The pulse compression technique

Pulse compression is a widely used technique [30], [31], [32][10] which correlates the received signal with the modulating transmitted signal and results in a compressed pulse. For the proper exploitation of the technique, a signal with a good autocorrelation function, denoted as $(CCF(_{x(t),x(t)}) \cong \delta(t))$ is required [33]. Signals satisfying desired autocorrelation condition that have been commonly used are linear/non-linear chirped sinusoids or pseudorandom binary sequences. Barker codes, Maximal Length Sequences (MLS), Gold Codes, Golay Codes, Chaos Sequence and Legendre Sequence are examples of pseudorandom binary sequences used in the literature [34]. In Chapter 5, linear chirp signals are employed as a part of the novel signal processing technique. Therefore, the next part provides brief information on chirp signals.

---

[10]Pulse compression is mainly applied to radar, sonar, echography and telecommunication applications to increase range resolution (angular resolution or spatial resolution) as well as signal to noise ratio.

Chirp

Chirped sinusoids are broadband signals which are created and tailored according to the frequency components desired in the signal. Chirp signals might have positive or negative chirp rates (*i.e.* frequency increases or decreases with time) and could have quadratic or linear characteristics. Since linear chirp signals are used in this study, a generic linear chirp equation is given as [35], [36]:

$$x(t) = \cos\left(\theta_0 + 2\pi(f_0 t + (\tilde{k}/2)t^2)\right) \tag{2.17}$$

where θ_0 is the initial phase, f_0 is the starting frequency and $\tilde{k}$ is the chirp rate, which is given as,

$$\tilde{k} = \frac{f_1 - f_0}{t_1} \tag{2.18}$$

where f_1 is the final frequency of the chirp and t_1 is the corresponding time of the final frequency. A chirp example with its auto-correlation function is illustrated in Figure 2.6–(a) and Figure 2.6–(b).

2.5.4 Sampling rate conversion

Generally, an input signal may perhaps be sampled at some specified sampling period T and the aim is to convert this sampled signal to a new sampled signal at a different sampling period T' such that the resulting signal corresponds to the same analog function. The process of digitally changing the sampling rate of a signal from a given sampling rate/frequency $F = 1/T$ to a different rate/frequency $F' = 1/T'$ is called sampling rate conversion [37].
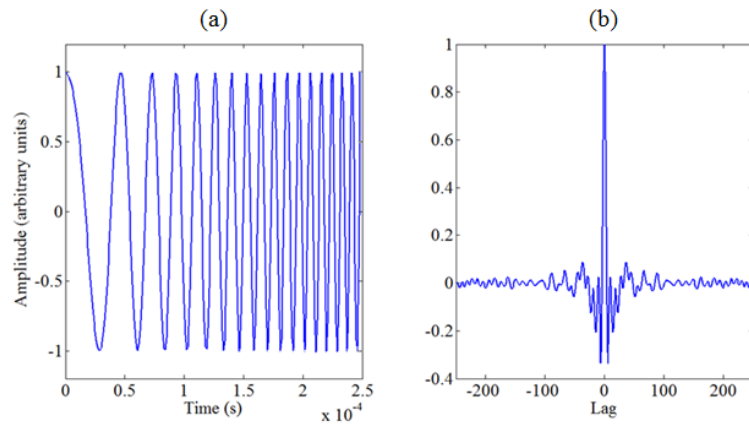
Figure 2.6: Chirp wave form: (a) wave form and (b) auto-correlation response

Sampling rate conversion has been widely used in [**38**]:

- Communication systems

- Speech processing systems

- Antenna systems

- Radar systems

The interpolation process is the conversion of the original sampling rate to the higher sampling rate *i.e.* $F' > F$ or $T' < T$ hence, the compact set of samples would generate samples of the original physical process. Besides, the reverse process is so called decimation. This concept was formulated by Crochiere and Rabiner [1981]. Figure 2.7 represents a sampling rate conversion system with the input signal $x(n)$, sampled at the rate $F = 1/T$, and aiming to calculate the output signal $y(m)$ with a new sampling rate $F' = 1/T'$ [**38**].

Figure 2.7 also represents that the entire process is a linear time-varying system with digital-to-digital sampling rate conversion. Since the system is linear, each output sample $y(m)$ can be expressed as a linear combination of input samples as [**38**]:

$$y(m) = \sum_{n=-\infty}^{\infty} g_m(n)x(\lfloor mR \rfloor - n) \tag{2.19}$$

$$R = M/L, \quad M, L \in \mathbb{N}$$

where, $g_m(n)$ is the response of the system at the output sample time m to an input at the input sample time $\lfloor mR \rfloor - n$ and R is the rational fractional ratio. It is also noticeable that the (2.19) would be considered as time-invariant digital convolution equation if $R = 1$. Furthermore, as shown in (2.19), the system response $g_m(n)$ is periodic in m with period L, and it can be defined as [**38**]:

$$g_m(n) = g_{m+rL}(n), \quad r \in \mathbb{Z} \tag{2.20}$$

There are commonly three basic categories of rate conversion, (a) integer ratio conversion (b) fractional ratio conversion and (c) variable ratio conversion. Here, the main focus is on fractional ratio conversion since it has been employed as a part of the signal processing technique presented in Chapter 4. When the two sampling rates have a simple fractional relationship; *i.e.*, M/L, there is a periodicity in the relationship between samples in the two streams.
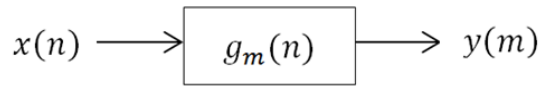
Figure 2.7: Basic process of sampling rate conversion

Therefore, the fractional-ratio converter could be made by arranging two integer-ratio converters M, L in series and the input sampling rate is multiplied by L in an interpolator, and the result is divided by M in a decimator, accordingly interpolation phase changes for each output. In this case, the general case of conversion by the ratios given in (2.21) and (2.22) are considered.

$$\frac{T'}{T} = \frac{M}{L} = R \qquad (2.21)$$

or,

$$F' = \frac{L}{M}F = \frac{F}{R} \qquad (2.22)$$

Figure 2.8 illustrates an example of sampling rate conversion in a sinusoidal pulse.

2.5.5 Fourier transform

The Fourier transform named after Joseph Fourier is a mathematical transformation employed to transform signals between the time/space and frequency domain which have many applications in physics and engineering. It is reversible and capable of transforming from one domain to another. Fourier Transform methods have been widely used in signal processing for UGWs. Here in this chapter the
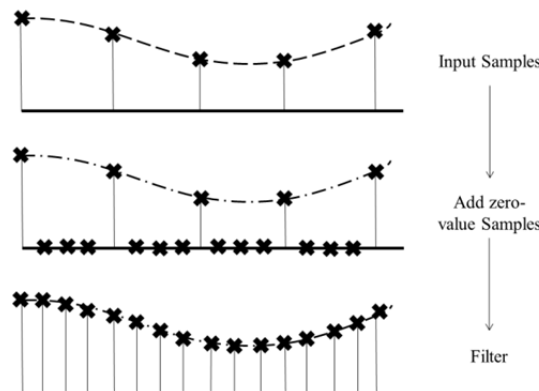
Figure 2.8: A simple example of sampling rate conversion [37]

fundamental concepts of the Fourier transform methods are discussed. Though the detailed descriptions of the research works using Fourier transform methods are reviewed in Chapter 3 based on the recent published literature.

Discrete Fourier Transform (DFT)

DFT borrows elements from both the Fourier series and the Fourier transform. It has all three desired properties. It applies to discrete signals which may be

(a) Periodic

(b) Of finite duration

(c) Have a discrete frequency spectrum

The DFT is essentially a discrete version of the Discrete Time Fourier Transform (DTFT) formulated in (2.23).

$$X(\omega) = \sum_{t=-\infty}^{\infty} x(t)e^{-j\omega t} \tag{2.23}$$

It is a function of the frequency index n, where the nth harmonic of the DTFT is defined as,

$$\omega_{\tilde{n}} = 2\pi\tilde{n}/\tilde{T}, \qquad 0 \le \tilde{n} \le \tilde{T} - 1 \tag{2.24}$$

Here $\tilde{T}$ is the period of the signal.

Then, the value of the harmonic can be substituted into the (2.23) as,

$$X(\tilde{n}) = \sum_{t=0}^{\tilde{T}-1} x(t)e^{-j(2\pi t\tilde{n}/\tilde{T})} \tag{2.25}$$

where t is the time index and $\tilde{n}/\tilde{T}$ is the $\tilde{n}^{th}$ harmonic.

It is notable that the only difference between the DTFT expression (2.23) and the DFT (2.25) is the range of summation.

The DFT uses only a finite number of harmonics, instead of the infinite for the DTFT, namely $\tilde{T}$, so its spectrum resolution as measured by the fundamental frequency $\omega_0 = 2\pi/\tilde{T}$ is discrete and finite. Conceptually speaking, it may be easier to think of the DFT as sampled DTFT at specific frequency points [39].

The algorithm for Fourier transform existed for more than 200 years before it came into widespread use mostly because we could not cope with such large number of

computations. The algorithm waited for the development of the microprocessor [39]. In 1948, Cooley and Tukey [40] presented a computational development called the Fast Fourier Transform (FFT) algorithm which allowed the computation of a $\tilde{T}$ point DFT as a function only $NlogN$ instead of the N^2.

2.5.6 Short-Time Fourier Transform (STFT)

The Fourier spectrum may not deliver sufficient information when analysing non-stationary signals which require an understanding of how the frequency content of the signal changes over time. The STFT method was created to quantitatively address the issue. From Cohen [41], the STFT splits a time domain pulse into a series of small intersecting portions. These portions are windowed and then discretely Fourier transformed. The STFT of an input $x(n)$ is defined as,

$$Y(\omega, t) = 1/2\pi \int_{-\infty}^{+\infty} e^{-\omega\tau} x(\tilde{\tau}) w(\tilde{\tau} - t) d\tilde{\tau} \tag{2.26}$$

where $w(t)$ is a window function. The energy density spectrum of an STFT is defined as (2) and called the spectrogram.

$$E_1(\omega, t) = |Y(\omega, t)|^2 \tag{2.27}$$

Time-frequency trade-off is the resolution limitation between time and frequency according to the uncertainty principle[11], *e.g.*, the Gabor-Heisenberg inequality [41]. Improved time-frequency methods have been proposed to balance the uncertainty in Time-Frequency Representation (TFR) which are mainly divided into two categories: Cohen's-class bilinear time-frequency distributions [41] and affine-class time-frequency distributions [42]. In UGW applications, all of these methods are able to reflect the time-frequency properties of the energetic guided components. Recently, many studies on UGWs were done by comparing TFRs with the theoretical dispersion curves. More information is given in Chapter 3 with specific focus on the recent published literature.

---

[11]From Cohen, 'The phrase 'uncertainty' was coined in quantum mechanics, where its connotation is appropriate since quantum machanics is an inherently probabilistic theory. In quantum mechanics the standard deviations involve the measurement of physical observables. However, in non-probabilistic contexts the uncertainly principle should be thought of as expressing the fact that a function and its Fourier transform cannot be made arbitrarily narrow. Also, according to Skolnik, the use of the phrase 'uncertainty' is a misnomer, for there is nothing uncertain about the 'uncertainty relation'

2.6   Chapter summary

This chapter covered the theoretical background necessary for the following chapters. It described the principles of elastic waves and UGWs which are repeatedly referred to throughout the thesis. The fundamental background of signal processing in UGWs was also covered within this chapter which is required for Chapters 4 and 5 introducing novel signal processing techniques for wave mode identification in multimodal UGW signals. In addition, the basic definition for wave propagation, dispersion and mode conversion phenomenon were described which are necessary for Chapter 6 reporting and studying the coupling dependant guided wave reflections and mode conversions from transducer coupling.

Chapter 3

Literature Survey for Ultrasonic Guided Wave Technology

3.1 Chapter overview

This chapter reviews the most significant works in relation to current research into UGW inspections and signal processing techniques for UGWs, specifically concentrating on the fields to which contributions have been made by this thesis. A general survey including the nature of sound and the founders of UGWs in different applications are provided in Section 3.2. The specific contributions are reviewed and summarized in Section 3.4 based on the literature survey provided in Section 3.3.

3.2 UGWs for NDT

The nature of sound has been explored by Rayleigh [43], Helmholtz [44], and Lamb [45] for 100 years. UGWs however have attracted the attention of many researchers in the field in recent 50 years. After the classic analysis and description of acoustic waves in plates by Horace Lamb, Worlton [23] recognised the potential of Lamb waves for the use of NDT, but he only considered the application to plates. Viktorov recognised the potential application of Rayleigh and Lamb modes for flaw detection in NDT of plates, tubes and thin-walled articles of complex shape [46]. In 1961, Meitzler [21] studied the propagation of elastic waves in wires. He showed that at certain critical frequencies where two modes of propagation have the same phase velocity pulses propagating in certain modes experience pronounced distortion with a remarkable reduction in the peak amplitude of the pulse and increase in

the duration of the pulse many times its original length. He also proposed particular notations for the different propagating wave modes which have been repeatedly used in the symbolization of different UGW modes these days. The notations were adopted as $L(0,q)$ – Longitudinal modes; $F(\beta,q)$ – Flexural modes; $T(0,q)$ – Torsional modes, hence $L(0,1), T(0,1)$ and $F(1,1)$ are respectively referred as fundamental wave modes of interest[12]. By referring to Meitzler's work, Silk & Bainton [47] empirically studied the generation of UGWs in thin-walled metal tubing using piezoelectric probes. They presented the propagating longitudinal wave modes (*i.e.* $L(0,1)$ and $L(0,2)$) and found that the $L(0,1)$ wave mode was generated with greater efficiency than the $L(0,2)$ wave mode. They also assessed the interaction of UGWs with artificial defects in pipes using $L(0,1)$ and $L(0,2)$ wave modes. Böttger *et al.* [48] developed a prototype system with computer support for ultrasonic inspection of ferritic tubes using UGWs. The waves were pulsed and received with the aid of Electro-Magnetic Acoustic Transducers (EMATs). They also recognised the linear relationship between the amplitude of reflected signals of the $T(0,1)$ wave mode and the cross sectional area of the defect.

In the 1990s UGWs attracted the attention of NDT researchers due to the emergence of reasonably priced, powerful computers. Mudge *et al.* [49], Cawley & Alleyne [50] and several other researchers [51], [52], [53], [54], [55], [56] studied the work of past researchers and applied it to the NDT of other types of structures *e.g.* pipes, rods, bars, plates. Cawley & Alleyne recommended making an appropriate choice of Lamb mode(s) and frequency-thickness range hence to use wave modes in a non-dispersive region. They suggested the use of the $L(0,2)$ wave mode for inspections at the frequency range of interest [9][13] on 3 inch diameter pipes due to its non-dispersive nature. Thus, a ring of shear mode piezoelectric transducers coupled around the circumference with axial alignment could particularly generate the $L(0,2)$ wave mode [13]. In addition, two rings of transducers were used to supress the generation of $L(0,1)$ wave mode along the surface of the waveguide. This was achieved by separating the transducers by the wavelength of $L(0,1)$ exciting with reverse polarities. They also added another ring in order to amplify the $L(0,2)$ wave mode by creating constructive interference of the desired mode. If the signal transmitted by the first two rings is phase delayed from the signal to the third ring, by the ratio of their separation and the $L(0,2)$ phase velocity [13], the distinct wave can be propagated only in one direction/forward.

---

[12]where β & $q = \{1, 2, 3, \ldots\}$

[13]The frequency region of interest for UGW inspection is commonly from 20 kHz to 100 kHz.

Two years Later, Alleyne & Lowe [57] evaluated the possibility of using the $T(0,1)$ wave mode in a similar fashion. According to their study, the fundamental torsional wave mode obtained:

1. Several advantages over the second order longitudinal mode as follows:

    (a) $T(0,1)$ is a UGW in pipes which does not have a frequency dependent velocity (*e.g.* approximately 3260 m/s for carbon steel). This makes it non-dispersive across the whole frequency region.

    (b) $T(0,1)$ is an axisymmetric wave mode that has circumferentially aligned particle displacements (with negligible radial and axial displacements at low frequency ranges *i.e.* 15-kHz to 40-kHz).

    (c) Only one ring of shear mode transducers placed around the pipe circumference (such that they displace the surface circumferentially) is capable of generating $T(0,1)$ wave mode.

2. A disadvantage that is the $T(0,1)$ wave mode propagates with a velocity much less than the $L(0,2)$ wave mode at the frequency range of interest. This means that test resolution/range can decrease due to the shorter wavelengths.

3.3 Signal processing for UGWs

Pavlakovic *et al.* [58] described a method to measure the dispersion of UGWs as a form of dispersion curve. This method was implemented in the DISPERSE software. The software calculates the dispersion curve for each wave mode across the chosen frequency region and provides an animation of the particle displacement pattern for each wave mode for a given material and geometry. This software has been used throughout the thesis to generate the dispersion curves of the structures under investigation *e.g.* Figure 2.4. Wilcox *et al.* presented a technique for modelling the propagation of dispersive wave packets. They described the technique for predicting the rate of spreading of a dispersive signal. The technique also assumes that the spectrum of the wave packet is the same as that of the electrical signal applied to the transducers. They also introduced a Minimum Resolvable Distance (MRD) which could predict the minimization of the wave packet's duration after a given propagation distance. The method was employed in Chapter 4 and 5 in order to perform the signal synthesis. It is based on injecting a frequency dependent phase twist to the wave packet which depends on the phase velocity of the

wave mode as a function of frequency given by dispersion curve. In this case it is assumed that the transducer is ideal and only excites the UGW mode of interest at a presumed location $u(x,t) = f(t)$. Therefore, it is necessary to find the input signal $f(t)$ at a given propagation distance d and calculate the received time-trace $g(t)$ assuming that there is no mode conversion after reflection from structure's feature.

Thus, the received time trace can be predicted as,

$$g(t) = \sum_j \int_{-\infty}^{+\infty} A_j(\omega)F(\omega)e^{i(k(\omega)d_j - \omega t)}d\omega \qquad (3.1)$$

where, ω is the angular velocity defined as,

$$\omega = k(\omega) \times v_{ph} \qquad (3.2)$$

$A_j(\omega)$ is the reflection coefficient of each reflector and d is the propagation distance. Sicard *et al.* and Wilcox presented a method to compensate the effect of dispersion from UGW signal [59], [60]. The method only works for a specified wave mode, in a particular structure, with known dispersion characteristics within the signal bandwidth. This method was employed to develop the novel signal processing presented in Chapter 5. Dispersion compensation techniques are used to reverse the effect of dispersion in order to achieve better spatial resolution. The algorithm makes use of *a priori* knowledge of the dispersion curve of a UGW mode and processes the signals in order to map them from the time domain to the spatial domain and reverse the dispersion process. If $g(t)$ propagates backward to its source location $(t = 0)$ in reversed propagation direction using negative distance $(x = -x)$, the dispersion compensated waveform $h(x)$ can be expressed as,

$$h(x) = \int_{-\infty}^{+\infty} h(k)e^{-ikx}dk \qquad (3.3)$$

where,

$$h(k) = G(\omega)v_{gr}(\omega) \qquad (3.4)$$

and,

$$\omega = \omega(k) \qquad (3.5)$$

where x and k represent the distance and wave-number respectively and $G(\omega)$ is

the Fourier transform of the $g(t)$. The Inverse Fourier transform can be used to calculate $h(k)$ in (3.3). Because $G(\omega)$ is a complex function containing phase and amplitude information, the interpolation requires some care to correctly preserve the phase information.

Lui and Yuan [61] presented a linear mapping technique to eliminate dispersion of Lamb waves in the frequency domain. The dispersion properties are expressed as a local quadratic polynomial within the bandwidth of the center frequency. The mapping is then implemented in the Fourier domain by converting the dispersion relation into non-dispersive linear dispersion. The time-domain un-dispersed signals are subsequently recovered using inverse Fourier transform. Xu *et al.* [62] reviewed and compared the dispersion compensation and removal techniques. They applied the both techniques to S0 and A0 wave modes propagating in an aluminium plate. They numerically and empirically demonstrated that both techniques are capable of recovering the original shape of a dispersed S0 wave packet. However, the dispersion removal algorithm takes less computation efforts than the dispersion compensation algorithm. Later, Xu *et al.* [63] investigated cross-correlation, envelop moment, matching pursuit decomposition and dispersion compensation using a dispersive Lamb wave mode on an aluminium plate. According to their study among all the methods, dispersion compensation delivers the best ToA estimation despite the fact that it was applied to a single wave mode.

3.3.1 Wave mode identification in UGW testing

Fourier Transform Methods

In 1978, Sachse and Pao [64] developed a one dimensional phase spectrum method to determine the phase function of a Fourier analysed pulse, the dispersion relation and the propagation speed of waves in solid media. Inspired by Sachse and Pao, Alleyne & Cawley [65], [66] demonstrated how two-dimensional data is required to achieve wave mode isolation, using time domain data collected from several equally spaced points on the surface of a pipe along the axis. This is a useful method from a research point of view, but inconvenient for field inspections in a pitch-catch experiment. This requires either an array of transducers or laser vibrometry equipment which can be expensive and/or time consuming. Prosser & Seale *et al.* [67] combined a time-frequency analysis (the pseudo-Wigner-Ville

distribution) with a broadband excitation source[14] and managed to characterize the Lamb mode dispersion and recover a part of the dispersion curve of the wave modes. They demonstrated their technique in the analysis of a simulated waveform in an aluminium plate and experimental waveforms from a unidirectional graphite/epoxy composite plate. Portions of the dispersion curves of the A_0, A_1 and S_0 and S_2 Lamb modes were achieved from the aforementioned waveforms. However, their technique suffers from the uncertainty principle, which makes a challenge in the allocation of energy to individual propagation modes. Minozio *et al.* [68], proposed a technique using two dimensional spatial-temporal Fourier transform and Singular Value Decomposition (SVD). They managed to recover a UGW phase velocity dispersion curve from a 2 mm thick copper plate. However, the technique requires measurements of several propagation distances using multiple transmitter/receiver which makes it expensive, time consuming and impractical for field inspections. Xu *et al.* [69] used a crazy-climber algorithm to separate time-frequency ridges of individual modes from TFR ridges. The crazy-climber algorithm was used to separate time-frequency ridges of distinct wave modes from Time-Frequency Representations (TFR) of a multimodal response. Then the individual wave modes were reassembled from the TFR ridges. They found that the separated TFR ridges were in agreement with the theoretical dispersion, and the reassembled signals were representative of the individual guided modes. However, there were some limitations due to the difficulty in identification of some wave modes as a result of the superposition between $L(0,4)$ and $L(0,5)$ in their study. Moreover, the application of this technique is restricted by the requirement for manual intervention. Mallet [70] considered cross-correlation, wavelet de-noising and Split Spectrum Processing (SSP) to be applied and examined on synthesized and experimental UGW response. It was shown that cross-correlation and wavelet de-noising are not appropriate techniques for the reduction of non-random noise since it removes the smaller amplitudes regardless of whether or not they are signal or noise. However, it was demonstrated that the SSP has great potential for improving the SNR which is highly dependent on the implementation and the parameters in the spectral splitting for SSP.

Song *et al.* [71] used a blind identification algorithm via the Joint Approximate Diagonalization of Eigen-matrices (JADE) in order to separate superposed UGWs in long bones. They suggested that the JADE algorithm may be used to separate

---

[14]The broadband acoustic waves are produced by a pencil lead fracture Hsu-Neilsen source and sensed with ultrasonic transducers. This source mechanism generates broadband, transient acoustic waves and is often used to simulate acoustic emission signals.

the superposed signals and could potentially be used to evaluate long bones. They reached an agreement in their simulation case between the estimated velocity and theoretical prediction. However, such an approach requires multi-measured acquisitions concurrently which make it impractical for field applications of UGWs. Xu *et al.* solved the single mode limitation of the traditional dispersion compensation methods and further proposed a multimode compensation technique [72] with the advantages of selective mode separation and parameter estimation. However, since all the dispersion compensation methods make use of *a priori* knowledge of the dispersion curve, further improvements are yet required.

Zeng & Lin [73] used the dispersion pre-compensation method on the narrow-band excitation signals, and managed to compress the time duration of received wave packet in an aluminium plate. Also they extracted the information of multiple distinct frequency ranges and responses to a few narrow band excitations using broadband chirp excitation thus optimizing the excitation waveform. However, this technique uses *a priori* knowledge of the dispersion curve and the propagation distance.

Broadband excitation and pulse compression of UGWs

Broadband excitation and pulse compression techniques have been recently found useful in many applications [30], [31], [32] such as radar, sonar, telecommunications, medical ultrasound [74] and material characterization [75]. Due to its powerful SNR improvement and localization features, pulse compression technique has been used in air-coupled ultrasonic testing where acoustic impedance mismatch-induced SNR degradation severely limits the inspection quality. Thornicroft [76] proposed a method to the existing pipeline inspection [9] procedure by exploiting the information enclosed within a broadband response using broadband chirps. His work led to a new collection procedure for Teletest Focus® inspection systems. He showed that narrowband signals could be extracted from a broadband UGW response using an adaptive FFT filter which was based upon the desired spectrum of the narrowband excitation. Gan *et al.* used capacitive transducers to generate chirp signals in air-coupled imaging of solid samples (aluminium disk, carbon-fiber composites) [77]. They showed that using broadband chirp signals significantly increase the SNR which paves the way for a much wider range of measurement. Later, Gan *et al.* [78] showed that the combination of air-coupled ultrasonic techniques and processed chirp waveforms possess a good sensitivity for ultrasonic through-transmission of wood samples. They used matched filter and gap filter

to recover the received signals which led to SNR improvement. Rodriguez *et al.* used air-coupled piezoelectric arrays and Golay codes to inspect copper plates [79]. They showed that the advantages of using Golay coded signals are a greater SNR when using pulse compression, a more precise ToA calculation and a greater use of the transducer bandwidth compared with burst excitation. Ricci *et al.* used chirp signals to inspect forged steels with high attenuation [80]. They found that the use of pulse compression achieves a significant enhancement of the SNR and then of the inspection capability. Michaels *et al.* [81] utilized the chirp excitations to address the need to both test at multiple frequencies and achieve a high SNR to minimize acquisition time. A broadband chirp was used to acquire data at a wide range of frequencies, and deconvolution was applied to extract multiple narrow-band responses. Zhang *et al.* [82] used Barker code excitation to enhance the SNR of the UGW response. The simulations and experiments were performed on the fractured cortical bone plate model, and received signals were decoded using the Finite Impulse Response Least Squares Inverse Filter (FIR-LSIF) and then compared with the results given by the sinusoidal pulse. They suggested that the coded excitations can potentially improve the SNR however further studies are required to be undertaken for multimodal cases. Zhou *et al.* used the wavelet transform to filter the noise and utilized Barker codes to perform pulse compression [83] in order to improve the SNR. They also analysed different Barker codes (5-13 bits) to achieve higher main to side-lobe ratio. They concluded that the 13-bit Barker code is more appropriate for the phase-coded pulse compression processes.

Although pulse compression improves the SNR which leads to a greater confidence in wave mode identifications, further improvements are still required in the application of the technique to be able to identify different wave modes in the complex superposed signals. These complex signals possessing various superposed UGWs are mainly caused by multimodal propagation of UGWs and/or reflections/mode conversion from different structural features. Toiyama & Hayashi [84] proposed the dispersion compensation method [60] using pulse compression to remove the effect of velocity dispersion and improve the SNR. The UGW was excited with a broadband temporal signal (chirp) and then the cross-correlation process was applied corresponding to the pulse compression and the dispersion compensation processes were executed simultaneously. The results showed that the improved pulse compression technique achieves enhanced SNR. However their technique was applied to uni-modal UGW response and the performance of the technique is not yet evaluated in multimodal cases.

3.4 Chapter summary

According to the literature presented in Section 3.3, an effective automatic technique to generate useful quantitative information such as propagation distance, ToA and dispersion curves for UGW inspection to be used out in the field remains a signal processing challenge where multimodal responses are concerned. It was suggested that the two dimensional Fourier transform methods [64], [65], [66], [68] are useful for research purposes but unsuitable for field inspection of UGWs since they require several spatial measurements using transducer arrays or laser vibrometry scans. The application of TFR techniques [67], [69], [72] is restricted by the requirement for manual intervention rather than an automated computerized process. In addition, there are limitations due to the difficulty in identification of closely spaced modes. These techniques also suffer from the uncertainty principle which makes it difficult to determine the modal energy attribution. Dispersion compensation based techniques [59], [60], [72], [73], [84] show promise for SNR improvements and claim greater confidence in wave mode identification of UGWs since the temporal broadening of the pulse caused by dispersion could be compensated. However, all of the dispersion compensation based techniques require *a priori* knowledge of the dispersion curve.

In addition, pulse compression techniques [77], [78], [79] were found to be useful for SNR improvements and wave mode identification of UGWs. However in multimodal cases where several dispersive and non-dispersive signals are superposed wave mode identification remains a challenge, particularly for dispersive wave modes. Further studies [84] employed pulse compression techniques considering velocity dispersion of UGWs. They showed that the SNR could be further enhanced when dispersive signals are compensated for dispersion, however; these studies are limited to uni-modal analysis and the performance of the technique in multimodal cases is yet to be evaluated.

Chapter 4

Frequency-Sweep Examination for Wave Mode Identification in Multimodal UGW Responses

4.1 Chapter overview

In this chapter a novel signal processing technique is presented using a combination of frequency-sweep measurement, sampling rate conversion and Fourier transform. The technique is applied to synthesized and experimental data in order to identify different modes in complex UGW signals. It is demonstrated throughout the chapter that the technique has also the capability to derive the ToA and group velocity dispersion curve of different wave modes. The research conducted in this chapter has been presented in *American Society for Non-Destructive Testing (ASNT) 23rd Research Symposium*, Minneapolis, United States of America on March 2014, and in *The Young Welding International Conference (YPIC)*, Budapest, Hungary on Sept. 2014 [**SF 08**]-[**SF 12**]. Also, this chapter resulted in a journal publication in *IEEE Transactions on Ultrasonics, Ferroelectrics and Frequency Control (IEEE-TUFFC)* [**SF 01**], [**SF 04**].

The background theory of the technique is covered in Section 2.5. Section 4.2 provides the reader with step-by-step procedure for the employment of the signal processing technique followed by sufficient mathematical implementation for each step. A signal synthesis is conducted considering single mode and multimodal UGW response to evaluate the performance of the aforementioned technique in Section 4.3. Section 4.4 covers the experimental validation and further analysis for the application of the technique. The summary of the chapter and concluding

remarks are given in Section 4.5.

4.2 Frequency -Sweep Examination (FSE)

A novel signal processing technique is developed using the combination of adaptive sampling rate conversions in fractional-ratio, Fourier transform and the concept of Frequency Sweep Spectrum (FSS) to identify different wave modes in a complex UGW response including several superposed signals. Specifically, accurate quantitative information such as, total number of existing wave modes in a particular frequency range, number of constituent wave packets in a superposed signal, v_{gr} of a wave mode by extracting the ToA is to be taken out from the technique outcome in order to ease the structural feature detection process. The technique employs multiple cycle Hann windowed sinusoidal pulse train [27], [85] excitations at a range of UGW frequencies which are equally incremented. It proposes to identify signals with similar group velocities but different gradient arising from independent modes. It is shown that the rate converted time shift caused by sampling rate conversion for each signal can make all of the acquisitions appear as if excited at the same frequency as the frequency of interest. Consequently, this promotes sequential rate converted time shifts to the individual acquisitions at each frequency increment. Hence, the technique can exploit the rate of shifts in the rate converted time which facilitates the identification of different wave modes in the superposed signals. It is also best suited for one dimensional structures *e.g.* rods, bars, pipes, rails, *etc.* A block diagram is provided in Figure 4.1 in order to provide a pictorial representation of the descriptions given in Section 4.2.1 to Section 4.2.5.

The methodology is initially applied to synthesized data performed by MATLAB-R2011b and then validated using experimental data collected using a *Teletest Focus*™ Pulser/Receiver.

4.2.1 Data collection

In order to extract useful information from the application of the Frequency-Sweep Examination (FSE) technique, the data collection must follow a particular routine. The UGW excitations should cover a wide range of UGW frequencies starting from f_0 to f_{p-1} with equal incremental factor (q). The acquisitions $x_\alpha(t)$, with the excitation index of $\alpha = \{0, 1, 2, \ldots, p-1\}$ are arranged in a matrix with p different steps/rows at each excitation frequency. Therefore, the frequency-sweep increment $(\tilde{q})$ and the acquisition matrix can be respectively expressed as,
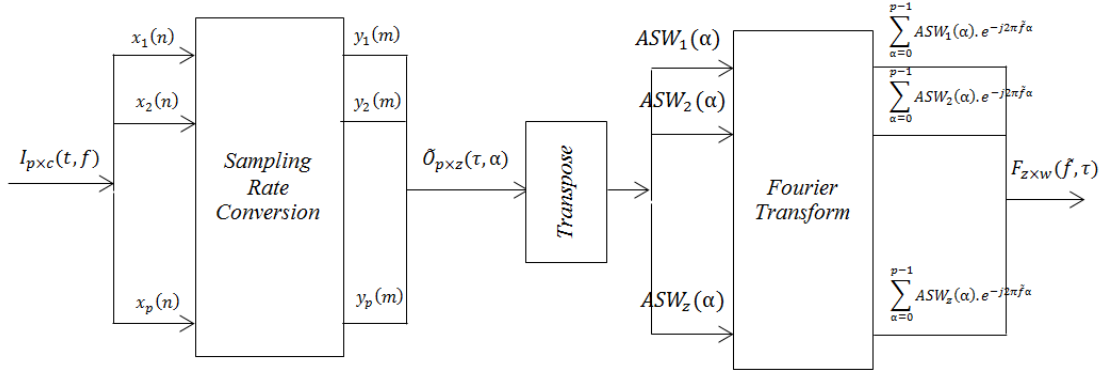
Figure 4.1: FSE block diagram

$$\tilde{q} = \frac{f_{\alpha=p-1} - f_{\alpha=0}}{(p-1)}, \ \forall p \in \mathbf{N} \tag{4.1}$$

$$I_{p \times x}(t, f) = \begin{bmatrix} x_1(t) \\ x_2(t) \\ \vdots \\ x_p(t) \end{bmatrix}_{p \times c} = \begin{bmatrix} I_{11} & \cdots & I_{1c} \\ \vdots & \cdots & \vdots \\ I_{(p-1)1} & \cdots & I_{(p-1)c} \\ I_{p1} & \cdots & I_{pc} \end{bmatrix} \tag{4.2}$$

where, c is the number of columns in the matrix which represents the length of each single acquisition, f_{p-1} is the upper limit of frequency-sweep and f_0 is the lower limit.

A constant appropriate sampling rate (1 MHz) [86] is used for each acquisition in the array, $x_\alpha(t)$ which satisfies the Nyquist criterion for the highest frequency /bandwidth acquisition. The criteria for the choice of p and $\tilde{q}$ is discussed in later sections in the context of *Data resolution*.

4.2.2 Sampling rate conversion

Each acquisition $x(t)$ is transformed to a new signal $y(\tau)$ as defined in (4.2) and (4.7) by fractional ratio sampling rate conversion [87]. For each signal, a Spline [88] is fitted to the samples in order to reconstruct the original signals. Sampling starts at the begging of the signal so that the first sample is common to both $x(t)$ and $y(\tau)$. The fractional ratio for each transformation is chosen and defined in (4.3) and (4.4) according to the frequency of excitation, so that each signal appears to have the same excitation frequency as f_0. Thus, the acquisitions will be ready for the direct comparison along the rate converted frequency-sweep axis.

Series of fractional sampling rate conversions are applied to each acquisition in order to rate convert over the entire range of frequencies, (f_0 to f_{p-1}) and adjust them back to the, f_0 frequency. Therefore, it can facilitate the extraction of quantitative information *i.e.* ToA and group velocity at f_0 after the application of Fourier transform. The fractional-ratio converter can be made by arranging two integer-ratio converters M, L in series. The input sampling rate is multiplied by L in an interpolator, and the result is divided by M in a decimator. Therefore, the general fractional ratio can be expressed as,

$$\frac{T'_s}{T_s} = \frac{M}{L} = R \ or \ F'_s = \frac{L}{M}F_s = Fs/R \qquad (4.3)$$

where, T_s, T'_s and F_s, F'_s are the input and output sampling intervals and sampling frequencies respectively.

In this chapter we consider an adaptive ratio (R_α) for each frequency-sweep excitation as,

$$R_\alpha = M/L = \omega_0/\omega_\alpha \qquad (4.4)$$

where ω_0 and ω_α are the angular velocity at f_0 and successive sweeping frequencies, f_α respectively defined as,

$$\omega_0 = 2\pi f_0, \omega_\alpha = 2\pi f_\alpha \qquad (4.5)$$

Thus, the output of the sampling rate conversion, $y(\tau)$ can be expressed as [89],

$$y_\alpha(\tau) = \sum_{t=-\infty}^{\infty} \tilde{h}(tL + \tau M \oplus L)x(\lfloor \tau R_\alpha \rfloor - t) \qquad (4.6)$$

where, $\tilde{h}(k)$ is a digital filter (low-pass) which operates both decimation and interpolation process (this can be performed in MATLAB using 'interp1' function). In addition, $\oplus$ represents the modulo operation and $\lfloor u \rfloor$ means less than or equal u. Thus, according to the input matrix given in (4.2) and the aforementioned sampling rate conversion, the output of the rate converted set of acquisitions can be expressed as,

$$\tilde{O}_{p\times z}(\tau, \alpha) = \begin{bmatrix} y_1(\tau) \\ y_2(\tau) \\ \vdots \\ y_p(\tau) \end{bmatrix}_{p\times z} = \begin{bmatrix} o_{11} & \cdots & o_{1z} \\ \vdots & \cdots & \vdots \\ o_{(p-1)1} & \cdots & o_{(p-1)z} \\ o_{p1} & \cdots & o_{pz} \end{bmatrix} \qquad (4.7)$$

where τ is the rate converted time and z is the number of columns in the matrix which represents the length of each rate converted acquisition given after the sampling rate conversion. It is also notable that the number of columns changed (from c to z) due to the effect of sampling rate conversion on the length of each acquisition. This change in the length creates the rate converted time (τ), which is constructed based on the sample shifts caused after the sampling rate conversion. For each individual acquisition, zero-paddings may be required to construct the $\tilde{O}_{p \times z}$ matrix, as they are rate converted with different fractional ratios defined in (4.4).

After the sampling rate conversion, all of the acquisitions appear as if excited at the same frequency as f_0. Therefore, the excitation index (α) has been set as the variable of the column vectors. Here, the Amplitude Sweep Wave form (ASW) can be defined as (4.8). It is constructed as the combination of single value amplitude information of the sampling rate converted acquisitions for a point in rate converted time defined in (4.7). Sample ASWs are given in Section 4.3 & 4.4. It is notable that the $x-axis$ represents the samples collected from the individual rate converted frequency-sweep acquisitions. They show how several superposed signals can be represented in different oscillations.

$$ASW_1(\alpha) = \left\{ \begin{array}{c} o_{11} \\ \vdots \\ o_{(p-1)1} \\ o_{p1} \end{array} \right\}, \ldots, ASW_z(\alpha) = \left\{ \begin{array}{c} o_{1z} \\ \vdots \\ o_{(p-1)z} \\ o_{pz} \end{array} \right\} \tag{4.8}$$

4.2.3 Fourier transform of the Signal Array

In order to obtain the spectrum of the incremental variations after the sampling rate conversion, the ASWs defined in (4.8) should be Fourier transformed. This will reveal the spectrum of incremental variations for each fixed point in rate converted time which is called Frequency Sweep Spectrum (FSS). The FSS measures the rate of shifts in rate converted time for various wave modes in *number of cycles per sample.*

According to the time domain system input-output given in (4.2) and (4.7), the transform relationships of the individual integer decimation and interpolation system, the output spectrum $FSS(\tilde{f})$ can be determined in terms of the input $ASW(\alpha)$ as,

$$FSS(\tilde{f}) = \sum_{\alpha=0}^{p-1} ASW(\alpha).e^{-j2\pi\tilde{f}\alpha} \tag{4.9}$$

Thus, the Total Frequency Sweep Spectrum (TFSS) of the signal array can be expressed as,

$$TFSS_{z\times w}(\tilde{f},\tau) = \begin{bmatrix} \sum_{\alpha=0}^{p-1} ASW_1(\alpha).e^{-j2\pi\tilde{f}\alpha} \\ \vdots \\ \sum_{\alpha=0}^{p-1} ASW_{z-1}(\alpha).e^{-j2\pi\tilde{f}\alpha} \\ \sum_{\alpha=0}^{p-1} ASW_z(\alpha).e^{-j2\pi\tilde{f}\alpha} \end{bmatrix} = \begin{bmatrix} f_{11} & \cdots & f_{1w} \\ \vdots & \cdots & \vdots \\ f_{(z-1)1} & \cdots & f_{(z-1)z} \\ f_{z1} & \cdots & f_{zw} \end{bmatrix} \tag{4.10}$$

The incremental variations correspond to individual row in $TFSS_{z\times w}$ matrix in which include individual $FSS(\tilde{f})$ at each instant in rate converted time. This facilitates the identification of existing wave modes at f_0 in Fourier domain and extraction of the ToA using a threshold based on the specific value sensitive to the level of coherent noise [90] according to the measured Signal-to-Noise Ratio (SNR) at f_0. Figure 4.2 is the schematic illustration of the ToA extraction using fixed threshold[15].
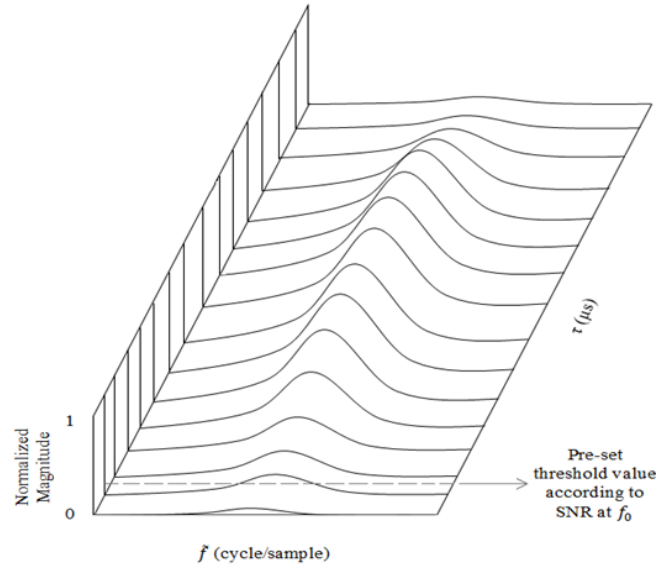
Figure 4.2: ToA extraction via thresholding

---

[15]Assuming that the SNR of the response of interest is known in dB, the threshold can be defined as: $1/10^{SNR/20}$

4.2.4 Data resolution

As it was discussed earlier in Section 4.2.1, a constant appropriate sampling rate was used for each acquisition in the array which could satisfy the Nyquist criterion for the highest frequency /bandwidth acquisition. However, the accuracy of the ASWs is depending on choosing an appropriate number of frequency-sweep acquisitions, p. Figure 4.3 shows the echoes from a non-dispersive wave modes (*e.g.* $L(0,1)$ wave mode in the rod under investigation) which has a linearly increasing shift in rate converted time as the frequency of excitation increases from f_0 to f_{p-1}. Additional results for effect of sampling rate conversion in signal synthesis and experiment are illustrated in Appendix-A. Figure 4.3 also shows a pictorial representation of the variables used in equations below.

The maximum rate converted time shift caused by sampling rate conversion for a non-dispersive signal can be expressed as,

$$t'_{FSE} = (t_{FSE}) \left(\frac{f_{p-1}}{f_0} \right) \tag{4.11}$$

where, t_{FSE} is the lowest experienced rate converted time shift caused by the sampling rate conversion.

The shift between f_0 and adjacent vertical sample can be expressed as,

$$\Delta t_{FSE} = (t'_{FSE} - t_{FSE})/p = \left(\frac{f_{p-1}}{f_0} - 1 \right) \left(\frac{t_{FSE}}{p} \right) \tag{4.12}$$

It is known that [91] the frequency band B of a n cycle Hann windowed sine wave at f_0 which corresponds to the excitation signal is expressed as,

$$B = [f_0 - 2f_0/n : f_0 + 2f_0/n] \tag{4.13}$$

Thus, according to (4.11), (4.12) and the Nyquist criterion, the minimum number of steps (p) should comply with the below inequality.

$$\frac{p}{((f_{p-1}/f_0) - 1)\,(t_{FSE})} > 2(f_0 + 2f_0/n) \tag{4.14}$$

As a result, the necessary range for p is,

$$p > 2(f_0 + 2f_0/n)\,((f_{p-1}/f_0) - 1)\,(t_{FSE}) \tag{4.15}$$

It is sufficient for the necessary range for p to be rounded to the *next power of two*, so as to perform a computationally efficient Fourier analysis.
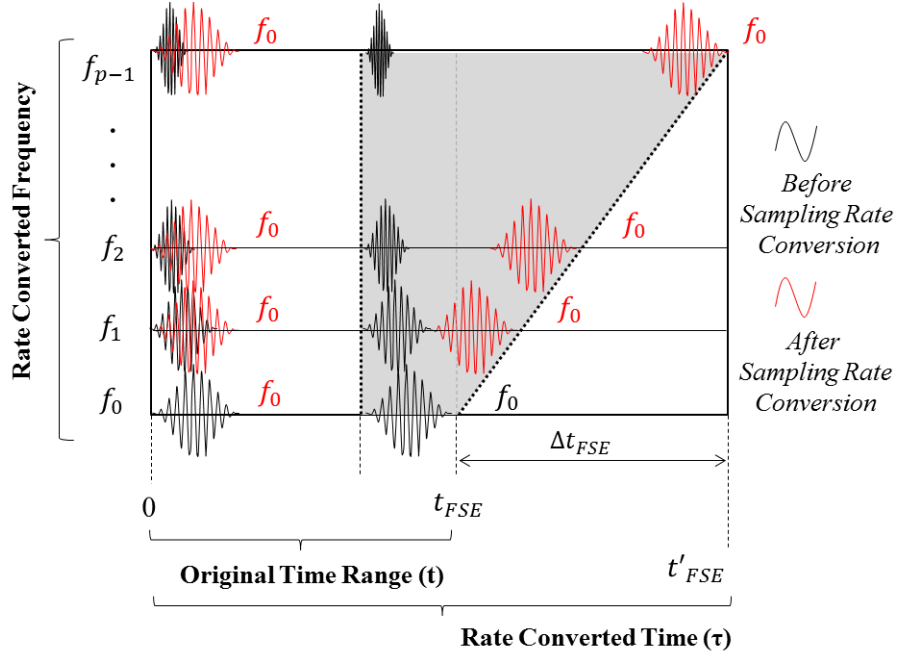
Figure 4.3: Theoretical signals before ($I_{p \times c}$) and after ($\tilde{O}_{p \times z}$) sampling rate conversion

In addition, according to the dispersion curve, the velocity and the ToA of a wave mode may tend to vary and/or remain constant in a certain frequency region depending on its dispersive and/or non-dispersive propagation. Subsequently these variations change the gradient of the rate converted time shift after sampling rate conversion. Therefore, an alternative way to increase the data resolution in the system output, or change the gradient of the rate converted time shift, is to shorten the original time range in order to focus the presence of different wave modes.

4.2.5 Group velocity

According to information given in Section 4.2.3 and assuming that the length of propagation is known (l), the group velocity value at f_0 can be extracted by,

$$v_{gr} = \frac{l}{t_{ToA}} \tag{4.16}$$

where t_{ToA} is the extracted ToA of the wave mode of interest.

The group velocity dispersion curve can also be computed by frequently applying the FSE procedure to the input matrix given in (4.2) with a given gradual change in the value of f_0 frequency, so that the group velocity at that frequency could be extracted sequentially.

For each of the frequency-sweep experiments, the time duration of the n cycle excitation pulse is reduced. As a consequence, the time duration of the reflected signals (especially the non-dispersive signals) is also reduced.

For non-dispersive signals in the frequency-sweep acquisitions, the increasing shift associated with the sampling rate conversion is linearly related to the increasing excitation frequency. Therefore, they can possess a constant frequency in the FSS domain. Figure 4.3 shows this effect for the non-dispersive signals. For dispersive signals, the variations of group and phase velocity with respect to excitation frequency will cause a shift in the time domain even before sampling rate conversion. However, these shifts cannot be traced with ASWs/FSSs due to the possession of different excitation frequencies for each acquisition. After, sampling rate conversion, the acquisitions appear as if excited at the same frequency as f_0. Therefore a more exaggerated non-linear shift can be experienced by dispersive signals which can potentially exhibit higher frequency in $FSS(\tilde{f})$ compared to the non-dispersive signals. These different frequencies in $FSS(\tilde{f})$ facilitate the identification of different dispersive and non-dispersive signals. As a result, the superposed signals should possess different oscillations in the $ASW(\alpha)$ and appear as clear peaks in the $FSS(\tilde{f})$ which facilitate the extraction of ToA and group velocity of the constituent wave modes.

To summarize, the steps in applying the FSE are as follows,

- Collect the frequency-sweep acquisitions, $x_a(t)$ based on (4.1), (4.2), and (4.15), from f_0 to f_{p-1}.

- Apply the sampling rate conversion with the ratios given in (4.4). Therefore, all of the acquisitions should appear as if excited at the same frequency as f_0.

- Construct the $ASW(\alpha)$ based on (4.7) and (4.8).

- Perform the Fourier transform on the $ASW(\alpha)$ at the entire rate converted time range in order to obtain the $FSS(\tilde{f})$ based on (4.9).

- Collect the whole obtained $FSS(\tilde{f})$ in order to produce $TFSS(\tilde{f}, \tau)$ based on (4.10).

- While performing the Fourier transform and constructing the $TFSS(\tilde{f}, \tau)$, define a threshold value sensitive to the level of coherent noise (according to the measured SNR at f_0) in order to automatically identify the existence of the wave modes in a superposed wave packet.

- Perform peak searches in the responses given by $FSS(\tilde{f})$ to extract the number of existing wave modes in a superposed wave packet with their ToA information.

- Compute the group velocity at f_0 based on (4.16).

- Repeat the whole process from the start with a given gradual change in f_0 to compute the desired portion of group velocity dispersion curve.

4.3   Signal synthesis

Signals were synthesized in order to examine the FSE proposed in Section 4.2. The technique is applied to superposed complex wave packets representing the interaction between $L(0, 1)$ and $F(1, 1)$ [21] propagating wave modes. A dispersion synthesis was carried out as a part of the signal synthesis.

4.3.1   Wave mode analysis

A superposed wave packet comprising $L(0, 1)$ and $F(1, 1)$ wave modes were synthesized based on the group velocity dispersion curves (Figure 2.4, Figure 4.6 and/or Figure 4.12) to identify the wave modes with the aid of FSE procedure. Figure 4.4–(a–c)–(left) illustrates sample isolated and superposed wave modes as a result of 20-kHz, 10 cycle Hann windowed excitation. With reference to Section 4.2.1 and 4.2.4, a set of 512 superposed signals were generated from f_0: 20-kHz to f_{p-1}: 100-kHz and are rate converted back to f_0-20-kHz. It should be noted that all the normalized results provided throughout the chapter are performed against the maximum value. The synthesis of the wave modes of interest were performed according to the method described by Wilcox *et al.* [92] using the parameters given in the dispersion curve. In this case it is assumed that the transducer is ideal and only excites the UGW modes of interest at the given location.

Three sample $FSS(\tilde{f})$ of the isolated $L(0, 1), F(1, 1)$ and their superposition at 2300-μs are displayed in Figure 4.4–(a–c)–(middle). Figure 4.4–(a–c)–(right) illustrate contour plots of the $TFSS(\tilde{f}, \tau)$ measured at the entire rate converted time instants where the application sampling rate conversion was in the range of $[1400 : 3000\mu s]$. The distinct curves illustrated in Figure 4.4–(a–c)–(right) are theoretical curves which show the discriminated wave modes of interest and the ability of FSE to identify the superposed wave modes at the frequency of interest where signals are overlapped at f_0-20-kHz *e.g.* Figure 4.4–(d)–(right).

According to the discussion provided in Section 4.2, each row of the rate converted output matrix given in (4.7) contains superposed signals where each is gradually shifted in rate converted time. The spectrum of the the acquisition signals before the sampling rate conversion, gives no indication as to how the wave modes could be possibly identified. Figure 4.4–(d) illustrates that the Fourier transform of the acqusition signal before sampling rate conversion is not capable of presenting useful information to identify the wave modes of ineterest. However, after sampling rate conversion, all of the non-dispersive and dispersive signals of the frequency-sweep acquisition appear as if excited at the same frequency as f_0, while experiencing different shift in rate converted time as the excitation frequency increases, owing to the possession of flat and non-linear group velocity dispersion curve respectively. These different shifts in rate converted time (linear/non-linear) after sampling rate conversion, facilitate a situation where each column of $\tilde{O}_{p \times z(\tau,f)}$ matrix to be selected as $ASW(\alpha)$ possessing different oscillations *e.g.* Figure 4.6 and Figure 4.9. These different oscillations in the selected ASWs defined in (4.8) contain key information about any non-dispersive and dispersive signals which classify each single reflection in different oscillations. It is notable that the *x-axis* of the $ASW(\alpha)$ represents the individual samples at the corresponding rate converted frequency-sweep acquisitions. After the application of Fourier transform on ASWs, FSSs are obtained as shown in Figure 4.4–(middle). The distinct peaks illustrated in Figure 4.4–(middle) correspond to the identified wave modes of interest in the superposed wave packet shown in Figure 4.4–(c)–(left). TFSS shown in Figure 4.4–(right) represents all of the FSSs meshed together at each of their respective rate converted time instants. The Non-dispersive L(0,1) wave mode exhibits a constantly increasing shift in rate converted time, (Section 4.2.4, Figure 4.3) so the position of the peak which is observed in the $FSS(\tilde{f})$ and $TFSS(\tilde{f},\tau)$ (Figure 4.4–(a)–(middle) and (right)) remains constant. However, the dispersive F(1,1) wave mode exhibits a non-linearly increasing shift in rate converted time causing a variation in the position of the peak observed in the $FSS(\tilde{f})$ and $TFSS(\tilde{f},\tau)$ (Figure 4.4–(b)–(middle) and (right)). As was discussed in Section 4.2.3, the ToA of each wave mode (L(0,1): 1720-μs and F(1,1): 2182-μs) at f_0 frequency *i.e.* 20-kHz are extracted by capturing the presence of a new gradually rising magnitude spectrum at each successive time instant (assuming the SNR of 35 dB, consequently threshold of 0.017 for the synthesized multimodal response).

Given the ToA, the group velocity was estimated according to (4.16). Figure 4.6 represents the computed F(1,1) and L(0,1) dispersion curve mapped to the
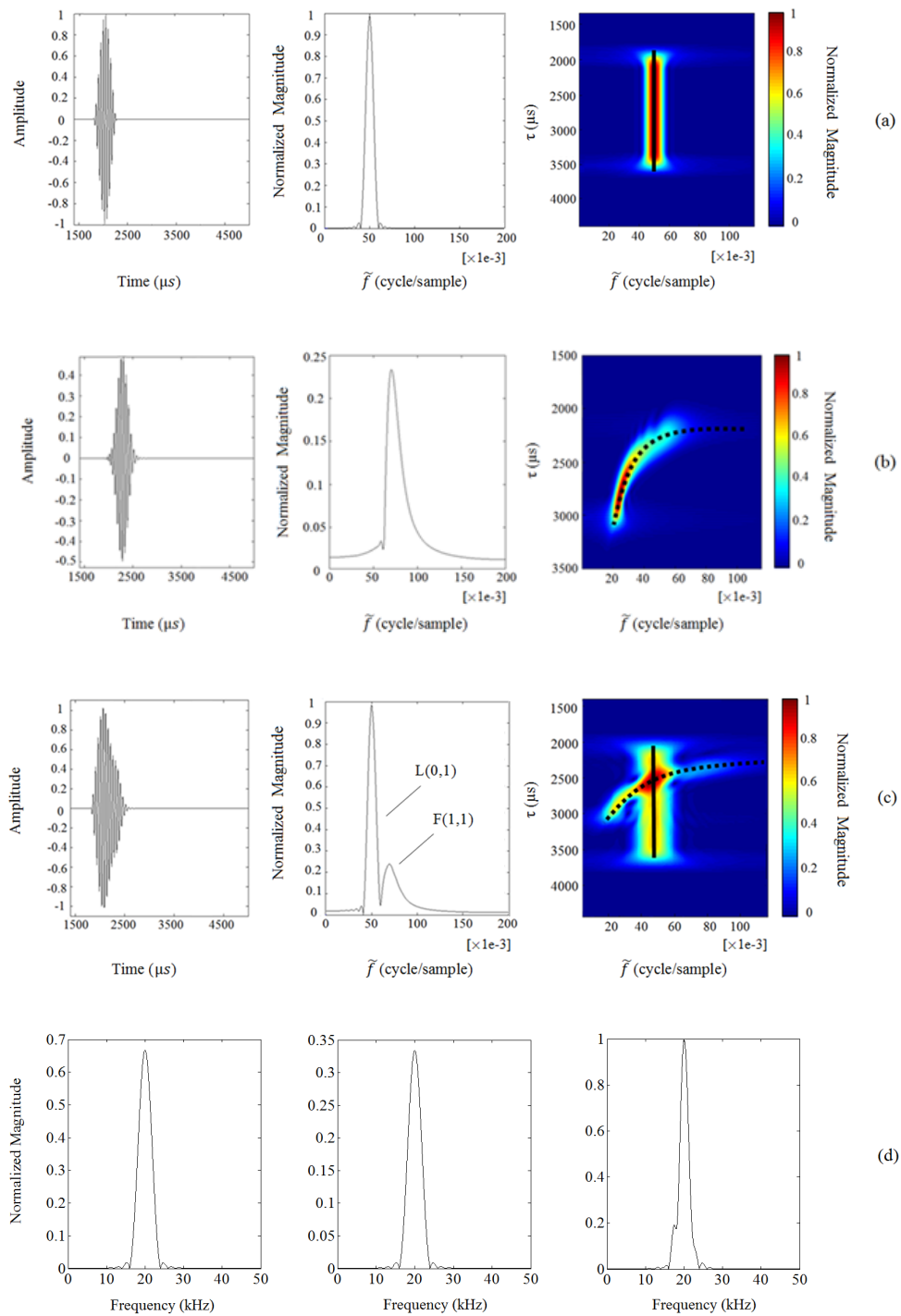
Figure 4.4: From left to right: signal, FSS and TFSS of a (a) Non-dispersive L(0,1) after the propagation distance of 8.6 m, (b) Dispersive F(1,1) after the propagation distance of 4.3 m, (c) Superposition of (a) and (b), (d) Traditional Fourier transform of the non-dispersive L(0,1), dispersive F(1,1) and the superposition of the two.

dispersion curve given by DISPERSE after the application of FSE in sequence to the synthesized signals with a given gradual change in f_0 frequency. Quantified results are also available in Table 4.1.
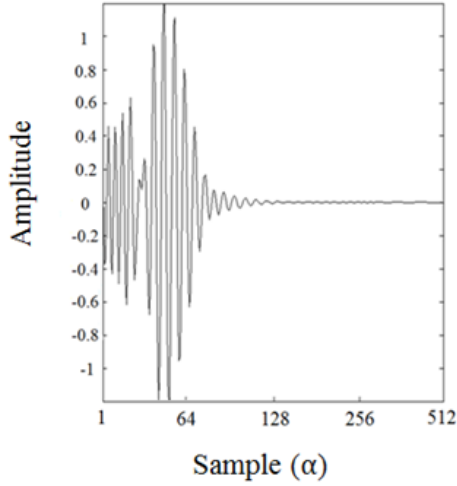
Figure 4.5: Sample ASW at 2300-μs
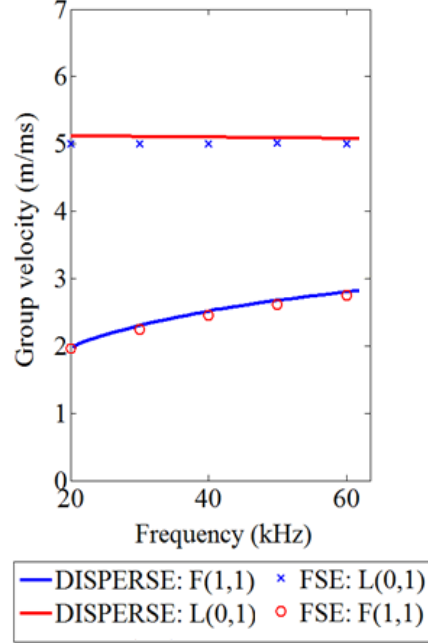
Figure 4.6: Group velocity dispersion curve of the aluminium rod

FSE: Synthesis			
Technique / Wave mode type	ToA	v_{gr}	v_{gr} error[16]
F(1,1)	2182 [μs]	1958 [m/s]	%1.85
L(0,1)	1720 [μs]	5000 [m/s]	%1.96

Table 4.1: Extracted wave mode information (synthesis: 20 kHz)

---

[16]The errors for the extracted the group velocities by the FSE technique are calculated based on the results given by DISPERSE software. Thus the errors only represent the discrepancy between the two provided results.

4.4 Experimental validation

The technuique is applied to pulse-echo UGW signals obtained from an aluminium rod. The data is acquired according to Section 4.2.1 and analysed using the FSE technique. The group velocity dispersion curve of the specimen is also extracted from the given results and validated via DISPERSE.

4.4.1 Experimental setup

The experimental set-up is illustrated in Figure 4.7. A shear piezoelectric transducer [9] is orientated in a manner that allows it to actuate longitudinally in the axial direction of the 2.15 metre length aluminium rod with 8-mm diameter. The transducer was connected to the unit via a tool lead cable and then the unit was connected to the laptop by communication cable. A ten cycle Hann windowed signal was injected from the laptop to the unit and fired from the transducer through the rod.

4.4.2 Data collection and experimental results

In this experiment several UGW signals were collected from the rod with different frequencies and an equal incremental factor. With reference to Section 4.2, 512 frequency-sweep excitations are performed in a wide range of frequencies starting from 20 kHz (f_0) and stopping at 100 kHz (f_{p-1}).

Figure 4.8–(left) displays the acquisition collected at f_0, 20kHz and (right) its corresponding Fourier transform. It can be observed that both time and frequency domain of the UGW response are not capable of delivering useful information to identify the wave modes of interest. Figure 4.8–(left) displays multimodal reflection from the end of the rod with overlapped echoes at different ToAs. It is notable that the first echo of L(0,1) was ignored therefore the acquisition could be analysed with a challenging scenario where several echoes are strongly overlapped.

Figure 4.7: Experimental Setup

The total signal acquisitions are accumulated as an input to the sampling rate conversion. Figure 4.9 and Figure 4.10 represent sample $ASW(\alpha)$ and $FSS(\tilde{f})$ at chosen individual rate converted time instants respectively. The x-axis of Figure 4.9 represents the individual samples collected at the corresponding rate converted frequency-sweep acquisitions. Figure 4.11 displays the $TFSS(\tilde{f}, \tau)$ derived from the superposed signa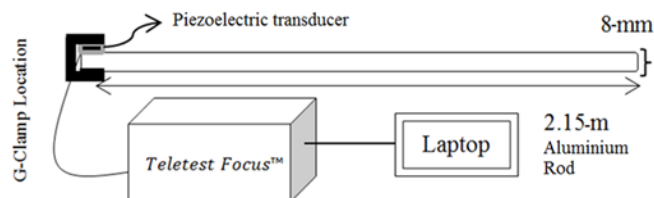ls. As was discussed in Section 4.2.3, the ToA of each wave mode (L(0,1): 1775-μs, F(1,1): 2290-μs and the mode converted signal: 3308-μs) at f_0 frequency *i.e.* 20-kHz are extracted by capturing the presence of a new gradually rising magnitude spectrum at each successive time instant. The SNR of the UGW response was measured to be 27 dB, consequently the threshold of 0.046 was set to capture the presence of a gradually rising magnitude spectrum.

4.4.3 Group velocity and further analysis

According to (4.16) the group velocities of the modes of interest were estimated and compared with the values given by DISPERSE in Figure 4.12. Although T(0,1) could be theoretically generated within the frequency range that has been excited, the orientation of the piezoelectric transducer is aligned to the axial direction of the rod hence this restricts any displacements in the circumferential direction. Therefore the presence of T(0,1) in this set of experiment will be negligible. It is also notable that according to the dispersion curve of the specimen, the cut-off frequency of L(0,2) is approximately at 460 kHz which is beyond the frequency range of excitation.

Here, the mode conversion occurred due to the fact that the transducer is clamped on the end of the rod via a G-clamp. The rod surface is in contact with the piezoelectric ceramic at an arbitrary point on the circumference and the reactive force of the clamp surface is in contact with the rod directly 180° to the prior mentioned arbitrary point. The location where the transducer and clamp are situated produces a feature on the rod hence, after the reflection of the waves from the end of the rod towards the clamp and the transducer, either the longitudinal wave converts to a flexural wave and/or a generated flexural wave has been converted into a longitudinal mode. This produces an additional wave packet, in the acquisition with relatively lower amplitude compared to other echoes. This mode converted wave packet possesses the same velocity as L(0,1) according to having the same *round trip time* [**93**].

Having the capability to identify and discriminate the wave modes with their velocity makes the defect detection process straight forward where the end of the

rod can be treated as a defect of interest which produces mode conversions.

The distinct curves illustrated in Figure 4.11 are traced energy peaks which show the existing superposed wave modes with different gradients at successive echoes. As discussed in Section 4.2.4, during the technique implementation, the original time range has been shorten to highlight the presence of the longitudinal, flexural and converted wave modes at different rate converted times. The wave modes were identified according to their group velocity value given in Figure 4.12. Figure 4.11–(left) represents the superposition of the 2nd echo of L(0,1) and 1st echo of F(1,1) where the application of sampling rate conversion was in the range of $[860\mu s:\ 3000\mu s]$. The L(0,1) wave mode shows a constantly increasing shift in rate converted time, (Section 4.2.4, Figure 4.3) so the position of the L(0,1) peaks which are observed in the $FSS(\tilde{f})$ and $TFSS(\tilde{f},\tau)$ (Figure 4.10 and Figure 4.11) remain constant. However, the dispersive F(1,1) wave mode exhibits a non-linearly increasing shift in rate converted time causing the non-linear variation in the position of the F(1,1) peaks observed in the $FSS(\tilde{f})$ and $TFSS(\tilde{f},\tau)$ (Figure 4.10 and Figure 4.11). Figure 4.11–(middle) represent the superposition of 3rd echo of L(0,1) and 1st echo of the mode converted signal over the given rate converted time where the application of sampling rate conversion was in the range of $[1450\mu s:\ 3800\mu s]$. Figure 4.11–(right) represents the superposition of three wave modes arising due to the reflection and mode conversion at the clamped end of the rod at a given rate converted time range where the application of sampling rate conversion was in the range of $[2100\mu s:\ 4270\mu s]$. The FSE procedure was performed in sequence with a given gradual change in f_0 frequency, therefore a portion of the group velocity dispersion curve covering the frequency range of 20 to 60 kHz was measured and validated via DISPERSE in Figure 4.12. Quantified results are also available in Table 4.2.
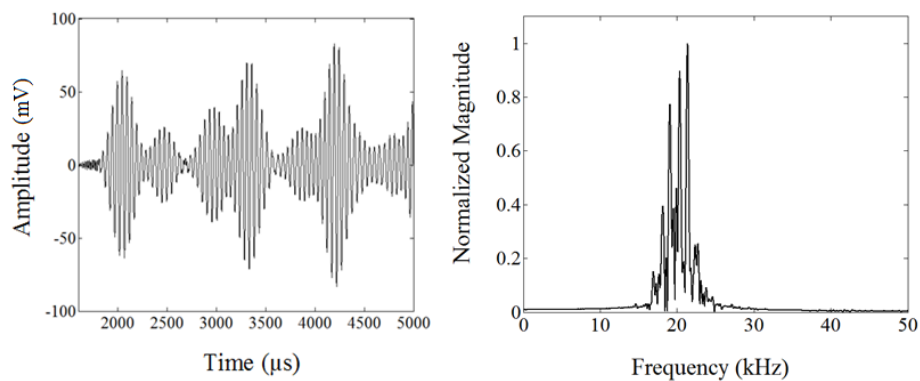
Figure 4.8: (Left) Acquisition signal at f_0 (20 kHz) and (right) Fourier transformed
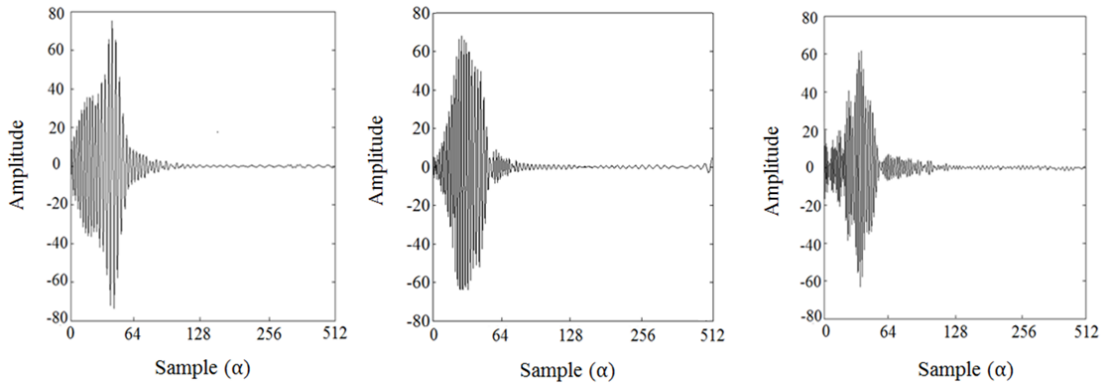
Figure 4.9: (left) ASW at 2300-μs (middle) ASW at 3500-μs (right) ASW at 4300-μs
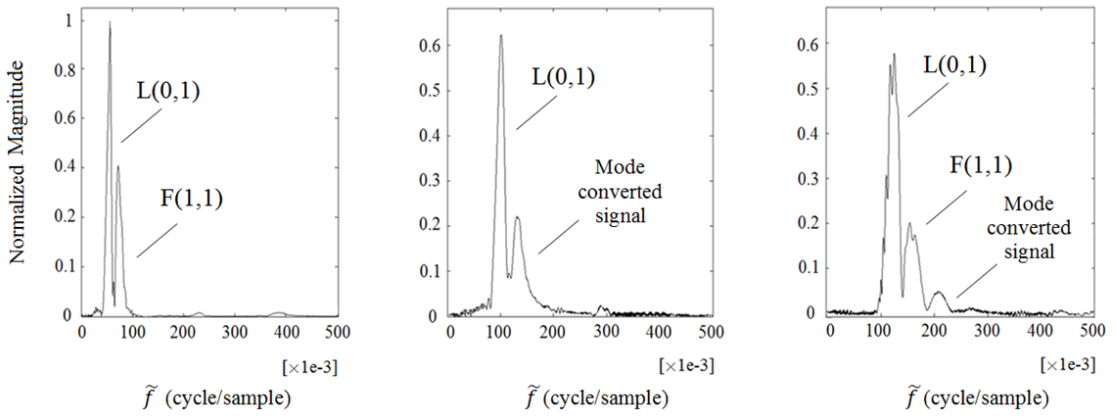
Figure 4.10: FSS at (left) 2300-μs, (middle) 3500-μs, (right) 4300-μs
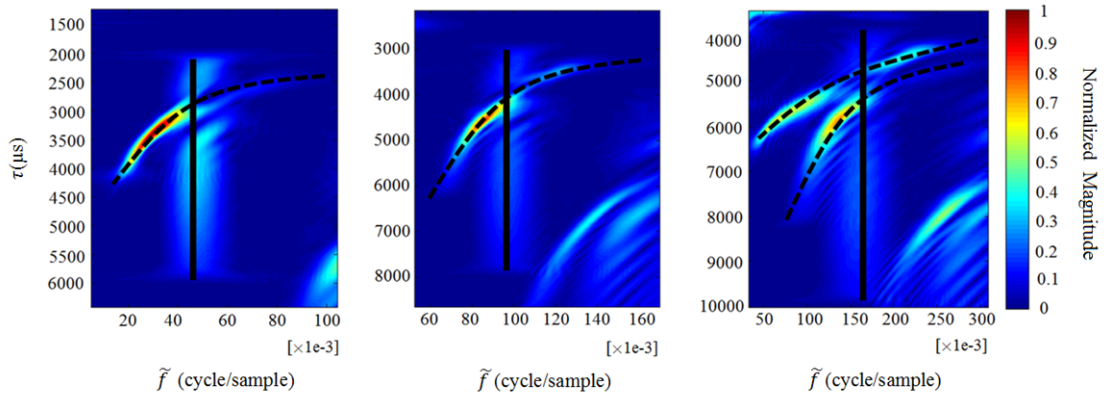
Figure 4.11: TFSS Image of (left) 2nd echo-L(0,1) and 1st echo-F(1,1), (middle) 3rd echo-L(0,1) and 1st echo-mode converted signal, (right) 4th echo-L(0,1), 2nd echo-F(1,1) and 2nd echo-mode converted signal

According to the given results, the proposed technique shows promise for wave mode identification in a multimodal UGW signal. It is also demonstrated to have
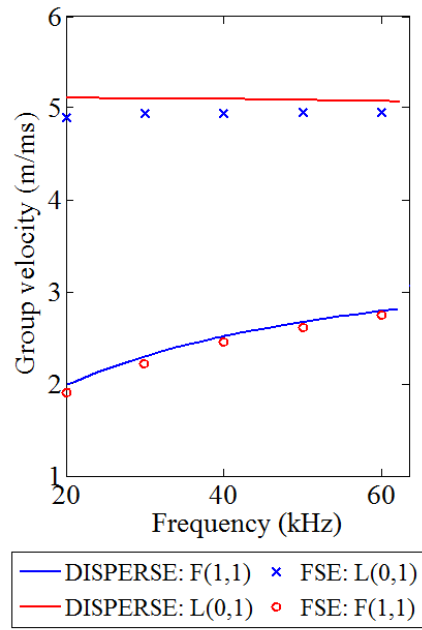
Figure 4.12: Validation of experimental group velocity dispersion curve

the capability to plot the group velocity dispersion curve of an aluminium rod. Therefore; the technique is mostly expected to be suitable for reliable inspection of one dimensional structures (*e.g.* wires, bars, pipes, rails, *etc.*) in field inspections, since it requires a frequency-sweep pulse-echo measurement.

	FSE: Experiment		
Technique Wave mode type	*ToA*	v_{gr}	v_{gr} *error*[17]
F(1,1)	2290 $[\mu s]$	1877 $[m/s]$	%5.91
L(0,1)	1775 $[\mu s]$	4845 $[m/s]$	%5.00
Mode converted signal	3308 $[\mu s]$	N/A	N/A

Table 4.2: Extracted wave mode information (experiment)

---
[17]The errors for the extracted the group velocities by the FSE technique are calculated based on the results given by DISPERSE software. Thus the errors only represent the discrepancy between the two provided results.

It is notable that the time domain separation has not been performed in this chapter as the aim of the chapter was wave mode identification capability focused in Fourier domain. According to the wave mode identification capability of the proposed technique that have been highlighted throughout the chapter, the author suggest employing customized filters on FSS responses in order to extract individual time domain wave forms, therefore it could also be particularly beneficial in other practical applications *e.g.* defect sizing and attenuation measurements out in the field.

4.5   Chapter summary

In this chapter a Frequency-Sweep Examination (FSE) technique was introduced and shown to be a promising technique for structural feature detection in complex UGW inspections. It has been empirically demonstrated that the proposed signal processing technique is useful for ToA/group velocity extraction and wave mode identification of superposed UGWs. The technique was able to detect the number of wave modes present with accurate quantitative information allowing a portion of group velocity dispersion curve to be computed.

The assumption of a known propagation distance is a drawback of the technique which needs to be taken into account in field inspection as well as the one presented by TFR methods [69] and [72]. In addition, the time domain separation has not been performed as the chapter is mainly focused on wave mode identification which was achieved in Fourier domain. According to the wave mode identification capability of the proposed technique, customized filtering in FSS domain can be a possible solution to such a requirement.

The advantage of this approach over a spatial 2D-FFT or SVD measurements is on performing pulse-echo frequency-sweep excitations of UGWs rather than several pitch-catch measurements. Moreover, the use of FSE enables the empirical computation of the dispersion curve which overcomes the need for *a priori* knowledge where it is needed for dispersion compensation methods [72].

Chapter 5

Iterative Dispersion Compensation Based Pulse Compression in Multimodal UGW responses

5.1 Chapter overview

In this chapter, a signal processing technique is proposed which considers a broadband chirp for excitation and employs iterative dispersion compensation and cross-correlation in order to identify the wave modes of interest in a multimodal UGW response. The technique derives accurate quantitative information (ToA & propagation distance) using *a priori* knowledge of the dispersion curves for structural feature detection. The technique is applied to synthesized and experimental data taken from an aluminum rod for performance verification. The consequent improvement in SNR is quantified.

A part of the research conducted in this chapter has been presented in *IEEE International Conference on Industrial Informatics (INDIN)*, Cambridge, United Kingdom, on July 2015 and has been submitted to *IEEE transactions on Industrial Informatics* as a result of invitation from the journal. Also, resulted in a submitted publication in *IEEE Transactions on Ultrasonics, Ferroelectrics and Frequency Control* [**SF 03**], [**SF 06**]-[**SF 07**].

The background theory of this chapter was covered in Section 2.5. The proposed technique is described in Section 5.2. A signal synthesis was performed in order to evaluate the performance of the proposed technique for unimodal and

multimodal responses in Section 5.3. The experimental validations are covered in Section 5.4 where the SNR improvements are quantified. The performance of the proposed technique is summarized in Section 5.5 followed by conclusions and recommendations for future works.

5.2 An Iterative Dispersion Compensation (IDC) based pulse compression

UGWs experience dispersion as they propagate through a medium. It was discussed in Chapter 3 in the context of Signal Processing for UGWs, with sufficient mathematical implementation from Wilcox that a dispersed signal defined in (3.1) could be compensated for dispersion via (3.3) which compensates for frequency-dependent velocities of the wave modes. The compensation process however, requires *a priori* knowledge of dispersion curve and the propagation distance for accurate compensation, which makes it infeasible for real life applications especially where long range ultrasonic testing is of concern.

Recently published literature [**59**], [**60**] shows, that a dispersion compensated UGW response can possess an improved SNR with a better feature localization for a dispersive wave mode. However, in multimodal scenarios where signals are superposed, the interpretation of received signals can become challenging and dispersion compensation may not necessarily deliver a useful outcome. As was discussed in Chapter 3, in the context of *Broadband Excitation and Pulse Compression of UGWs*, in such cases, pulse compression techniques can be potentially used to increase the ability to improve the SNR as well as accurate feature localization. Chirp could be potentially an ideal candidate for such a requirement since it has δ-function like autocorrelation values (Figure 5.2–(middle)). Here, a novel signal processing technique is presented [**SF 03**] which was developed concurrently by Yucel *et al.* [**SF 06**]–[**SF 07**].

Figure 5.1 illustrates the block diagram of the whole technique. A dispersion compensated UGW response, $h_d(t)$ can ideally have a good cross-correlation with the excitation signal, $x(t)$, assuming that $\tilde{x}(t)$ represents the dispersed signal. Thus, the maximum value of the cross correlation of $\tilde{x}(t)$ and $h_d(t)$, $\max(\mathrm{ccf}(h_d(t),x(t)))$ may provide accurate localization of the UGW response. The technique proposed in this study combines the dispersion compensation technique with the pulse compression in a brute-force search manner. The dispersed signal $\tilde{x}(t)$ is iteratively dispersion compensated, $\left[h_{d(1)}, \ldots, h_{d(n)}\right]$ for a range of pre-defined prop-

agation distances, $[d(1), \ldots, d(n)]$ and cross-correlated with the excitation signal $\left[ccf_{d(1)}(t), \ldots, ccf_{d(n)}(t)\right]$ in order to obtain the compressed pulse. In each iteration, the maximum cross-correlations are obtained, $\left[max(ccf_{d(1)}(t)), \ldots, max(ccf_{d(n)}(t))\right]$ and the respective maxima in time are stored in an array where the peak of that array denotes the ToA and the propagation distance. Such analysis may extract the propagation distance for individual wave modes automatically.

5.3 Signal synthesis

A linear positive chirp with (250 samples with sampling frequency of 1-MHz) possessing frequency components between 10 to 120 kHz was synthesized. Figure 5.2 illustrates the waveform of interest with its respective auto-correlation and spectrogram. The synthesis [60] is performed for an 8 mm diameter aluminium rod in order to evaluate the performance of the technique in unimodal (Section 5.3.1) and a multimodal scenarios (Section 5.3.2). Group velocity dispersion curves for the wave modes propagating through the structure are given in Figure 2.4 and overlaid with relevant spectrograms in Figure 5.3.
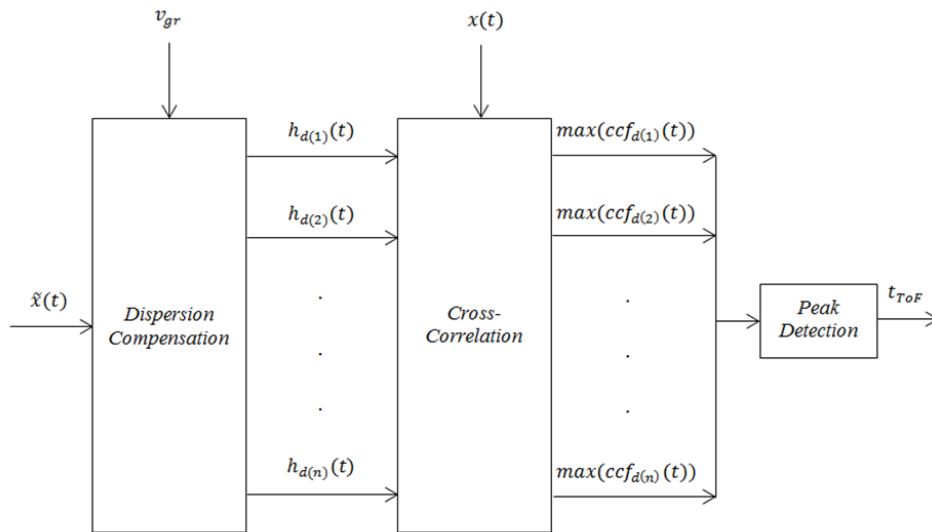

Figure 5.1: Block diagram for the proposed technique

5.3.1 Unimodal synthesis

The chirp is dispersed [92] assuming a travelled path of 4.3 meters for the fundamental flexural wave mode F(1,1) and 8.6 m for the fundamental longitudinal wave mode, L(0,1). Figure 5.3–(left) illustrates the spectrogram of the dispersed
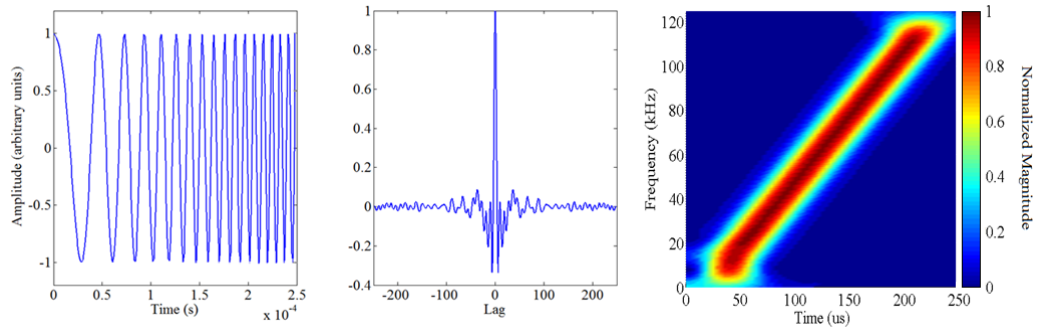
Figure 5.2: Synthesized (left) positive chirp waveform with (middle) its auto correlation and (right) spectrogram.

F(1,1) signal. The spectrogram shown for the chirp (dashed line) possesses an offset value of its time duration (250 μs) when compared with its dispersion curve (solid line). This is due to the time-variant broadband nature of the chirp where its dominant frequency varies with time. Figure 5.3–(right) shows the spectrogram for the successful compensation of dispersive F(1,1) wave mode (dashed line) at 20 kHz centre frequency and overlaid group velocity dispersion curve (solid line). The magnitudes beyond -35 dB have been ignored in the spectrogram plots. It should be noted that all the normalized results provided throughout the chapter is performed against the maximum values.

The proposed iterative search technique is applied to the synthesized signals for a variety of distances ranging from 0 to 10 m with a step size of 1 mm. The step size was chosen based on the measured smallest wavelength of the wave modes of interest. Figure 5.4 shows the dispersed signal, dispersion compensated signal and cross correlated signal (compressed pulse) for F(1,1) and L(0,1) wave modes. It can be observed in Figure 5.4 that the SNR of the compressed pulse after IDC is considerably improved. SNR values throughout the chapter are measured in dB scale using [94], [95]:

$$SNR = 20log(P/\sigma) \tag{5.1}$$

where P is the peak value of the target zone and σ is the standard deviation of the whole trace. Results of the SNR improvement are given in Table 5.1. It can be seen that the chirp achieved up to 13.15 dB improvement for the wave modes of interest.

Maximum cross-correlation values are acquired as the ToA (Table 5.3) of the mode of interest, therefore the propagation distances (4.3 m and 8.6 m for F(1,1) and L(0,1) wave modes respectively) are extracted as shown in Figure 5.5.

5.3.2   Multimodal synthesis

Two wave modes, F(1,1) and L(0,1) are synthesized and superposed to evaluate the effectiveness of the technique in a multimodal scenario. The broadband chirp is dispersed for the propagation distance of 4.3 meters for the F(1,1) wave mode and 8.6 meters for the L(0,1) wave mode simultaneously. Figures 5.6–(left) and (right) show the spectrograms of the dispersed pulse and the dispersion compensated pulse at 20 kHz centre frequency. It is evident that the F(1,1) wave mode is compensated for dispersion accurately whereas the L(0,1) wave mode is further dispersed since the two wave modes possess different dispersion properties.

The iterative search technique is applied on the aforementioned waveform for a range of distances between 0 to 10 m with a step size of 1 mm (it is notable that the brute-force search can be implemented in Matlab software with minimal computational time, less than 3 mins for the step size of 1 mm covering 0 to 10 mm). Figure 5.7 and Figure 5.8 show the superposed dispersed pulses, compensated and compressed for F(1,1) and L(0,1) wave modes respectively.

It can be also observed in Figure 5.7 and Figure 5.8 that the SNR of the compressed pulse is enhanced considerably with respect to the original superposed dispersed pulses. Quantification of the SNR improvement for multimodal signals is shown in Table 5.1. Figure 5.9 illustrates the maximum cross-correlation amplitudes for the wave modes of interest where the peaks observed in the figure indicate the propagation distance. The iterative technique therefore extracted the accurate ToA and propagation distance of 2156 μs and 4.3 m for F(1,1) wave mode and 1686 μs and 8.6 m for L(0,1) wave mode in the multimodal response.
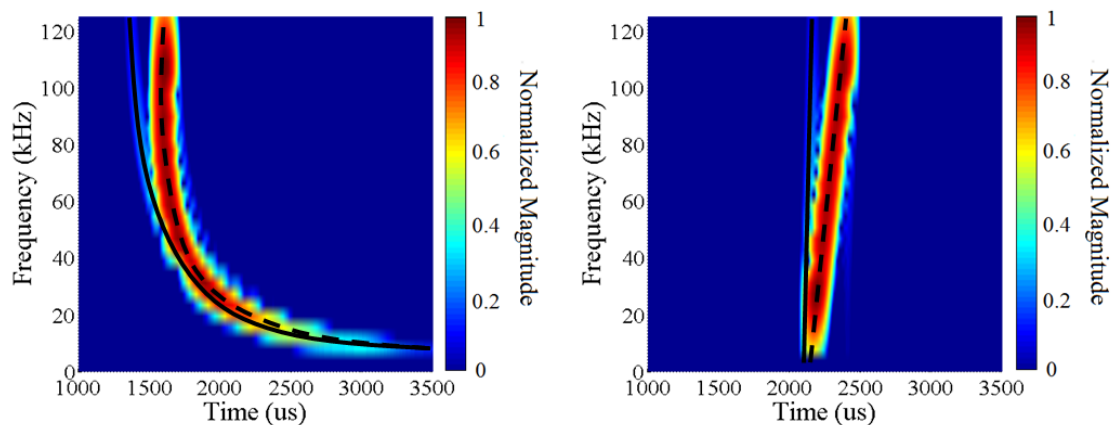
Figure 5.3: Spectrogram of (left) synthesized F(1,1) and (right) compensated F(1,1) with the overlaid group velocity dispersion curve: solid line, group velocity F(1,1), dashed line, theoretical curve.
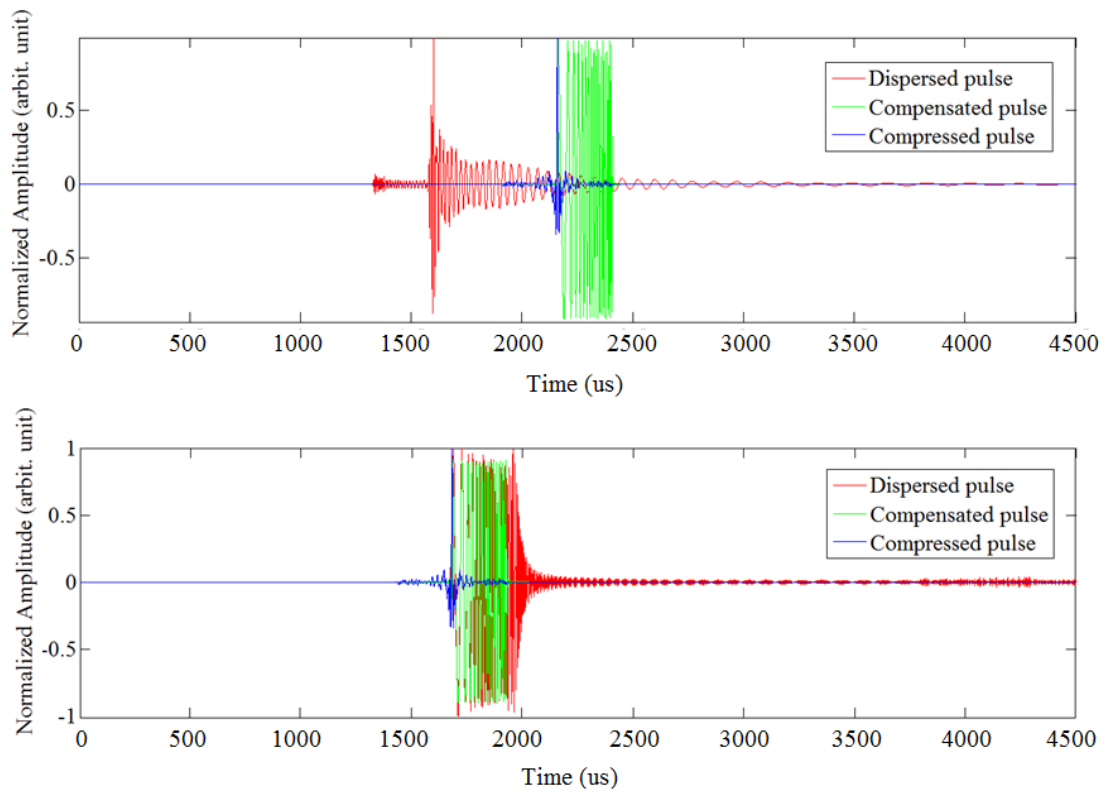
Figure 5.4: Synthesis of (top) F(1,1) and (bottom) L(0,1) wave modes: (red) dispersed for 4.3 and 8.6 meters respectively (green) dispersion compensated wave modes and (blue) compressed wave modes
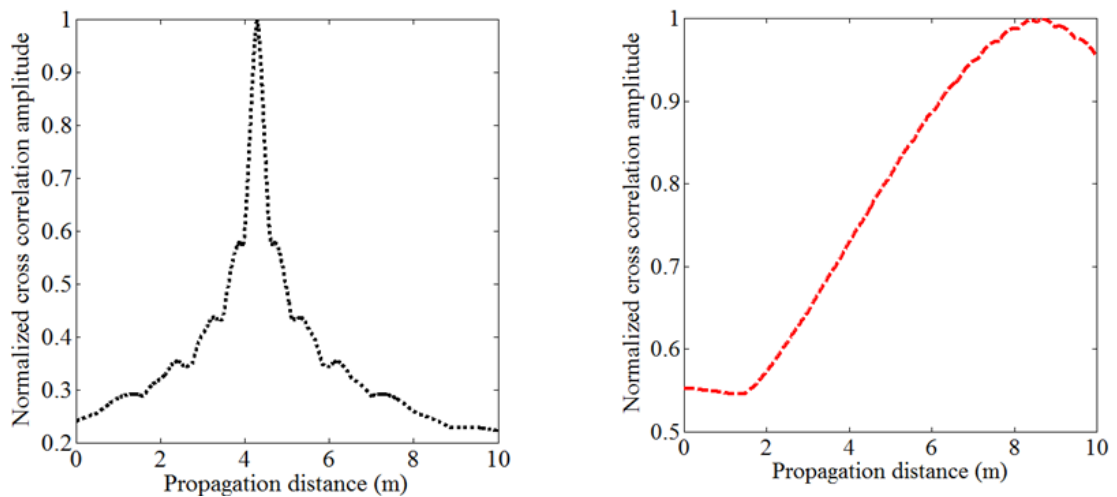
Figure 5.5: Maximum cross correlation amplitude for the propagation distance of (left) F(1,1) and (right) L(0,1) wave modes
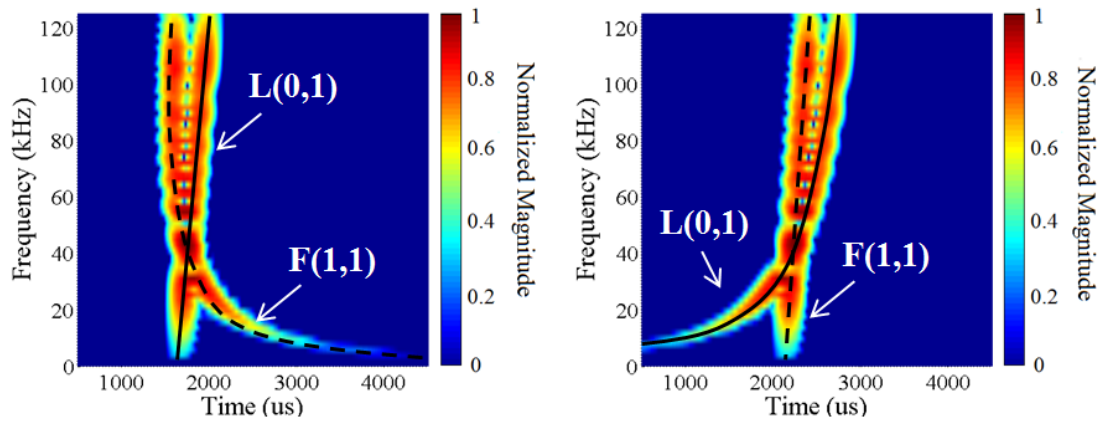
Figure 5.6: Spectrogram of (left) synthesized superposed pulse containing F(1,1) and L(0,1), (right) compensated F(1,1) with the overlaid theoretical curve: (solid line, L(0,1)), (dashed line: F(1,1))
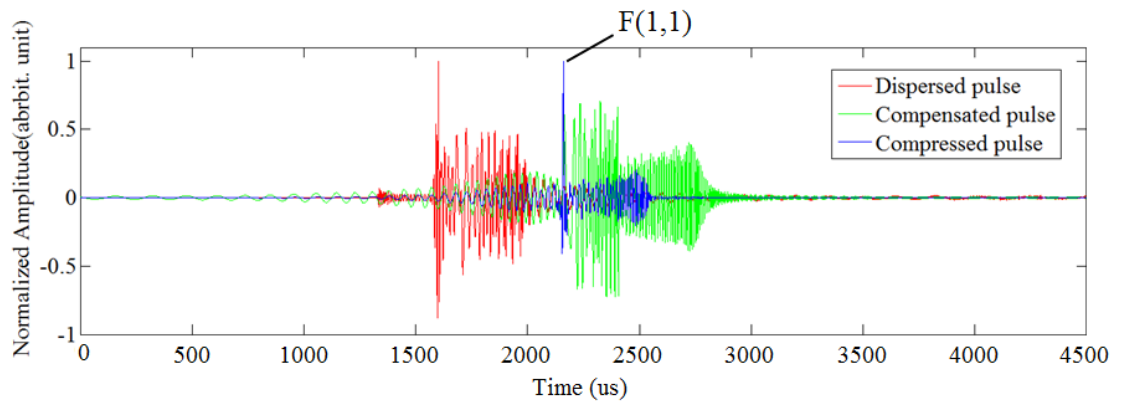
Figure 5.7: Synthesis of (red) superposed pulse containing F(1,1) and L(0,1) wave mode (green) compensated F(1,1) and (blue) compressed pulse
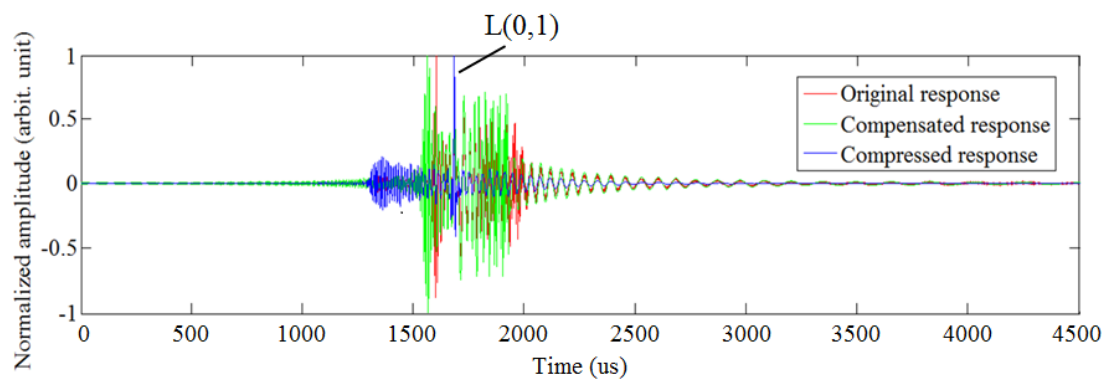
Figure 5.8: Synthesis of (red) superposed pulse containing F(1,1) and L(0,1) wave mode (green) compensated L(0,1) and (blue) compressed pulse
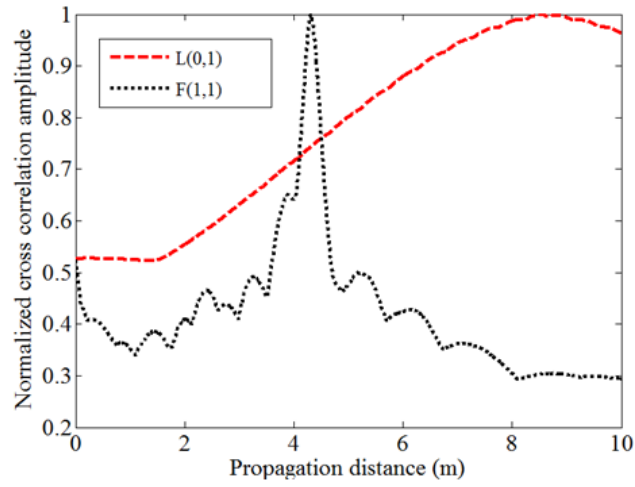
Figure 5.9: Maximum cross correlation amplitudes for the propagation distance of F(1,1) and L(0,1) wave modes

SNR results / Multimodal Synthesis	Original SNR (dB)	Conventional dispersion compensation		Iterative dispersion compensation based pulse compression	
		SNR (dB)	SNR Increase (dB)	SNR (dB)	SNR Increase (dB)
F(1,1)	29.44	22.63	-6.81	38.22	8.78
L(0,1)	29.44	26.35	-3.08	38.14	8.69
Uni-Modal Synthesis					
F(1,1)	32.50	35.31	2.81	41.16	8.66
L(0,1)	27.95	29.03	1.08	41.10	13.15

Table 5.1: SNR values of the single wave mode and multimodal synthesis

5.4 Experimentation

5.4.1 Experimental setup

The same experimental setup explained in Section 4.4 and illustrated in Figure 4.7 were used. The same excitation waveform (broadband chirp) as used in the Section 5.3 (signal synthesis) is selected. It must be noted that the excitation signals could be affected by the transfer function of the hardware and the transducer. The frequency response [96] of the hardware components is important because this may alter the excited signal; which can lead to deterioration of the cross correlation and dispersion compensation steps of the proposed technique [97]. Therefore, the signal generated by the Teletest unit has been extracted (Figure 5.10) using an oscilloscope[18] and fed into the proposed technique before the application of cross-correlation.

5.4.2 Experimental results

In order to evaluate the effectiveness of the technique experimentally, two separate multimodal responses are acquired. The responses under investigation are as follows[19]:

1. Superposition of the L(0,1) and F(1,1)

    (a) Identification of F(1,1) wave mode

    (b) Identification of L(0,1) wave mode

2. Superposition of the L(0,1) wave mode and a mode converted signal

    (a) Identification of a mode converted signal

---

[18]The oscilloscope was used to observe the voltage of the waveform generated by the Teletest unit with a piezoelectric transducer as a load. The voltage best approximates the stress induced by the transducer.

[19]The experiments were repeated three times and the standard error was found to be less than %5.

5.4.3 Superposition of L(0,1) and F(1,1) wave mode

a. *Identification of F(1,1) wave mode in a multimodal response*

The spectrogram of the aforementioned multimodal response for chirp is illustrated in Figure 5.11–(a)–left with fully compensated F(1,1) wave mode in Figure 5.11–(a)–right. Figure 5.12–(a) illustrate the original multimodal response, compensated F(1,1) wave mode of the multimodal response and the compressed response. The iterative search for the cross correlation maximum is performed for the ranges between 1.5 and 10 m with a step size of 1 mm. Based on the empirical findings, this minimum distance threshold value is chosen as 1.5 m since most of the responses are masked by the ringing response and the switch on spike of the transducer. The peak observed in the compressed response (Figure 5.12–(a)) represent the existence of F(1,1) at the ToA of 2305 μs and the propagation distance of 4.39 m (error$\approx\%$2.1) as shown in Figure 5.13–(left). The SNR improvements for the individual identified wave modes are provided in Table 5.2.

b. *Identification of L(0,1) wave mode in a multimodal response*

The iterative technique as was employed based on the dispersion compensation of the longitudinal wave mode L(0,1). The results are shown in Figure 5.12–(b) represent the original response, with compensated L(0,1) and the compressed response. The maximum cross-correlation values are acquired as the ToA of the mode of interest and plotted against the propagation distance in Figure 5.13. It can be observed that the propagation distance of the L(0,1) wave mode could not be extracted. It is known that the longitudinal wave mode, L(0,1) undergoes very low dispersion, in the frequency range of 20 to 100 kHz, and was nominally considered as a non-dispersive wave mode. Therefore, the dispersion compensation could not have an effect on the original signal (shown in Figure 5.11–(b)) causing the majority of the distant trace ($x(m)$, from 1.5 m to 12 m) to possess a correlation range of [0.9 to 1] (shown in Figure 5.13). However, the sharp peak observed in the compressed response appears at a constant time in the frequency range of interest since the L(0,1) wave mode experiences very low dispersion. This peak represents the ToA of the longitudinal wave mode, L(0,1) at 1786 μs thus could be converted to the propagation distance of 9.10 metres (error$\approx \%$5.81) using (4.6). Thus, in such regard, a hybrid approach can be used to extract the ToA of the non-dispersive wave modes and convert the extracted ToA into the propagation distance. Quantification of the SNR improvement for longitudinal-based compensation of experimental signals is given in Table 5.2.

5.4.4 Superposition of L(0,1) wave mode and the mode converted signal

a. ***Identification of the mode converted signal in a multimodal response***

Here, the mode conversion occurred due to the fact that the transducer was clamped on the end of the rod. The rod surface is in contact with the piezoelectric ceramic at an arbitrary point on the circumference and the reactive force of the clamp surface is in contact with the rod directly $180°$ to the aforementioned arbitrary point. The location where the transducer and clamp are situated produces a feature on the rod hence, after the reflection of the waves from the end of the rod with the attached the clamp and the transducer, either the longitudinal wave converts to a flexural wave and/or a generated flexural wave has been converted into a longitudinal mode. This phenomenon has been investigated in detail in Chapter 6. The mode converted signal was investigated in an echo of the multimodal response overlapping with L(0,1) wave modes at 20-kHz. The spectrogram of the response is given in Figure 5.11-(c) with the compensated mode converted signal based on F(1,1) wave mode dispersion properties. The dispersion compensation on the mode converted signal has been performed based on the F(1,1) wave mode dispersion properties since the mode converted signal follows the same time/frequency response as F(1,1). Figure 5.12–(c) represents the original time domain response, the dispersion compensated response and the compressed pulse respectively. It can be observed that the mode converted signal could be identified (ToA: 3306 μs) after the application of dispersion compensation and possessing higher SNR properties after pulse compression (Table 5.2). The maximum cross-correlation values are acquired as the ToA of the wave mode of interest and plotted against the propagation distance as shown in Figure 5.13–(right). It is evident that the propagation distance of the mode converted signal could not be extracted as a dominant peak although the relevant peak appeared at 8.71 m, error $\approx \%1.3$. The amplitude of the mode converted signal is approximately 20 dB less than the dominant L(0,1) therefore the maximum cross-correlation amplitudes of the mode converted signal could not overcome the dominance of the L(0,1) wave mode. Thus, in such regard, human interactions may be required to perform wave mode identification and obtain the ToA of the wave mode of interest.

Figure 5.12–(d) represents the original time domain response, the dispersion compensated response based on the L(0,1) wave mode and the compressed pulse re-

spectively. It can be observed that the L(0,1) wave mode could be identified (ToA: 2707 μs) after the application of dispersion compensation. The maximum cross-correlation values are acquired as the ToA of the wave mode of interest and plotted against the propagation distance as shown in Figure 5.13–(right). It is evident that the propagation distance of the mode converted signal could not be extracted as was described previously in Section 5.4.3. However, the ToA could be converted to the propagation distance of 13.7 (error $\approx$ %6.2) using *a priori* knowledge of the dispersion curve.

SNR results Multimodal Experiment	Original SNR (dB)	Conventional dispersion compensation		Iterative dispersion compensation based pulse compression	
		SNR (dB)	SNR Increase (dB)	Improved SNR (dB)	SNR Increase (dB)
F(1,1)	22.46	16.48	-5.98	26.48	4.02
L(0,1)	22.46	22.03	-0.42	25.97	3.50
Mode converted signal	N/A	14.3	N/A	18.9	N/A

Table 5.2: SNR values of the experimentations
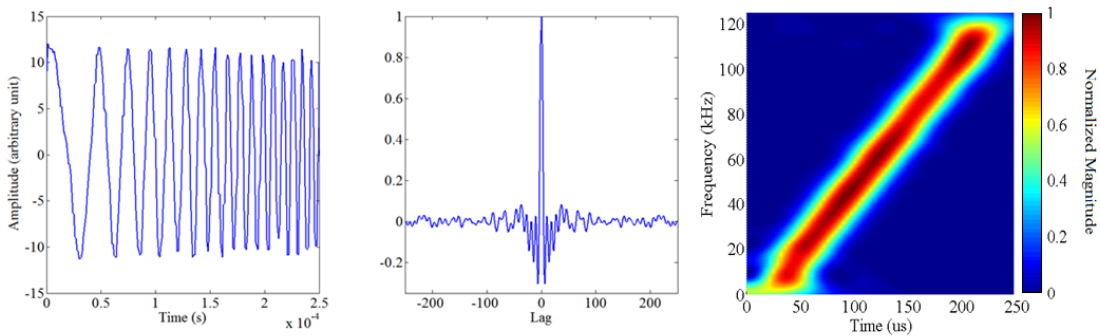
Figure 5.10: Chirp waveform generated by the Teletest unit (left) time domain and (middle) its auto correlation and (right) spectrogram
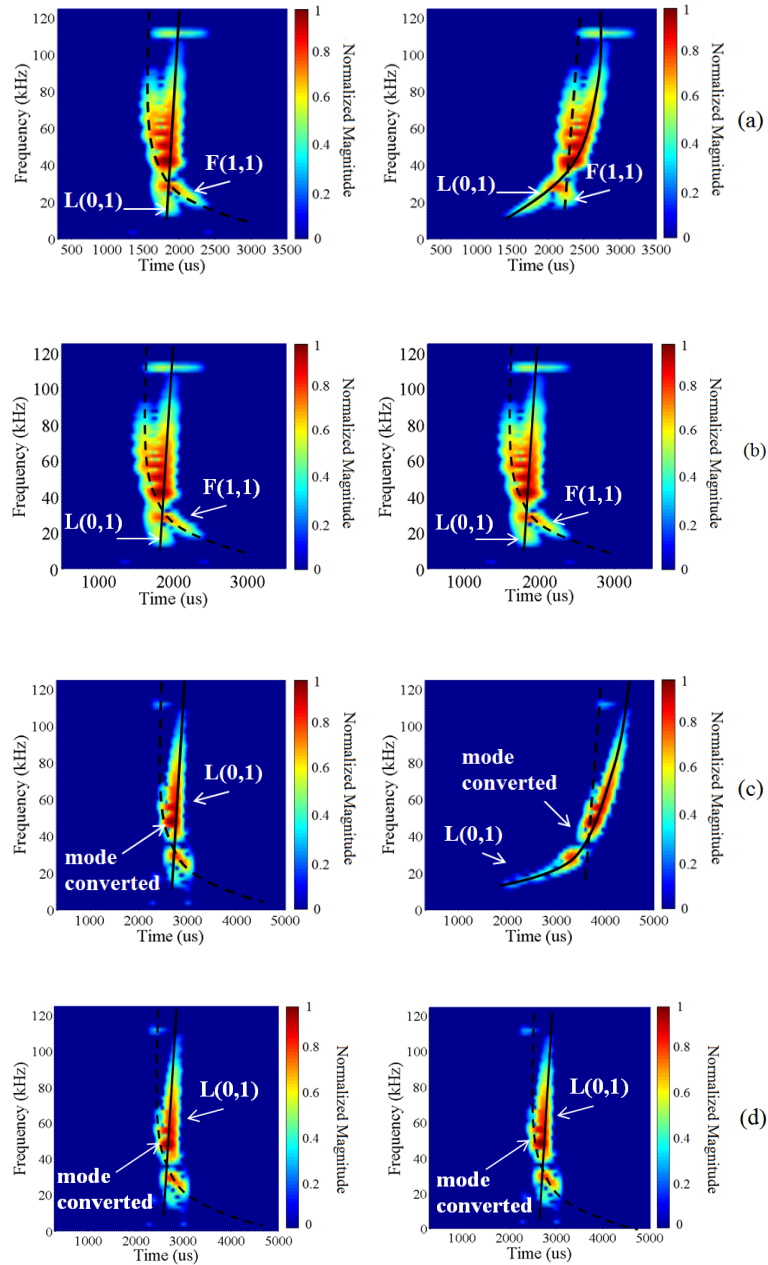
Figure 5.11: Spectrogram of (a)–left: superposition of F(1,1) and L(0,1), right: compensated F(1,1), with the overlaid theoretical curve: (solid line, L(0,1)), (dashed line: F(1,1)). (b)–left: superposition of F(1,1) and L(0,1), right: compensated L(0,1), with the overlaid theoretical curve: (solid line, L(0,1)), (dashed line: F(1,1)). (c)–left: superposition of L(0,1) and the mode converted signal, right: compensated F(1,1) with the overlaid theoretical curve: (solid line, L(0,1)), (dashed line: mode converted), (d)–left: superposition of L(0,1) and the mode converted signal, right: compensated L(0,1) with the overlaid theoretical curve: (solid line, L(0,1)), (dashed line: mode converted)
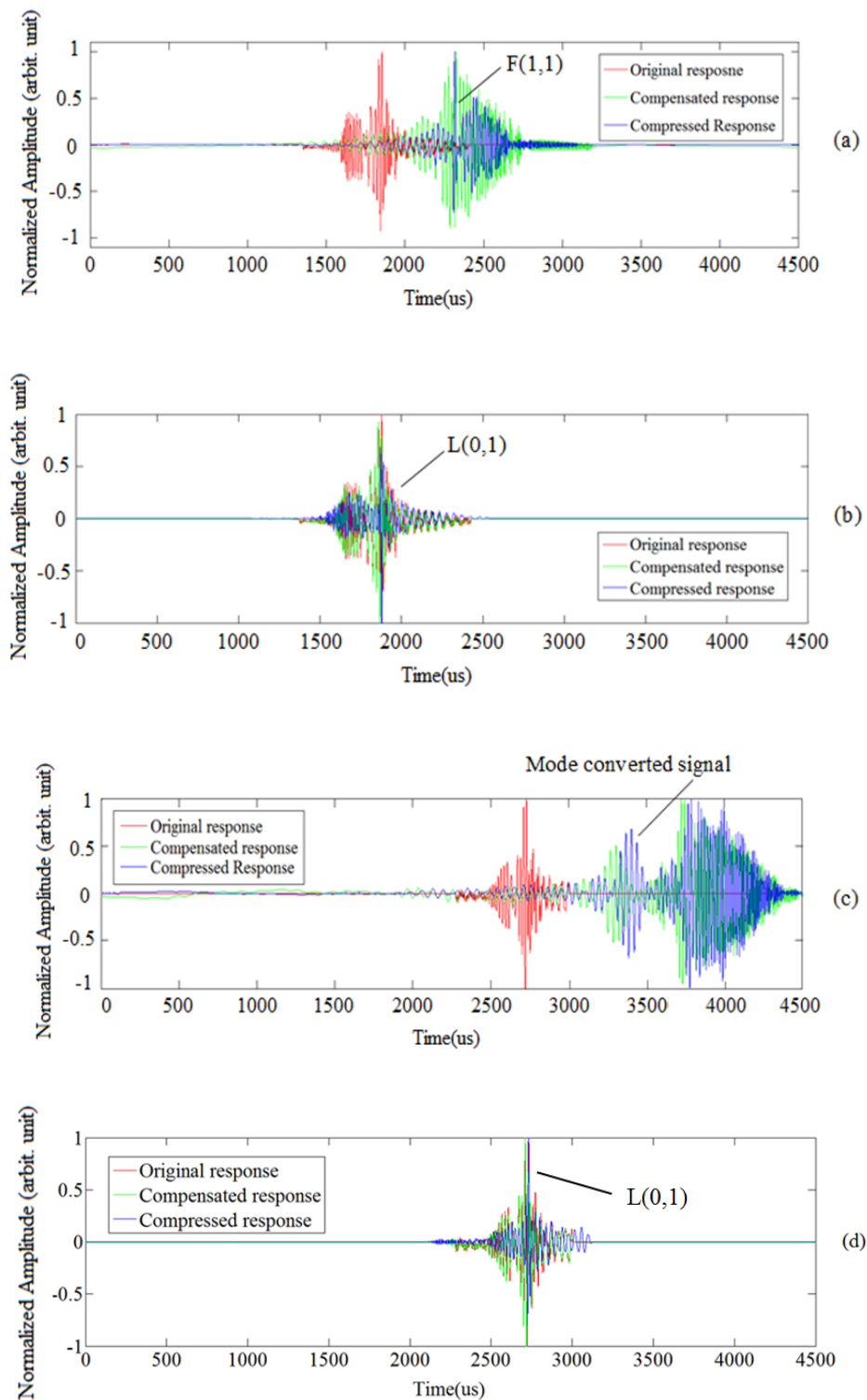
Figure 5.12: Identification of (a) F(1,1), 1st echo and (b) L(0,1), 2nd echo after superposition of the two and identification of (c) the mode converted signal, 1st echo and (d) L(0,1), 3rd echo after superposition of the two.
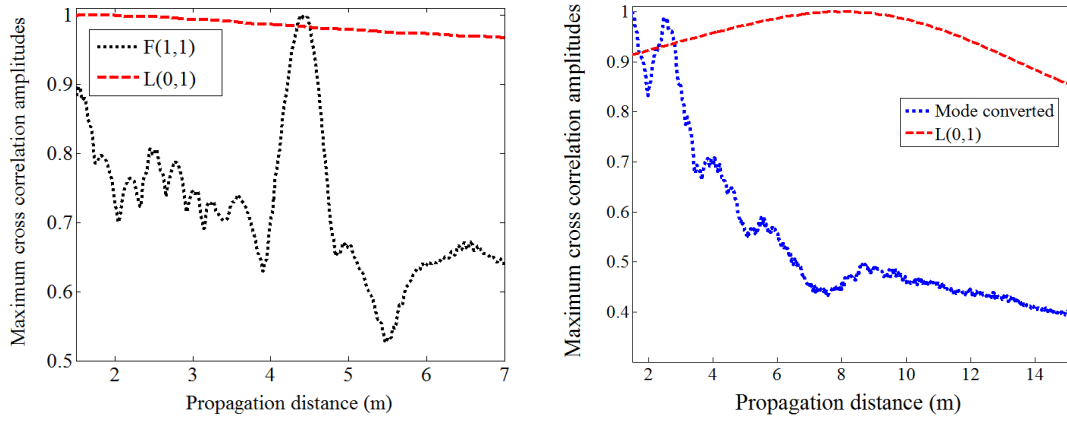
Figure 5.13: Maximum cross-correlation amplitude for the propagation distance of (Left) F(1,1), 1st echo and 2nd echo of L(0,1) wave modes, (Right) the mode converted signal, 1st echo and 3rd echo of L(0,1) wave mode

Wave mode type	Technique	Experiment: IDC based pulse compression			Synthesis: IDC based pulse compression	
		ToA	Prop.	Prop. error[20]	ToA	Prop.
F(1,1)		2305 [μs]	4.39 m	%2.10	2156 [μs]	4.30 m
L(0,1)		1786 [μs]	9.10 m	%5.81	1686 [μs]	8.60 m
Mode converted signal		3306 [μs]	8.71 m	%1.30	N/A	N/A

Table 5.3: Quantitative information (experiment)

[20]The errors for the extracted the group velocities by the FSE technique are calculated based on the results given by DISPERSE software. Thus the errors only represent the discrepancy between the two provided results.

5.4.5 Highlights and recommendations for future works

- The results provided in Figure 5.13 indicated that the IDC based pulse compression technique extracted the propagation distance of the F(1,1) wave mode with minor errors (up to %2.1) when compared to the wavelength of the wave modes of interests. However, the technique could not manage to extract the propagation distance of the L(0,1) wave mode as a form of an independent peak. It is known that L(0,1) wave mode experienced very low dispersion in the operating frequency region. Therefore the dispersion compensation technique could not have any effect on the shape of the wave form in order to be cross correlated with the reference chirp wave form shown in Figure 5.10–(left). However, the sharp peak observed in the compressed response (Figure 5.12–(b)) represents the ToA of the L(0,1) wave mode at 1786 μs corresponding to the propagation distance of 9.10 metres (error $\approx$ %5.81).

- It should be noted that the frequency response of the transducer and the hardware is an important factor for the application of the proposed technique. As was seen in Section 5.3.2 in the context of *multimodal synthesis*, the results (ToA and propagation distance) were obtained with no errors. However, due to measurement noise and transducer/hardware affect the ToA and/or the propagation distances were obtained with minor errors. Therefore, it must be noted that the technique is potentially expected to generate results with higher accuracy if the dispersion compensated responses are cross-correlated with the actual signal generated by the transducer.

- The results provided in Table 5.2 specify that the proposed technique is suitable for SNR enhancements of the UGWs where multimodal responses are of concern. It was shown that the dispersion compensation technique may not possess any SNR improvement when applied to a multimodal response. Despite the fact that the dispersion compensation technique for uni-modal response produced considerable SNR improvements as shown in Table 5.1 and highlighted in the previous studies [63], [62], [60], [59], [84].

- The accuracy of the dispersion curve also plays an essential role in the extraction of the ToA and/or the propagation distance where dispersion compensation is of concern. Since all of the dispersion compensation techniques use *a priori* knowledge of the dispersion curve for accurate compensation,

it is recommended that the dispersion curves are empirically measured to be fed to the dispersion compensation algorithm thus the technique could potentially produce better results.

- The original SNR values given in Table 5.1 and Table 5.2 were calculated based on the peak value of the original response. It must be noted that the peak value of the original response does not necessarily represent the peak value of the wave modes of interest (L(0,1) and F(1,1)) since they are heavily superposed and could not be directly identified. Therefore the SNR increase values given in Table 5.2 may potentially have higher rise when compared with the actual SNR of the wave modes.

- As was mentioned in Chapter 4 the FSE technique facilitates the extraction of ToA of individual wave modes in a superposed wave-packet and uses *a priori* knowledge of the propagation distance to measure the group velocity dispersion curve. The IDC technique on the other hand extracts the ToA using *a priori* knowledge of the dispersion curve and also enables considerable SNR enhancement (Table 5.1 and Table 5.2). It is notable that the application of the IDC technique may be restricted when the type of the structure is complex and dispersion curves are not available for that. FSE technique on the other hand uses *a priori* knowledge of the propagation distance to measure the dispersion curve therefore the application of the technique could be further enhanced if the length of propagation is unknown. Thus the IDC technique and FSE could be combined to compute the dispersion curve and also enhance the SNR simultaneously in an automated computerized process with no manual intervention which is recommended for the future work.

5.5 Chapter summary

In this chapter, a novel iterative technique comprising dispersion compensation and pulse compression was proposed. The technique extracted the ToA and iteratively searched for the propagation distance of individual wave modes using *a priori* knowledge of group velocity dispersion curves. Signal synthesis for the unimodal and multimodal cases successfully extracted the ToA and the propagation distance of individual wave modes. According to the experimental results the ToA and the corresponding propagation distance of the dispersive flexural wave mode could be extracted with up to %2.1 error. Moreover, considerable SNR improvements in

the signal synthesis and experimental validation (Table 5.1 and Table 5.2) were achieved for individual wave modes.

It was empirically demonstrated that the proposed technique is best suited for the identification of dispersive wave modes (*e.g.* F(1,1) wave mode) and may not successfully derive the propagation distance of the fundamental longitudinal wave mode (L(0,1)) since it experienced very low dispersion in the operating frequency region. Therefore the dispersion compensation technique could not have a major effect on the shape of the wave form in order to be cross correlated with the reference chirp wave form and extract the propagation distance. However, in such regard, the sharp peaks for the non-dispersive wave modes appear at a constant time in the frequency range of interest. This peak represents the ToA of the longitudinal wave mode, L(0,1) and can be converted to the propagation distance since the group velocity dispersion is known.

During the experimental validations the dispersion compensated responses were cross-correlated with the signal generated by the Teletest unit. Therefore, it is also expected that the errors in the extraction of the propagation distance to be further reduced if the dispersion compensated responses are cross-correlated with the signal generated by the transducer. This may require careful vibrometry measurements which can be a time consuming process for field inspections. It is intended to perform such an experiment in the future research studies. In addition, since the dispersion compensation technique is highly dependent on the accuracy of the dispersion curve the precision of the extracted quantitative information such as ToA and the propagation distance could be further promised if the dispersion curves are experimentally acquired.

The IDC presented in this chapter and FSE technique presented in Chapter 4 use *a priori* knowledge of the propagation distance and the group velocity dispersion curve respectively to measure the ToA of the individual wave modes. Thus the two techniques could be combined to compute the dispersion curve and also enhance the SNR at the same time in an automated computerized process with no manual intervention which is recommended for the future works.

Chapter 6

Investigation of UGWs Interacting with Piezoelectric Transducers

6.1 Chapter overview

In this chapter, a novel investigation of the interaction of UGWs with piezoelectric transducers is presented. According to the best of author's knowledge the UGWs interacting with the piezoelectric transducers have not been reported and/or investigated in the field of guided waves. A Finite Element Analysis (FEA) approach is used to conduct a parametric study in order to quantify the effect of the waveguide diameter on the UGW response. Laboratory experiments are designed to measure the effect of the force on the dry-coupled piezoelectric transducers and the corresponding UGW response including reflections and mode conversions. The signal processing techniques presented in Chapter 4 and 5 are employed to identify the modes of interest where the superposed wave modes at certain frequencies (20 to 60 kHz) cannot be directly identified. As a verification, a 3-dimensional Laser Doppler Vibrometer (3D-LDV) scan is performed on the waveguide in order to identify and quantify the wave modes of interest. As a final point, the phenomenon is studied on a pipe in order to investigate its possible effect on the on-site applications of UGWs. The research conducted in this chapter resulted in two publications in *IEEE Sensors Journal and The Journal of British Institute for Non-Destructive Testing (BINDT), Insight* [**SF 02**] and [**SF 05**].

An introduction is given in Section 6.2 including a theoretical background and the recent published literature. Section 6.3 proposes an FEA approach which con-

siders a 3D geometric transducer as the source of UGW excitation which improves agreement between the theoretical predictions and experimental results. A parametric study is undertaken in Section 6.4 which investigates the effect of waveguide diameter on the corresponding UGW response. Experimental validations are carried out in Section 6.5 considering essential parameters such as force and excitation frequencies followed by a verification using a 3D-LDV in Section 6.6. Section 6.7 provides further experimental investigations for pipe applications.

6.2 Introduction

6.2.1 Behaviour of UGW modes

L(0,1) wave mode

L(0,1) is an axisymmetric wave mode that has higher phase velocity compared to its accompanied non-axisymmetric mode, F(1,1). This wave mode is commonly described as an attenuative and dispersive wave mode in pipe applications [**98**], [**47**]. However, in this chapter according to the dispersion curves (*i.e.* Figure 6.5) of the waveguide under investigation (*i.e.* 2.15-m long, *8-mm diameter aluminium rod*) for the operating frequency range of interest (*i.e.* 20 to100 kHz), the group velocity is approximately in the range of [5000:5100 *m/s*]. Therefore, throughout the chapter it is nominally assumed to be non-dispersive as it demonstrates very low dispersion. Figure 6.1 illustrates the fundamental wave modes existing in a short section of the rod under investigation. These are standing waves calculated using a FEA procedure for dispersion curve calculation developed by Sanderson and Smith [**99**]. Figure 6.1–(a) illustrates the three dimensional displacement characteristics (deformation scale factor of 5e-3) of the L(0,1) wave mode at 80 kHz which mainly exhibits axial displacement. It is meshed using structured 8 node linear brick elements with reduced integration.

F(1,1) wave mode

First order flexural wave mode, F(1,1) is a non-axisymmetric wave mode with relatively lower phase velocity compared to the other fundamental existing wave mode in the frequency region of interest, L(0,1) (*i.e.* 20 to100 kHz). Figure 6.1-(b) illustrates the three dimensional displacement characteristics of F(1,1) at 80 kHz which mainly exhibits radial displacement characteristics. It is also shown [**100**], [**101**] that the dispersion properties of first order flexural F(1,1) wave mode

can differ from other wave modes. Unlike the other flexural wave modes, F(1,1) wave mode tend to have an increasing velocity in the frequency range of (up to) 200–kHz. Cui *et al.* [101] highlighted the occurrence of F(1,1) with anomalous dispersion in cylindrical systems and considered possible methods that fall into three categories as experimental, numerical and theoretical methods. They also suggested using LDV and/or 3D-LDV to identify the modes of interest and measure their dispersion.

T(0,1) wave mode

Axisymmetric wave modes are those which have identical displacement vector at all circumferential positions for a given radial and axial position. If the displacement vector of an axisymmetric mode is predominantly circumferential the mode is referred to as 'Torsional'.

The T(0,1) wave mode is the fundamental torsional wave mode (shear type mode) which is non-dispersive in the entire frequency region.
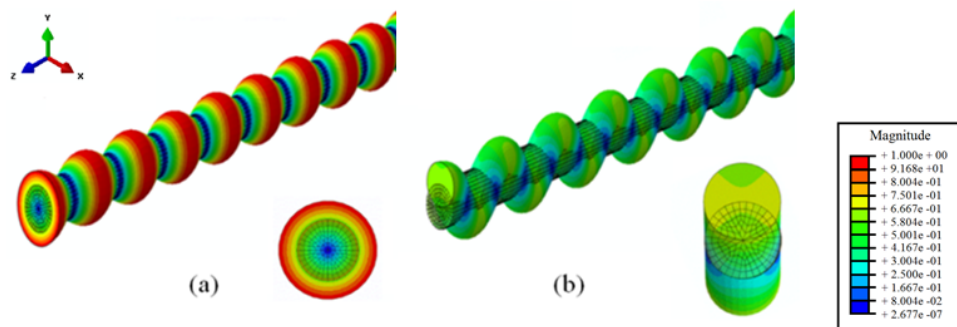

Figure 6.1: Magnitude displacement characteristics of (a) L(0,1) (b) F(1,1) in isometric and cross-sectional view at 80-kHz
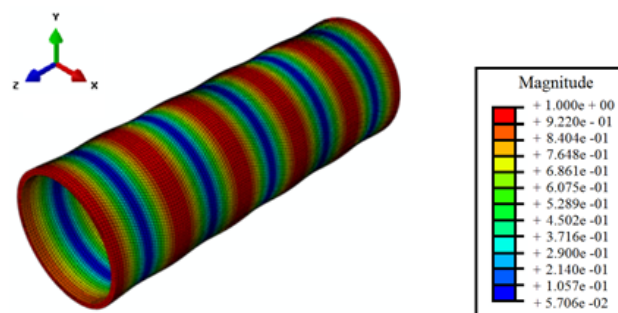

Figure 6.2: Magnitude displacement characteristics of T(0,1) wave mode

T(0,1) is the main wave mode used in field inspections since a single ring of shear mode transducers placed around the pipe circumference (such that they displace the surface circumferentially) is capable of generating the wave mode of interest. The T(0,1) wave mode is used in Section 6.7 in order to pursue the investigations into pipe inspection applications. Figure 6.2 illustrates the standing wave existing in a short section of a schedule 40 pipe (7.11-mm thickness) at 15 kHz obtained using the FEA procedure proposed by Sanderson and Smith [99].

6.2.2   Transducer coupling

Transducer coupling plays an important role in UGW inspections. Conventional ultrasonic liquid couplant is not used when operating shear transducers, as shear wave modes are not supported in Newtonian fluids. Thus, dry coupling with a sufficient amount of force enables the transfer of the displacements into the inspected substrate. The transducer needs to be bound to the surface for a successful coupling [102]. This can be achieved *e.g.* in pipes, by wrapping an inflatable collar around the transducer rings or in rods by using clamps. In commercial UGW systems, the inflatable collars are typically pressurized from 20 psi up to 60 psi in order to exert sufficient pressure on the transducers for them to be adequately coupled to the surface and generate the shear motion in the surface of the waveguide [9]. If the transducers are not sufficiently coupled to the surface, this will induce ringing of the transducers. Due to the lack of damping, the transducer will listen to itself resonating rather than transmitting sound into the component under inspection. This will degrade the resolution of any UGW response and make the signal interpretation challenging or infeasible.

6.2.3   Effect of force on the piezoelectric transducers

Alleyne & Cawley [103] demonstrated the receiving characteristics of a dry coupled transducer. Sixteen circumferentially dry-coupled transducer elements were used to excite UGWs at a single frequency, 70-kHz within a pipe. A clamped transducer listened to the excitation from the coupled element. The peak to peak amplitude of a pulse possessing the velocity of L(0, 2) wave mode in the pipe was measured. It was shown that the magnitude of a received pulse would non-linearly increase with an increase in clamping force. This behaviour can be prescribed from various macroscopic elastic contact theories such as the JKR model [104] and the Greenwood & Williamson model [105] which are fundamentally based upon the *Hertzian*

theory of elastic contact. It is said that the contact area between two elastic bodies is proportionally equivalent to the normal force applied to it by a power of a $\frac{1}{3}$. Engineer [96] studied the effect of the dry force coupling of the Teletest transducer on the received signal, aligning this connection to classical contact theory. It was also shown that as the normal force used to press the transducer on the waveguide increases, the corresponding transmission amplitude increases at a non-linear rate across the frequency spectrum of excitation. However, during these studies the UGWs interacting with the transducer have not been noticed and investigated since the studies mainly focused on the incident and/or the first reflected wave modes rather than the wave modes reverberating between different features of the structure under test. Force dependent coupling of transducers on an 8-mm diameter aluminium rod is investigated in Section 6.5 and further studied in pipe applications in Section 6.6 which have not been covered in the prior literature.

6.2.4 Reflections and mode conversions from discontinuities

Mode conversion, along with waveguide geometric features, can make the signal interpretations challenging. Mode conversion often occurs when a UGW encounters a discontinuity and is converted into a wave mode with different velocity and displacement characteristic. The main focus of the recent research on mode conversion phenomena has been on part circumferential notches, adhesively bonded lap joints and cracks by Alleyne *et al.* [106], Lowe *et al.* [107], Demma *et al.* [108] plates with thickness variations by Cho [109], reflections from free-edge of a structural element by Cho & Rose [110], Morvan *et al.* [111] and Jiangong *et al.* [112]. These studies are mainly focused on the mode conversion of longitudinal and/or torsional wave modes from defects, joints, thickness variations, *etc.* and no attention has been given to the possible reflections and mode conversions from the source of excitation which is the coupled transducer. These reflections and/or mode conversions arising from the coupled transducers may cause misinterpretations. Therefore, the reflections and mode conversions of UGWs from transducers were investigated and studied via FEA, experimentation and 3D Laser Doppler Vibrometry (3D-LDV) measurements. In this study it is shown a considerable amount of reflections and mode conversions can occur due to the presence of the coupled transducers which can potentially become a disruptive matter in practical applications of UGWs. According to the literature, these reflections and mode

conversions from the transducers have not been studied and/or reported in the field of guided waves.

6.3   Proposed FEA approaches

Currently, the modelling of UGW propagation is performed using selected nodes in the geometry which simulates a 'point excitation' [99], [114], [119]. In laboratory experiments, UGW excitations are applied using transducers which have different acoustic impedance and material properties in comparison to the waveguide. However, the nodes in FEA have the same acoustic impedance and material properties. Here, a FE model is presented which was developed concurrently by S. Lowe and published in [SF 05]. It considers the 3D geometry of the transducer as the source of excitation rather than using the nodes (point excitation) which is commonly used by researchers in the field. The FEA of an aluminium rod (8-mm diameter, 2.15-m long) was performed using the commercially available FE software, ABAQUS *version 6.12*. The model is a three dimensional (3D) simulation of UGWs propagating within a solid body using linear brick elements. The excitation frequency in all models was chosen to be 80-kHz since, according to the dispersion curve given in Figure 6.5, the individual wave modes are expected to arrive at separate ToAs. Therefore, they could be directly identified. The results are further investigated through a FEA parametric study in Section 6.4 and validated through experimentation in Section 6.5.

The dispersion curves for the rod are calculated using Disperse. At the excitation frequency used, there are only three possible modes, L(0,1), T(0,1) & F(1,1). The excitation direction is along the axis of the rod. This would preferentially excite L(0,1) & F(1,1). Therefore the presence of T(0,1) could be ignored due to the alignment of the piezoelectric element.

Two separate FE-models were used to study the mode conversions caused by UGWs interacting with the transducers as outlined below.

6.3.1   FEA Model 1

The first model uses a single point/node to excite an 80-kHz, 10-cycle Hann-windowed pulse within an 8-mm diameter aluminium rod, as illustrated in Figure 6.3-(a). The node of excitation has been placed on the free-edge of the rod. The properties assumed for the FE-model are given in Table 6.1.

6.3.2 FEA Model 2

The same pulse as that described in *FE-model-1* was excited along a line between a 3D geometric modeled, shear transducer and the rod at the free edge. The transducer was connected to the rod using the '*tie*' constraint function[21]. Therefore, it was assumed that the transducer was bonded to rod. The material properties used in the model are provided in Table 6.1.

Figure 6.3 (b) and (c) display the *FE-model-2* in 3D dimensions. The transducer [115] is made up of a piezoelectric element and a steel backing block. In both FE models the dimensions of the elements were in the range of 1.21 - 1.27-mm. This type of mesh refinement was used to ensure there were at least eight elements to adequately represent the smallest wave length of interest [106].

Figure 6.4[22] shows the UGW response generated from the two FE-models. As illustrated, the ToAs of each echo from the far free-edge of the rod are matched in both responses. However, the second response has additional signals as labelled in Figure 6.4-(b). The signals have been identified and labelled according to the calculated ToAs based on the dispersion curve in Figure 6.5 at 80-kHz frequency. The first wave mode to arrive is the L(0,1) wave mode reflected from the free-edge of the rod as it is the fastest wave mode followed by the second wave mode, F(1,1) with multiple succesive echoes.

According to Figure 6.4–(b), after the first F(1,1) echo and second L(0,1) echo, there is an unexpected wave-packet present in the UGW response. ToA of this wave-packet is consistent with a mode conversion from F(1,1) to L(0,1) and/or L(0,1) to F(1,1) occuring at the transducer location with the amplitude of 22.9 dB and 14.7 below the L(0,1) and F(1,1) respectively. It is notable that the mode converted signal contributes to the coherent noise[23] therefore the aforementioned dB values for L(0,1) and F(1,1) are interpreted as Signal to Coherent Noise Ratio

---

[21]From ABAQUS version 6.12 manual: 'tie' constraint function enables the coupling functionality of separate geometries and considers the geometries to act as a part of the body of the other geometries.

[22]In the modelling and experimental results, the excitation signal and the cross talk/switch on spike appearing at time zero were ignored.

[23]In the field of guided waves, '*coherent noise*' is the disturbance generated due to the presence of numerous possible wave modes which can degrade the resolution of the guided wave response. The coherent noise has two main sources: a) The excitation and reception of unwanted modes, b) The transmission of UGWs and reception of multiple echoes from unwanted directions.

(SCNR)[24]. The ToA of the individual wave modes for the two FEA models are available in Table 6.2. In this particular setup, mode conversions occur from a number of different modes propagating in the rod and interacting with the transducer. For this reason it is necessary to have a convenient shorthand system for designating a particular reflected and converted wave modes [21]. The notation adopted for this chapter is the following:

- L(0,1) - pure first order longitudinal wave mode

- F(1,1) - pure first order flexural wave mode

- L(0,q) - converted longitudinal mode from F(1,1), q≥1

- F(β,q) - converted flexural mode from L(0,1), $\beta \geq 1$

This mode converted wave-packet represented is the superposition of F(β,q) & L(0,q) at the same ToA since their round trip time would be identical while they are interchangeably converted. This has been calculated in which F(β,q) & L(0,q) possess the exact equivalent ToAs as:

$$ToA_{L(0,q)} = ToA_{F(\beta,q)} = 2(t_{L(0,1)} + t_{F(1,1)}) \tag{6.1}$$

where, $t_{L(0,1)}$ & $t_{F(1,1)}$ are the time duration for L(0,1) & F(1,1) respectively to propagate from one free-edge of the rod to the other. The time durations are calculated based on,

$$t = x/v_{gr} \tag{6.2}$$

where, x is the propagation distance of the wave mode of interest and v_{gr} is the group velocity value given by the dispersion curve (Figure 6.5). An Additional pictorial representation of the aforementioned description to yield (6.1) is provided in Appendix C.

Therefore, these two mode converted wave-packets are combined to build another wave-packet with relatively higher amplitude with respect to each one of them

---

[24]In order to avoid any possible confusion in the terminology of Signal to Noise Ratio (SNR) used in Chapter 4 and Chapter 5, Signal to Coherent Noise Ratio (SCNR) was introduced to be used throughout the chapter. SCNR represents the ratio between the peak amplitude of the dominant wave mode (incident wave mode or a response from a %100 reflector) to the peak amplitude of the wave modes of interest. The peak value of the wave modes were calculated using: $Peak\ value = (max(dataset) - min(dataset))/2$. The normalizations of the Y-axes in the figures presented throughout the chapter is against the aforementioned peak value.

individually. The individual mode converted wave-packets are extracted by 3D-LDV (Figure 6.16) and compared with the results given by the transient FEA model (Figure 6.17) in Section 6.6.

However, the presence of the mode converted signal was only predicted by *FE-model-2*. In laboratory experiments UGW excitations are applied using transducers which have different acoustic impedance and material properties to the waveguide, however; the nodes in FEA have the same acoustic impedance and material properties. This fact was only considered in *FE-model-2* which produced a discrepancy of results between the two models.

6.4   Parametric study of the FEA

A parametric study was undertaken through FE-transient modelling in order to observe the behaviour of UGWs interacting with the transducers on different diameters which is the most commonly changed parameter in UGW inspections. Therefore the ratios between the reflected and mode converted signal in relation to the waveguide diameter could be measured for both models (*FE-model-1* and *2*). The dispersion curve of the rod with different diameter is illustrated in Figure 6.5. It is notable that the velocity of L(0,1) is inversely proportional to the change in the diameter. However; as the diameter of the rod expands, the velocity of F(1,1) increases.

Figure 6.6 represents the UGW responses of a rod with 8-mm to 14-mm diameter. The response for the 8-mm diameter is chosen as the baseline. The dashed blue & red lines respectively represent the expected and unexpected wave modes appearing at the baseline. The dashed lines help to illustrate the movements of the wave modes of interest in time as the diameter of the rod increases. It can be seen that the responses given by single point/node excitation and 3D-transducer excitation do not correlate, since the transducer functionality was disregarded in the *FE-model-1*. The mode conversion phenomenon is evident in all the responses where the diameter of the rod varies from 8 mm to 14 mm.

It is also evident that the wave modes arrive at different ToAs due to the change in their velocity after the corresponding changes in the diameter. This causes the L(0,1) & F(1,1) wave modes to be superposed at some echoes as shown in Figure 6.6–(c) & (d). Figure 6.7 represents the peak amplitude proportion of first reflected wave modes with an increase in the rod diameter for *FE-model-1 & 2*. Although the ToAs of fundamental wave modes are matched in both models, the amplitude

of the two models do not correlate.

The peak amplitudes of the reflected and mode converted signals off the transducers are normalized and given in Figure 6.7 with quantified SCNR values for the wave modes of interest. As can be observed, in both models, the amplitude of L(0,1) decreases as the rod diameter expands. Therefore, as the diameter of the rod increases the less effective a single transducer or a node/single point becomes at generating axisymmetric wave modes. In *FE-model-2*, the amplitude of F(1,1) increases as the rod diameter expands. When the size of the UGW transmitter is very much smaller than the wavelength of the transmitted signal, it could be considered as a point source. According to the alignment of the excitation, it would be expected that all possible modes over the frequency bandwidth of the excitation signal would be generated *i.e.* L(0,1) & F(1,1). Using a node/point excitation (*FE-model-1*) will emphasize more on a non-axisymmetric excitation *i.e.* F(1,1) and less on an axisymmetric excitation *i.e.* L(0,1). When a 3D-geometric piezoelectric transducer is used (*FE-model-2*) for excitation along the axis of the rod, this helps longitudinal modes *i.e.* L(0,1) to be generated with higher proportion. However; as the rod diameter expands, the amplitude of non-axisymmetric wave modes *i.e.* F(1,1) will have higher contributions to the UGW response and consequently possess higher SCNR due the excitability (frequency-thickness product) of the wave mode of interest on the waveguide [13], [116].

Properties	Aluminium rod	Transducer element	Backing Block
Density	2700 kg/m^3	7600 kg/m^3	7830 kg/m^3
Young's Modulus	70 GPa	76 GPa	207 GPa
Poisson's Ratio	0.33	0.31	0.3

Table 6.1: Assumed material properties for the FEA models

		FE-model-1	FE-model-2
Mode Type	v_{gr}(m/s)	ToA (μs)	ToA (μs)
L(0,1)	5100	848	848
F(1,1)	2900	1380	1380
Mode converted	N/A	N/A	2270

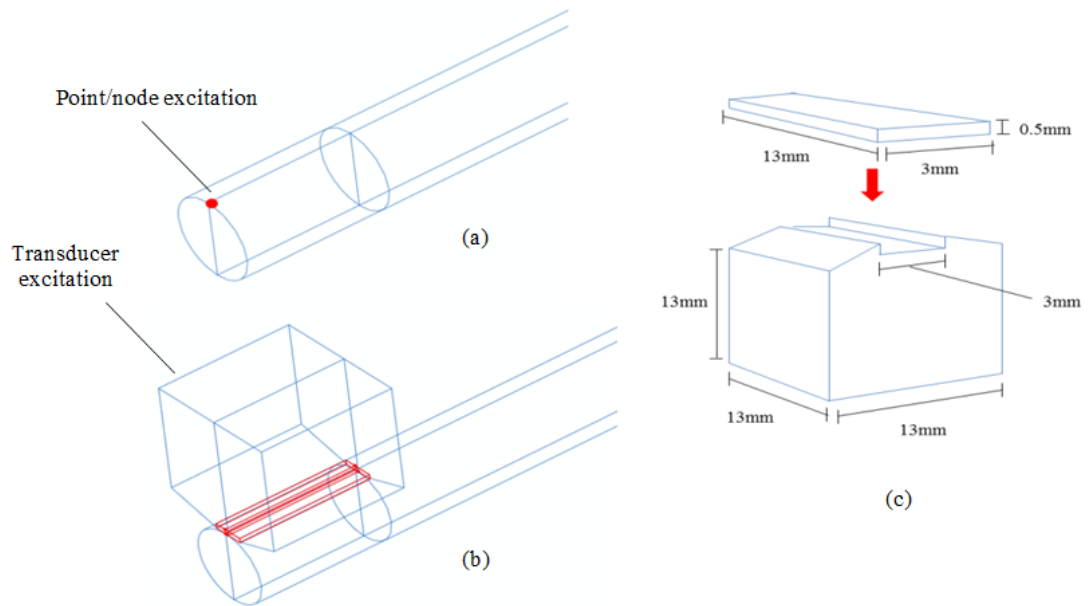Table 6.2: Wave mode information for FEA model 1 and 2

Figure 6.3: Layout of the FE model: (a) short section of the aluminium rod with point excitation and (b) transducer excitation, (c) modelled transducer with accurate dimensions
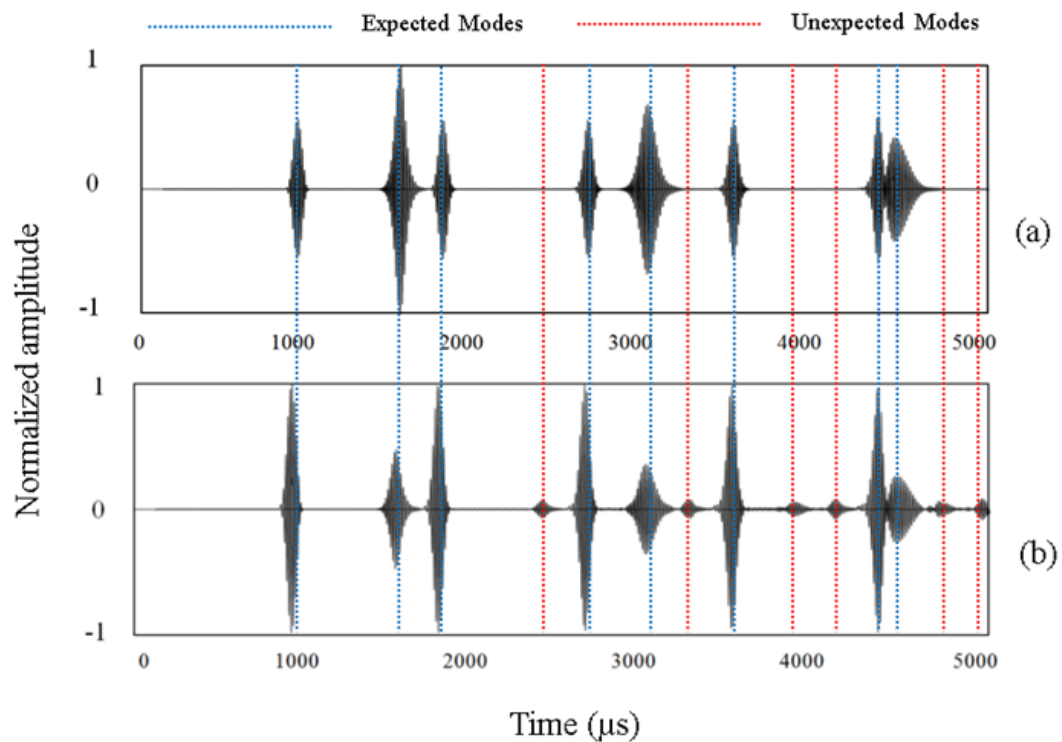

Figure 6.4: UGW response given by (a) FEA model 1 and (b) FEA model 2: Blue dotted lines represent the expected wave mode (L(0,1) & F(1,1)) and the red dotted lines represent the unexpected mode converted signal.
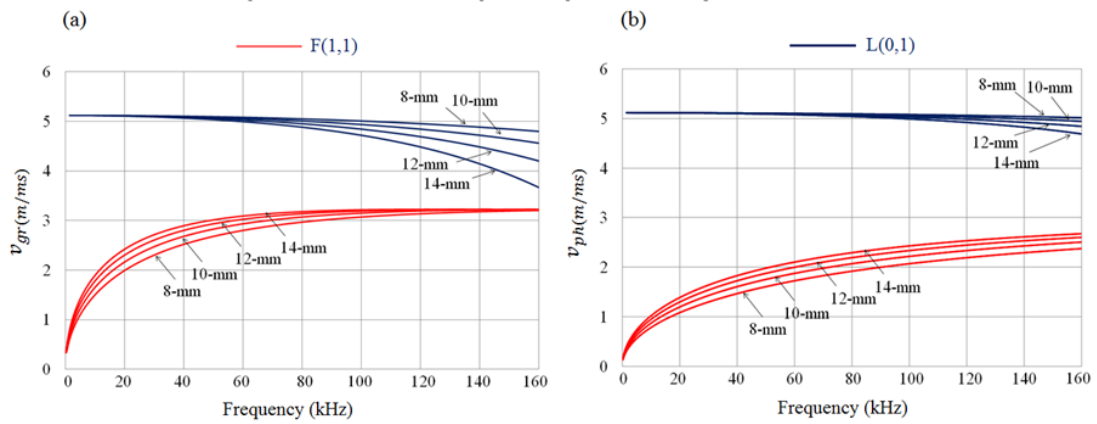
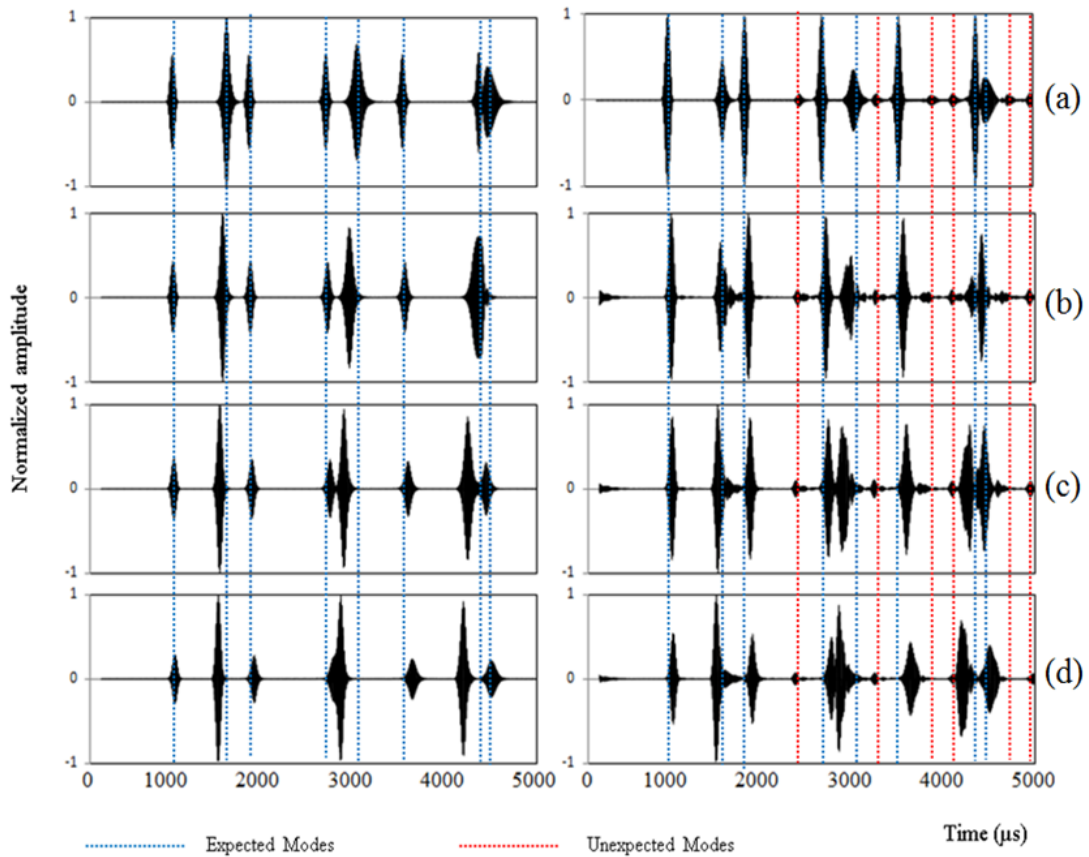Figure 6.5: Dispersion curve: (a) Group velocity (b) Phase Velocity for different diameter aluminium rods

Figure 6.6: Parametric study results, UGW response of (left) FEA model 1 and (right) FEA model 2 for (a) 8-mm, (b) 10-mm, (c) 12-mm and (d) 14-mm diameter rod: Blue dotted lines represent the expected wave modes (L(0,1) & F(1,1)) and the red dotted lines represent the unexpected mode converted signals.
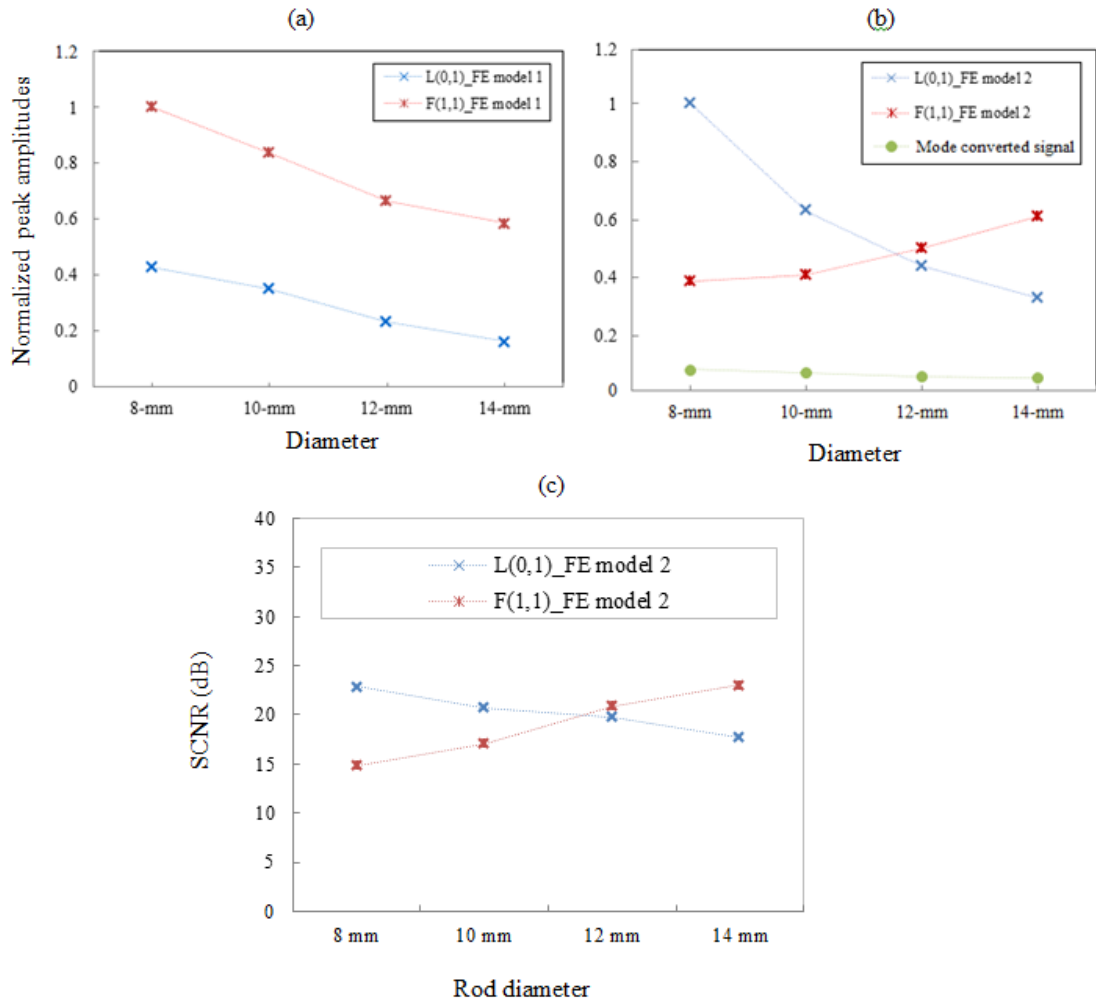
Figure 6.7: Peak amplitude proportions for individual wave modes (a) FEA model 1 and (b) FEA model 2, normalized against the maximum value and (b) SCNR values for the fundamental wave mode when compared with the mode converted signal in FE model 2.

6.5 Laboratory experiments

The experimental setup is illustrated in Figure 6.8. An 8-mm diameter, aluminium rod with the length of 2.15-m has been used for the experimental validation. According to the parametric study; the signals could be clearly identified in the selected waveguide since there was no interaction predicted between the individual reflections. The rod was placed on two wooden blocks and supported with foams to avoid any possible reflection from the surroundings. The piezoelectric transducer shown in Figure 6.8 is coupled axially to the rod in a manner that allows it to actuate longitudinally. To validate the FE-models, a 80-kHz 10-cycle Han win-

dowed pulse was excited using a UGW unit [9]. The UGW response is displayed in Figure 6.9. The experimental result shown in Figure 6.9 correlates with the result obtained from the 8-mm diameter aluminium rod (in terms of identified UGW responses) in the parametric study, Figure 6.6–(a) which uses a 3D geometry of the transducer for excitation. The mode converted signal is 7 dB below the L(0,1) wave mode and 4.5 dB below the F(1,1) wave mode. As was discussed in Section 6.3 and 6.4, this is due to the UGW interaction with the transducer which induces the mode conversion. The experimental result is summarized and compared with *FE-model-1* and *2* in Table 6.3. It is also noted that there was no mode conversion observed from the far flat free-edge of the rod where no feature was coupled to its surface.
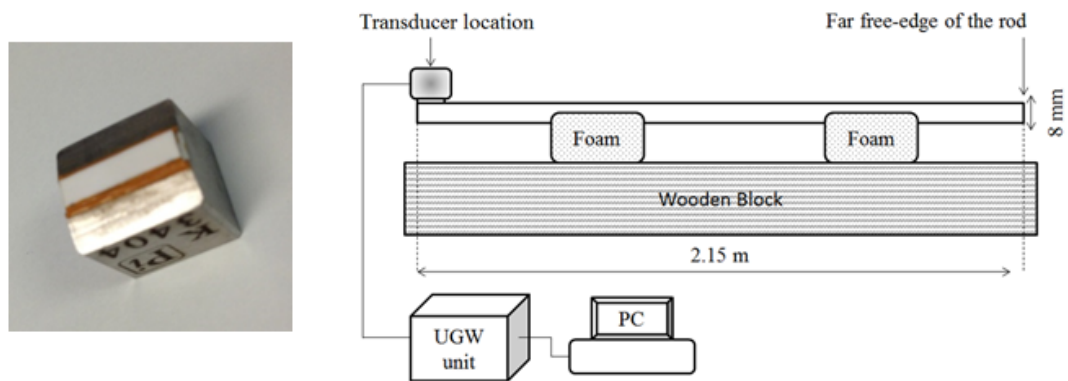

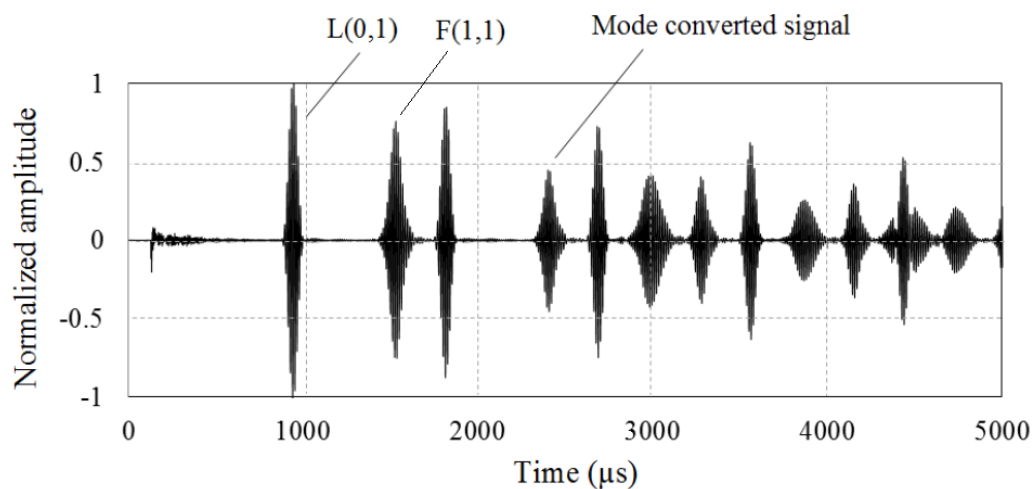Figure 6.8: (left) Shear type Teletest piezoelectric transducer and (right) Experimental setup

Figure 6.9: UGW response of the experiment

Mode Type	v_{gr} (m/s)	FE-model-1 ToA (μs)	FE-model-2 ToA (μs)	Experiment ToA (μs)
L(0,1)	5100	848	848	870
F(1,1)	2900	1380	1380	1400
Mode converted	N/A	N/A	2270	2350

Table 6.3: Wave mode information for FEA models and experimental results

6.5.1 Frequency dependency of coupling dependent mode conversion

A pulse-echo frequency sweep excitation has been performed (based on the same setup described in Figure 6.8) in order to investigate the UGW reflections and mode conversions from the transducer in the range of frequencies commonly used in commercial inspection systems *i.e.* 20 kHz to 100 kHz. The signals in the UGW responses for the range of 20 to 60 kHz are heavily superposed and could not be directly identified. Beyond 60 kHz (*i.e.* 60 to 100 kHz), the wave modes tend to arrive at separate ToAs therefore could be directly identified as illustrated in Figure 6.10. The peak amplitude of the individual wave modes are therefore extracted and displayed against each operating frequency in Figure 6.11 with quantified SCNR values for the wave modes of interest. It can be observed that the amplitude of the individual wave modes are decreasing since the attenuation rate and frequency are directly related. The amplitude of F(1,1) wave mode also decreased more rapidly compared to the L(0,1) wave mode due to its dispersive nature. This trace for F(1,1) wave mode had a direct effect on the magnitude of the mode converted signal which is produced by the superposition of both flexural and longitudinal wave modes. Moreover, the drop in the amplitude of the mode converted signal caused an increase in the SCNR of the wave modes of interest (L(0,1) and F(1,1)) at higher frequencies. The presences of the mode converted signal have been identified with the aid of the signal processing techniques developed in previous chapters (FSE in Chapter 4 and IDC in Chapter 5) where the signals at 20 to 60 kHz were

superposed. The results are available in the *Appendix B*. Hence, it is diplayed that for each operational frequency that has been excited, the mode conversion behaviour which is instigated by wave mode reflections off the transducer is present at every frequency.
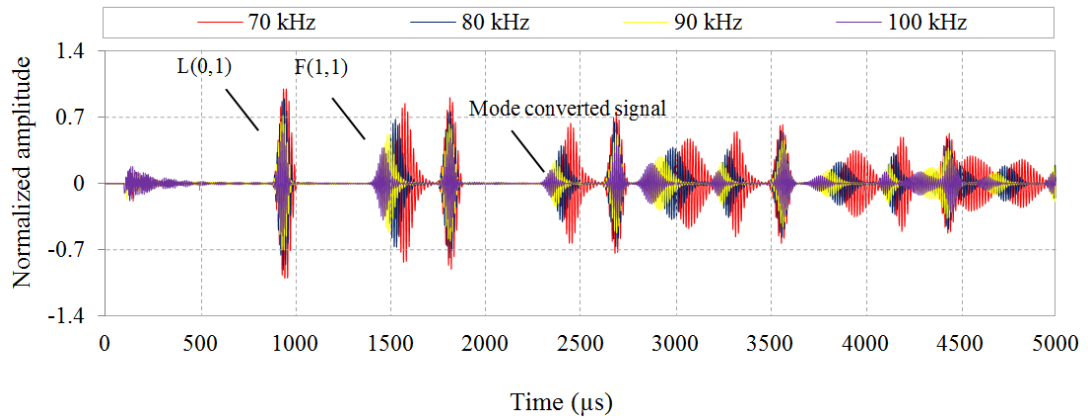

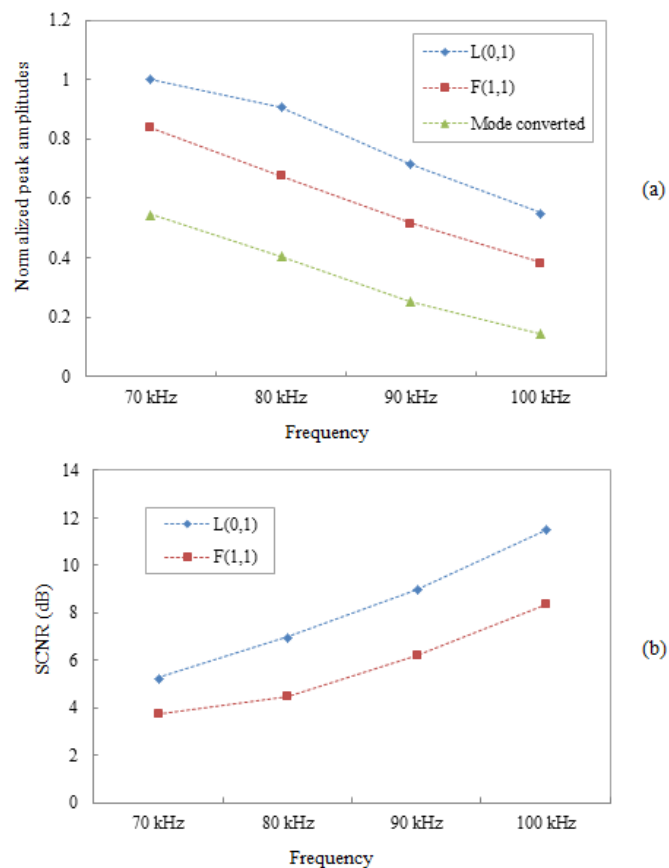Figure 6.10: Frequency sweep response from (a) 20 to 60 kHz, (b) from 70 to 100-kHz

Figure 6.11: (a) Amplitude proportions for individual wave modes at each operating frequency, normalized against the maximum value (b) SCNR of the individual wave modes

6.5.2 Force based coupling dependent reflection and mode conversion

UGW transducers are commonly dry-coupled using *e.g.* clamps [**60**], [**117**], springs [**118**], [**119**], pneumatic collars/air pressure to supply a normal loading force. The applied force can affect the amplitude of the UGW response [**103**]. Therefore, an investigation was conducted to study the effect of a varying physical force applied on a single shear transducer and the subsequent UGW response while transmitting through an aluminium rod and reflecting from its free-edge. A pulse-echo excitations have been made with an incrementally increase in force in order to observe the relationship between the force and the peak amplitude of the first reflected signals from the free-edge of the rod and the mode converted signal from the transducer.

Experimental Setup

The test rig [**96**] which is displayed in Figure 6.12 is designed to mount transducers and accommodate long lengths of waveguides. The purpose of the rig is to apply a normal force onto the transducer. The force applied can be controlled and varied. The premise of the rig is based on a simply supported beam subjected to a point force. A pneumatically driven ram is used to apply a force. The ram is bolted onto an aluminium truss. It contains an extended shaft that houses the transducer and accurately positions the transducer repeatedly. The force applied is varied by an air pressure regulator with a gauge indicating the pressure supplied to the ram. A toggle switch has been implemented to actuate and retract the ram in order to safely mount and dismount the transducer. Neglecting the self-weight of the beam, any force applied on the waveguide will create an equal but opposite reaction force at the location of contact. This principle was used to measure the force being exerted on the transducer by the pneumatic ram. A load cell sensitive to compression forces is placed directly underneath the waveguide at the location where the transducer is impacting with the waveguide. With the waveguide sitting on the load cell, a reaction force reading can be taken when an external force is applied to the waveguide.

Pulse-echo excitation with incremental applied forces

Incremental forces were exerted on to the transducer whilst transmitting a pulse at 80-kHz. At this frequency, an UGW response with sufficient wave mode separation

is produced according to given velocities and corresponding ToAs given in Table 6.3. The transmitter is coupled to the free-edge of the rod and the force applied on the transducer is then subsequently adjusted from 5 to 205-N with 10-N increments. Data collection is taken for the specified frequency range for each load cell reading. Two sample pulse-echo UGW responses at 5 and 55-N applied forces are displayed in Figure 6.13 which represents multiple echoes from the far free-edge of the rod. It can be observed in Figure 6.13–(bottom) that a wave-packet arises at $\approx$2400-μs after the first echo of F(1,1) wave mode which is the result of mode conversion from the coupled transducer. It is notable that the mode converted signal contributes to the coherent noise [120] at a low force (*i.e.* 5 N). In this case due to the low level of force applied to the transducer, the coupling will be affected and the UGW response experiences a relatively long ringing phenomenon as can be seen in Figure 6.13–(top). The amplitude of the mode converted signal is considerable *i.e.* SCNR $\approx$ 17.1 dB below the first reflected L(0,1) & 15.2 dB below the first reflected F(1,1) at 55 N applied force. Therefore, above the threshold of a clamping force (*i.e.* 5 N) the coupled transducer effectively acts as a non-axisymmetric feature on the waveguide.

The overall results of the peak amplitude for the first reflected L(0,1), F(1,1) and mode converted signals, are plotted against the incremental rise in clamping force in Figure 6.14 with quantified SCNR values for the wave modes of interest. It is illustrated that the amplitude of the mode converted signal, non-linearly increases with incremental forces as well as the fundamental longitudinal and flexural wave modes. The figure shows that the amplitudes of the wave modes of interest are in proportion. This behaviour can be prescribed from various macroscopic elastic contact theories which are fundamentally based upon the *Hertzian theory of elastic contact*. It is said that the contact area between two elastic bodies is proportionally equivalent to the normal force applied to it by a power of a $\frac{1}{3}$ [96], [104]. The test was repeated five times and the standard error of the responses were calculated to be less than %10. The average values for the SCNR of L(0,1) and F(1,1) shown in Figure 6.14-(b) are calculated to be 19.02 and 17.08 respectively.
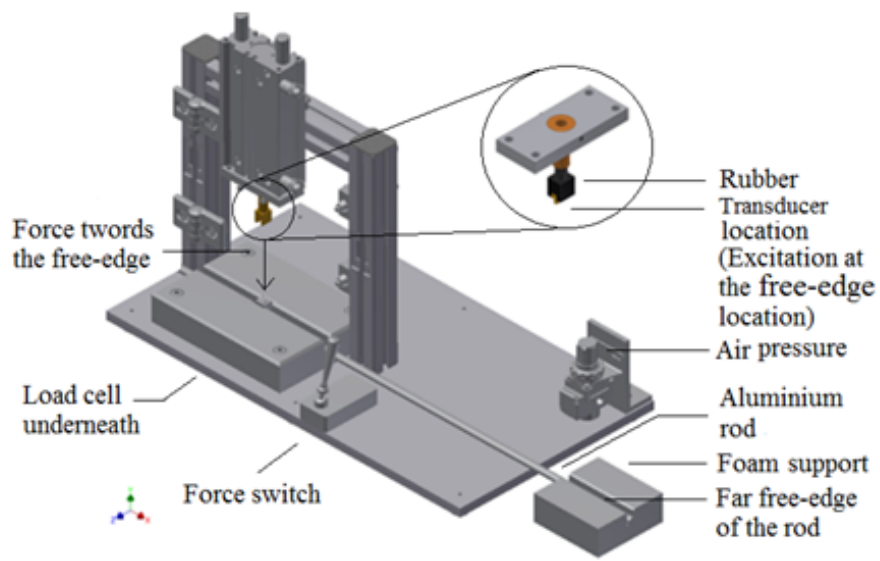
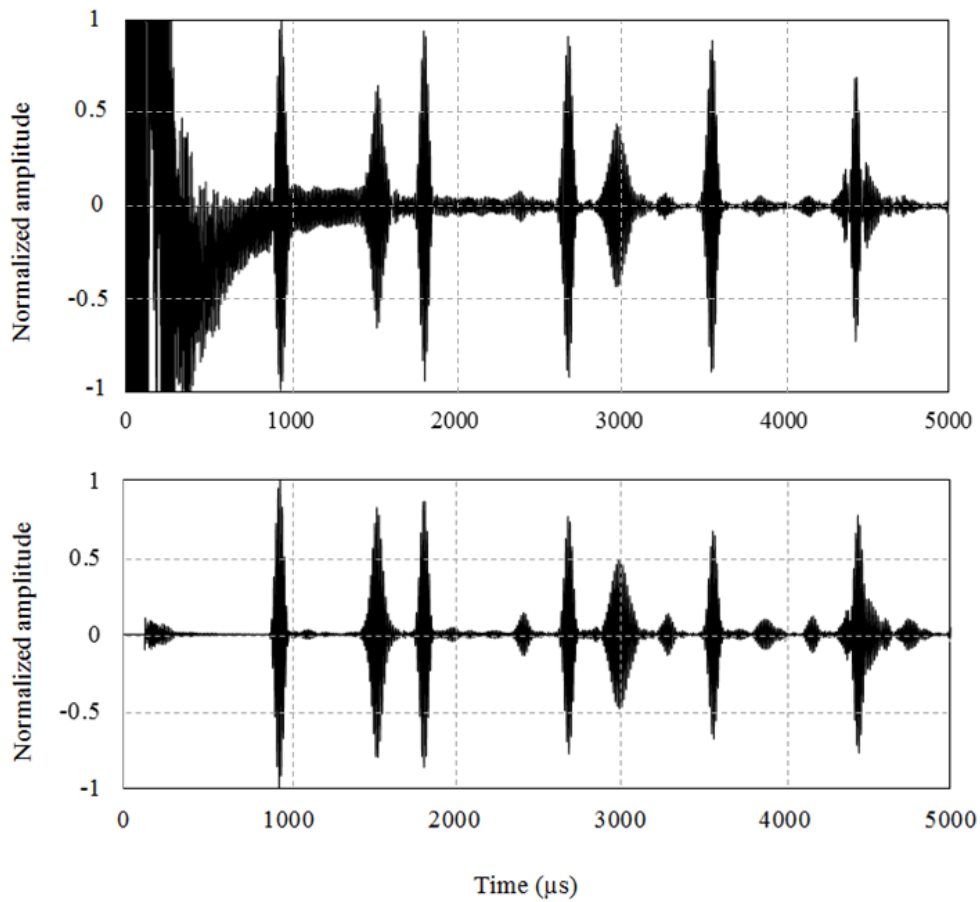Figure 6.12: The test rig used to mount the transducer with a measurable applied force

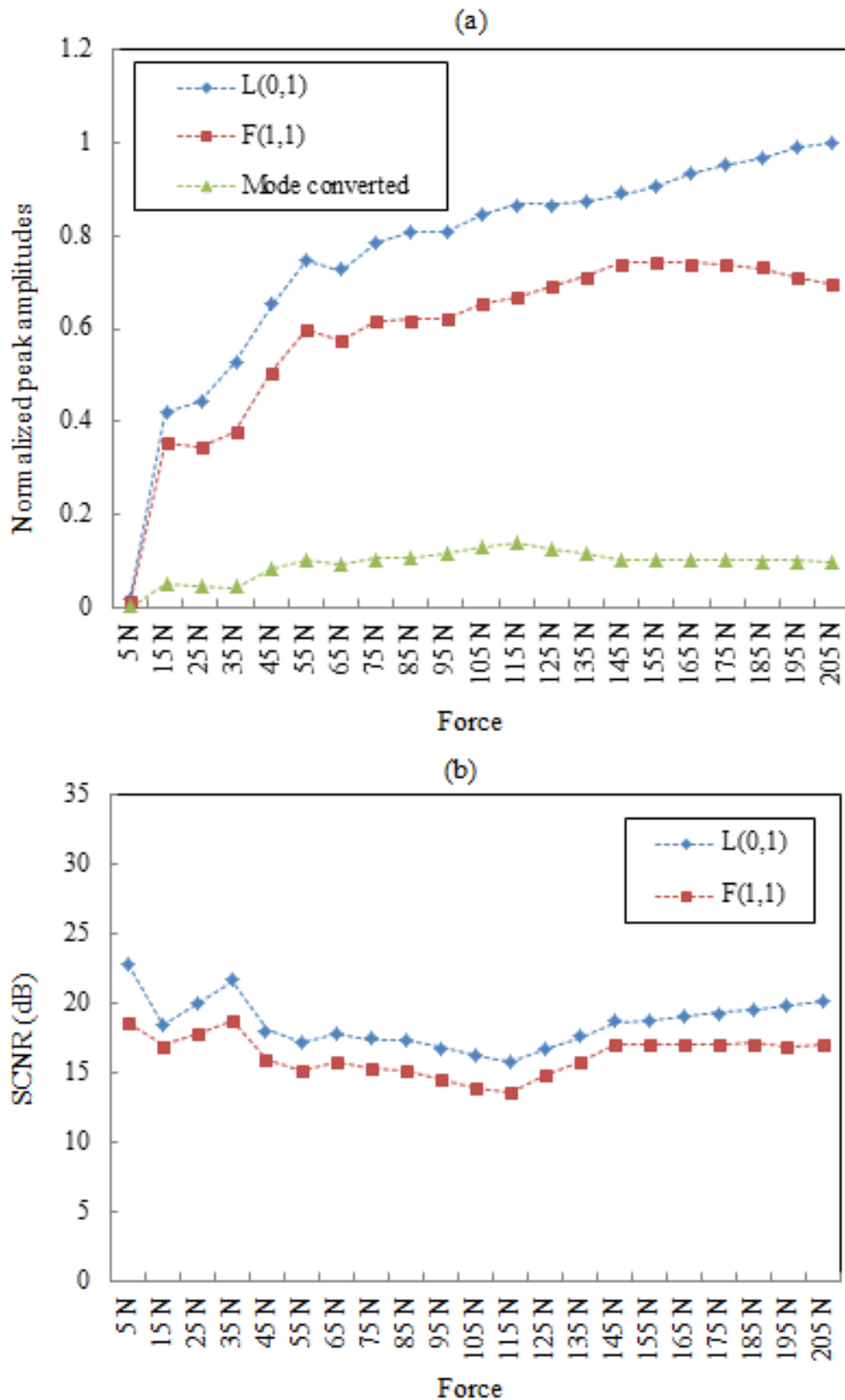Figure 6.13: Sample UGW response at (Top) 5-N and (bottom) 55-N applied force

Figure 6.14: (a) Force vs. peak amplitude of a pulse-echo excitation at 80 kHz, normalized against the maximum value (b) calculated SCNR values for L(0,1) and F(1,1) wave modes

6.6 3D LDV verification

According to the test-setup used in Section 6.5, the mode converted signals *i.e.* L(0,q) & F(β,q) were superposed at the transducer location (shown in Figure 6.9) in which the consequent wave-packet was labelled as mode converted signal. Laser vibrometry was used to unintrusively measure the vibration of the surface of a spatial position such that the wave modes of interest L(0,q) & F(β,q) were separated in time domain. The optical receiver can potentially eliminate the uncertainty of the coupling and receiving transfer function of the piezoelectric ceramic so the existence of wave modes generated purely by transmission could be validated. The 3D-LDV is equipped with three laser sensor heads in order to detect the 3D motions caused by UGW propagation through the structure. The motions of the surface are caused by excitation of 5-cycle UGW signals at 80 kHz via shear transducer. The laser can detect the surface velocity and derive displacement changes as waves propagate through the structure with a continuous analog voltage output that is proportional to the target velocity component along the direction of the laser beam [121].

In order to capture the full wave forms of the wave modes from the vibrometry results, 0.36m of the rod was scanned based on (6.3). Although a 10-cycle Hann windowed sine wave was used in the FE model in the experimental validation (Section 6.3 & 6.5), the excitation of 5-cycles was alternatively performed in the vibrometry experiment due to the limitation of the beam angle of the laser heads [121], [122]. Given the velocity and excitation frequency of the existing wave modes, the longest possible pulse-length (L) could be calculated as,

$$L = n\lambda \tag{6.3}$$

where, n is the number of cycles and λ is the wavelength of the wave mode of interest which can be expressed as,

$$\lambda = v_{gr\_max}/f \tag{6.4}$$

where, v_{gr_max} is the maximum group velocity value of the existing wave modes across the operating frequency range. Therefore, the sufficient length of line scan could be chosen as a value equal or more than L.

Scan setup

The same aforementioned pulse-echo excitation setup illustrated in Figure 6.8 has been used during the vibrometry scan, taking into account that a *dividing head* was used to rotate the waveguide eight times with 45° intervals. Therefore, eight 3D-line scans with 120 points have been conducted covering 0.36 m of the rod at each individual degree as illustrated in Figure 6.15. According to the dispersion curve given in Figure 6.5, the L(0,q) & F(β,q) could be potentially separated along the line scan, 0.55-m away from the excitation point since the 3D-LDV can act as a non-contact UGW receiver. Foams were used beneath the rod and inside the dividing head in order to prevent the *dividing head* from causing any additional feature to the waveguide's surface.

Scan Results and further discussion

Figure 6.16 represents the surface velocity of the waveguide at a fixed point in time (in isometric and cross-sectional view) caused by various UGW modes. It provides normalized measurements (against the maximum value) of surface velocity (absolute value) of the waveguide at the points where the lasers are pointed. A measurement of this kind provides a signal that represents the material's velocity at the surface of the waveguide as recorded over time. Since the velocity is the rate of displacement, it is possible to use either when measuring the characteristics of the wave modes. Note that the surface velocity does not represent the propagating velocity of the wave modes. The polar plots represent the cross sectional view of the measured axial, circumferential and radial displacement respectively for each mode. Four wave modes *i.e.* L(0,1), F(1,1), L(0,q) & F(β,q) are displayed in
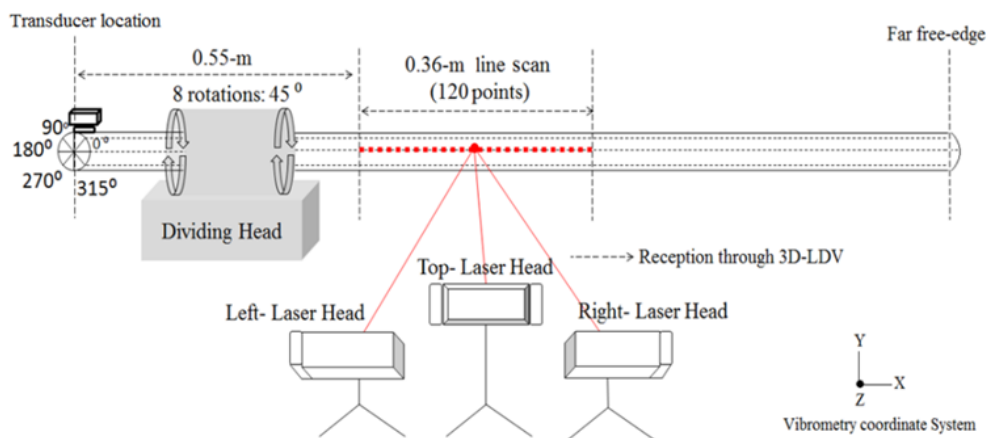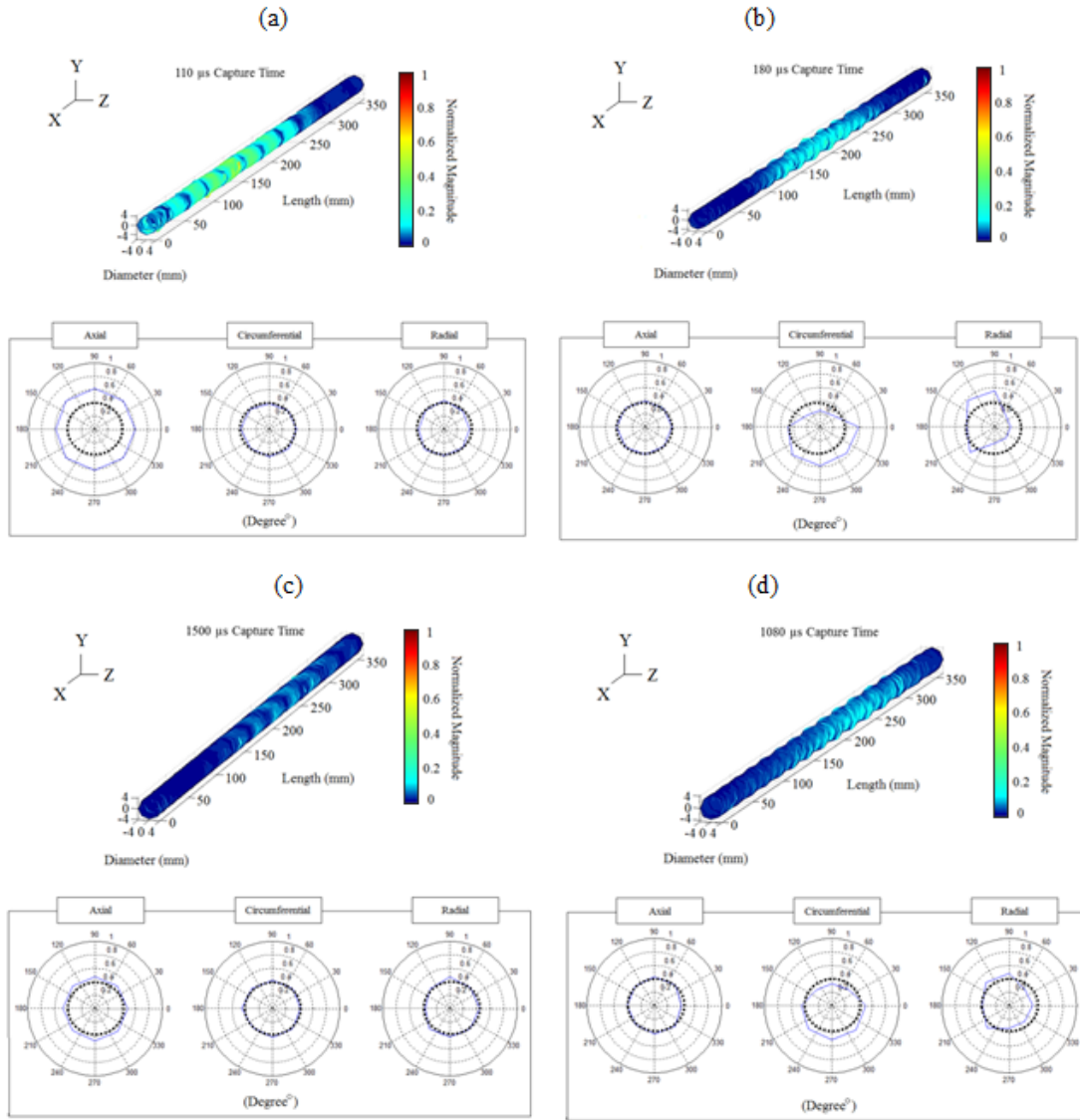

Figure 6.15: 3D-LDV setup

Figure 6.16: 3D-vibrometry captured wave modes at: (a) 115-μs: L(0,1), (b) 180-μs: F(1,1), (c) 1500-μs: L(0,q) and (d) 1080-μs: F(β,q). The black dotted lines are theatrical lines representing the cross section of the rod under investigation.

Figure 6.16 and identified according to their displacement characteristics (using Figure 6.1), measure of dispersion (using Figure 6.5), expected ToAs (using (6.2)) and estimated pulse length (using (6.3)).

Figure 6.17 illustrates the wave modes of interest captured at different time steps given by the transient FEA model which agrees with the results given by 3D-LDV. Thus, the wave modes present in the waveguide which were identified by the 3D-LDV correlated with the reflected and converted modes identified throughout the modeling and experimentation.

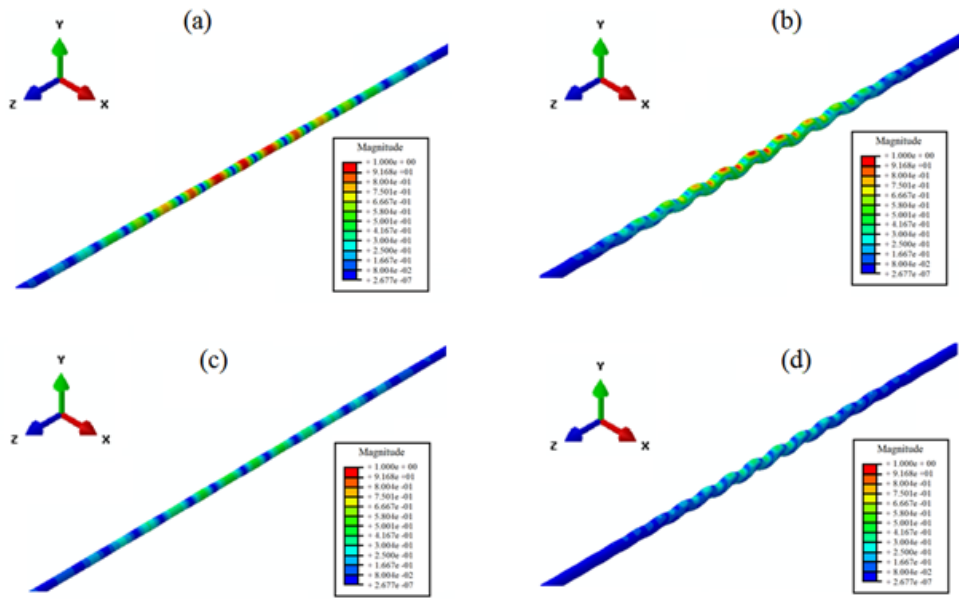It was also validated that the modes known as L(0,q) & F(β,q) will be added

Figure 6.17: FEA predicted propagating wave modes at: (a) 140-μs: L(0,1), (b) 210-μs F(1,1), (c) 1200-μs L(0,q) and (d) 1050-μs F(β,q)

to the UGW response due to mode conversion as was also predicted in (6.2). A mode converted signal generated by a transmitter emulating a waveguide feature is influenced by two main governing factors. Primarily, the amplitude of an original mode directly affects the presence of a mode converted signal from a feature as it is a derivative from the initial incident wave.

The second factor is that the occurrence of mode conversion is dependent on the ability of a transducer to act as a non-axisymmetric feature on a structure. This phenomenon can make the signal interpretation challenging as in some applications it has the potential to be misread as a defect in a structure while the structure is in fact defect free. In addition, the phenomenon can be misinterpreted with some higher order modes existing in the operating frequency region especially in some applications where the cut-off frequency of the higher order longitudinal/flexural modes are relatively low, *e.g.* 68-kHz for an 64-mm diameter aluminium rod.

6.7 Further studies on pipe applications

After the investigation of the interaction of UGWs with piezoelectric transducers on an aluminium rod, the subject has brought the attention to the practical implication of the phenomenon in industrial pipelines. Here, the interaction of UGWs with piezoelectric transducers is studied on a pipe which has not been highlighted

in the prior literature. Laboratory experiments are carried out to measure the effect of operating frequency and the force on the dry-coupled piezoelectric trans- ducers and the corresponding UGW response. Figure 6.18 illustrates the phase and group velocity dispersion curve of T(0,1) wave mode and its family of flexural wave modes for a 6 inch schedule 40 pipe (7.11-mm wall thickness). In this chap- ter T(0,1) wave mode is employed in order to generate UGW through a schedule 40 6-inch (7.11-mm thickness) pipe and quantify the UGWs interacting with the transducer rings coupled to the pipe surface. As a result of the quantification of those UGWs interacting with the transducer rings, useful recommendations are given for on-site applications.

6.7.1 Experimental setup

Pulse-echo single ring torsional excitation 0.75-m away from the near end of the pipe

The experimental setup used throughout the chapter is illustrated in Figure 6.19. A ring of 24 evenly spaced transducers (Figure 6.20) is coupled to a 6-inch schedule-40 carbon steel pipe, 0.75-m away from the near end. The distance from the edge was set to achieve optimum UGW response with sufficient wave mode separation in time domain according to the dispersion curve given in Figure 6.18. The purpose of this setup is to perform a bi-directional UGW excitation so that the peak amplitude of the incident wave mode and the scattered signals (reflected and/or mode converted) off the transducers could be directly measured.

The transducer ring shown in Figure 6.20 was manufactured as a custom prototype to achieve an evenly spaced distribution of the transducers around the circumfer- ence. Commercially available Teletest tool can be found in Figure 6.26. Similarly the Teletest collar is able to distribute 24 transducers circumferentially around the pipe however, as can be seen, the spatial distribution is non-axisymmetric. The Teletest tool was used in the experimental setup employed to quantify the effect of multiple rings on the UGW response.

6.7.2 Effect of force on the UGW response

Based on the aforementioned experimental setup, the pulse-echo excitation was conducted 0.75 m away from the near end of the rod at 50 kHz in order to measure the peak amplitude of reflected and mode converted signals off the axisymmetric
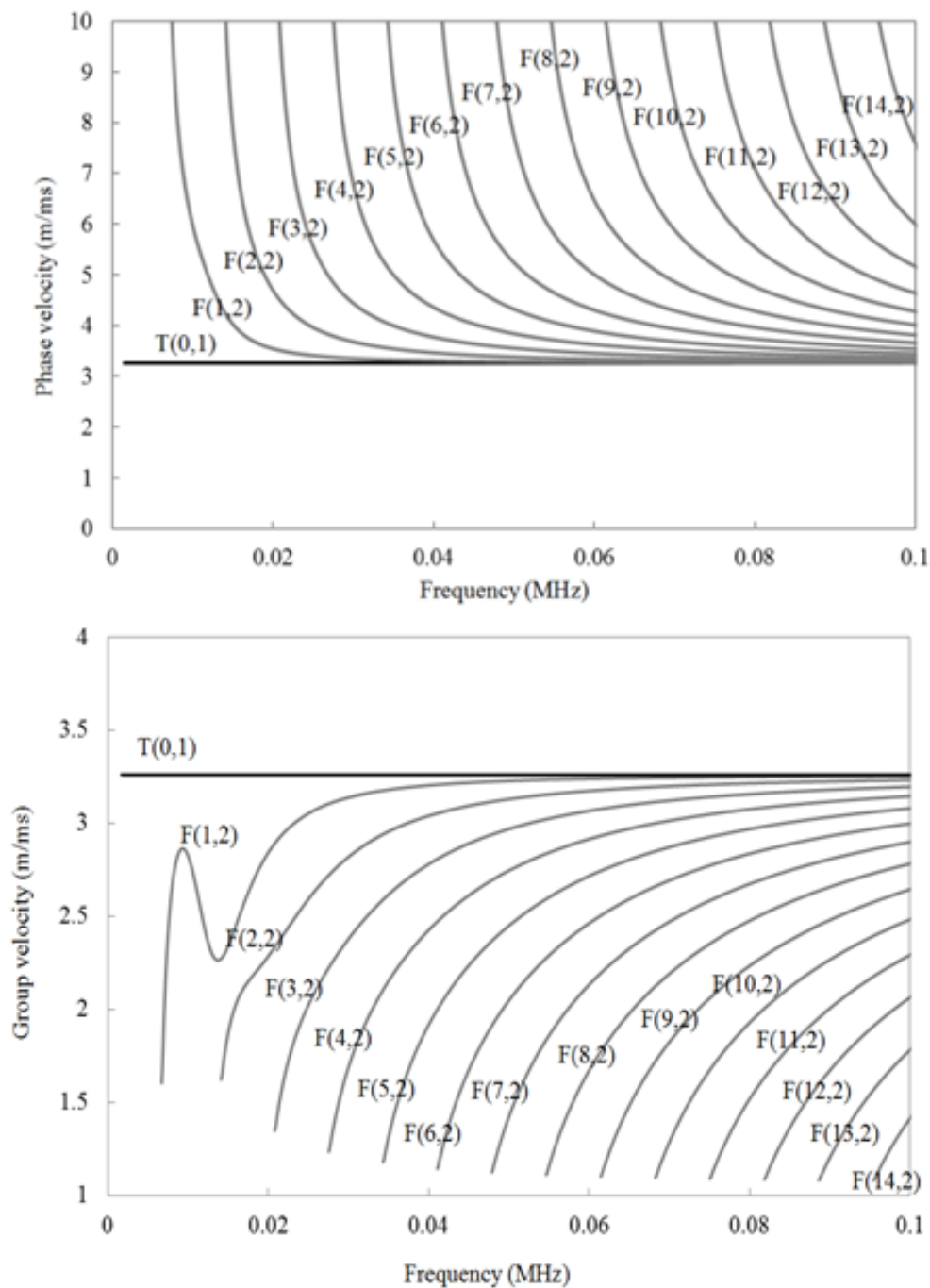
Figure 6.18: Dispersion curve for 6 inch schedule 40 pipe

ring of transducers at incremental forces. The incremental forces were exerted to the transducers by the inflatable collar bladder which was pressurized from 10 psi to 40 psi. A sample UGW response at the minimum and maximum applied force to the transducers are shown in Figure 6.21. The figure represents the sum of all responses given by the individual transducers evenly placed around the circumference of the
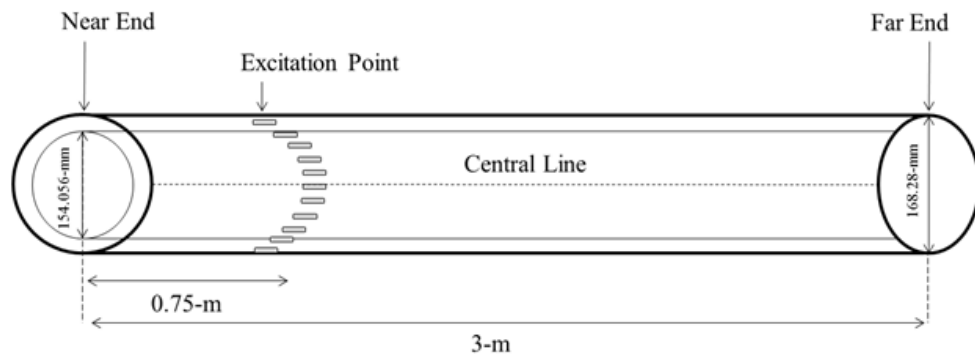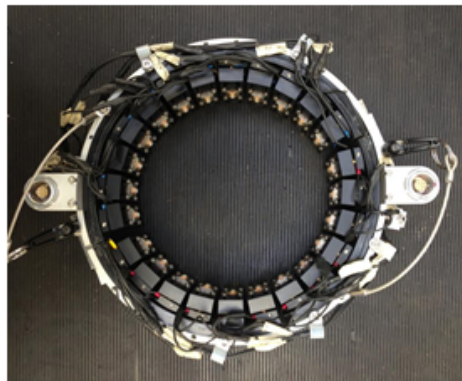
Figure 6.19: Experimental setup

Figure 6.20: Transducer ring used throughout the experiment

pipe. The first echo represents the T(0,1) incident wave mode reflected from the near end of the pipe and the second echo arises from the reverberation of the T(0,1) wave mode between the transducer ring and the near end of the pipe. The peak amplitudes are also extracted and illustrated in Figure 6.22 with the respective SCNR values. It is shown that the SCNR of the T(0,1) wave mode is higher when operating at low force level. This can be explained as less contact area between the transducers and the substrate which causes less reflection from the transducer ring and higher SCNR for the wave mode of interest. It can be also observed that the amplitude of the incident wave mode and the reflected wave mode off the transducer ring are increasing. As was described in Section 6.5.2 the contact area between two elastic bodies is proportionally equivalent to the normal force applied to it by a power of a $\frac{1}{3}$ [104], [105].
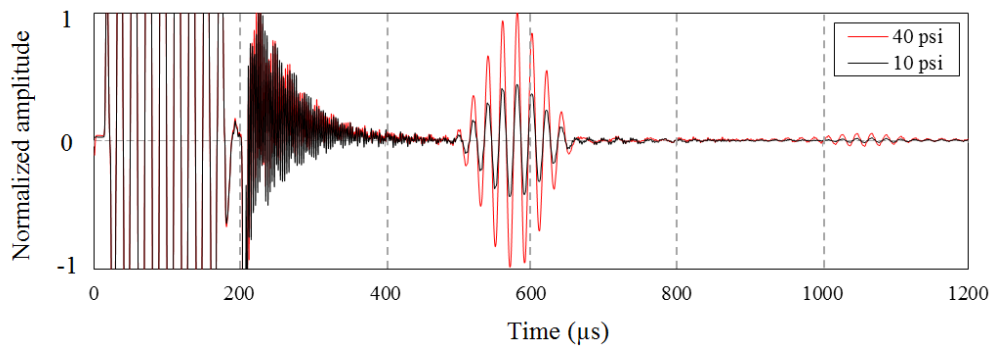
Figure 6.21: Pulse-echo UGW response of the setup described in Figure 6.19
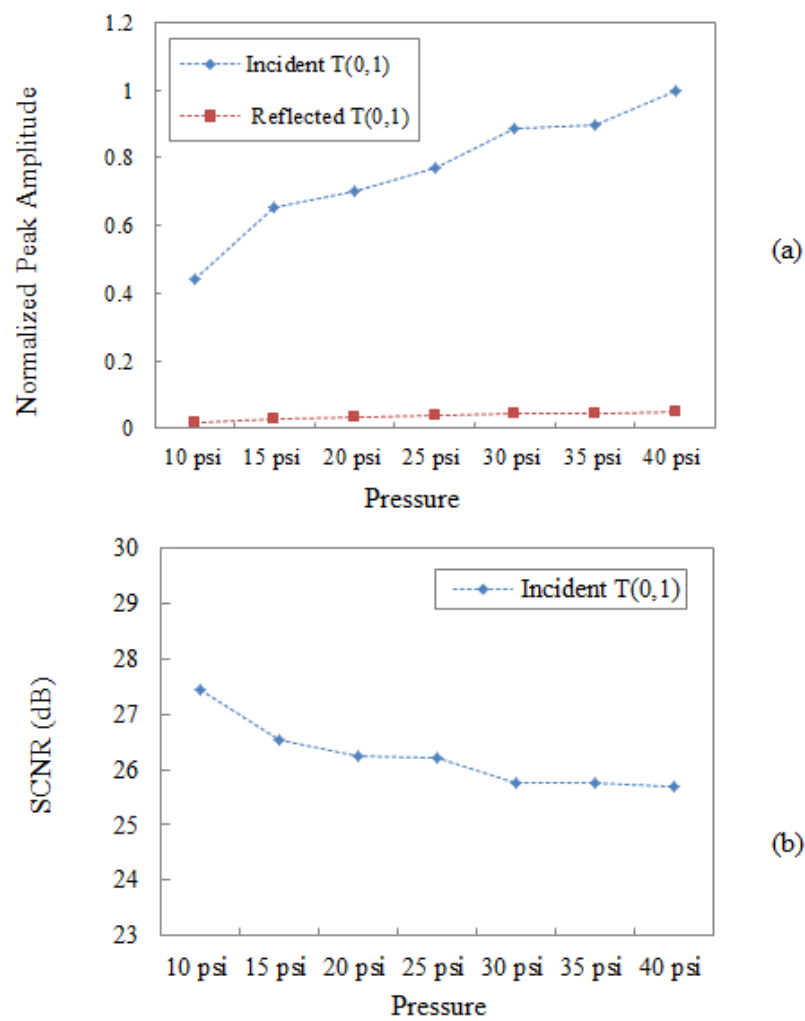

Figure 6.22: (a) Peak amplitude against incremental forces, normalized against maximum value, (b) corresponding SCNR of (a)
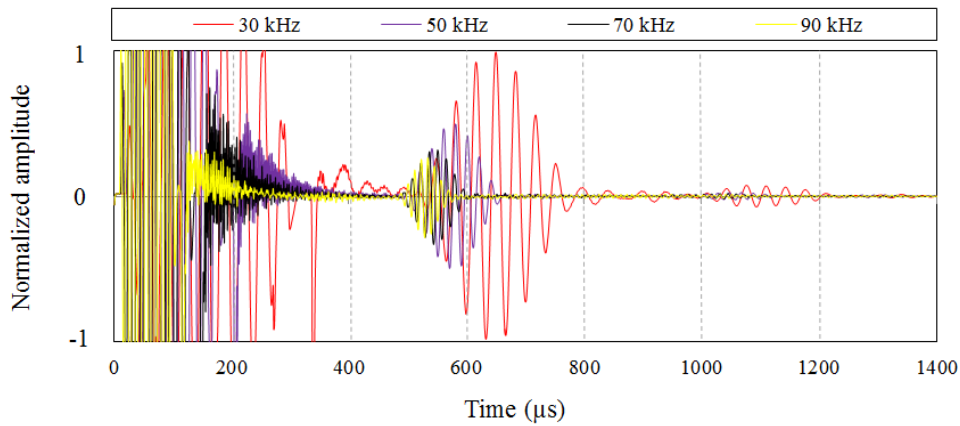
Figure 6.23: Frequency-Sweep: An example of multiple frequency UGW response

6.7.3 Investigation of frequency dependency

A pulse echo frequency-sweep excitation with a constant applied pressure of 40 psi has been performed based on the setup described in Figure 6.19. Sample frequency-sweep response of the scenario is shown in Figure 6.23. The peak amplitudes of the frequency-sweep response are extracted and shown in Figure 6.24. It is evident that the UGWs interacting with transducer rings are present at every operating frequency *i.e.* 20 kHz to 90 kHz[25]. The amplitude of the wave modes decreases by increasing frequency and subsequently the SCNR increases due to the decreasing pattern in electrical impedance/ structural resonance of the transducer. According to Engineer [96] both electrical impedance and structural resonance measurements of the Teletest transducers coincides with the local peaks of amplitude produced in the operational frequency response of (20 to 35 kHz) of the transducer.

6.7.4 Effect of multiple rings

In order to investigate the effect of multiple rings interacting with the propagating T(0,1) wave mode, three phantom transducer rings were gradually coupled to the pipe surface 1.5 m away from the excitation location which is at the end of the pipe (Figure 6.25). The peak amplitudes of the reflected signals were measured with respect to presence of different number of rings at a fixed force of 40-psi and 50 kHz centre frequency. The transducer ring used throughout the experiment

---

[25]The UGW response and the wave modes of interest at 100 kHz are indistinguishable due to the presence of a superior exponentially decaying signal which is believed to be a resonance phenomenon of the transducer coupled to the waveguide. Teletest inspections normally are not operated beyond 90 and or 100 kHz in pipe applications. Thus, the frequency range of interest was set to be up to 90 kHz.

is illustrated in Figure 6.26–(left) and while coupled to the 6 inch schedule 40 pipe shown in Figure 6.26-(right). It can be seen that transducers are evenly spaced however there is a gap between the first and the last modules/transducers which compromises the axisymmetric accommodation of the transducers by 15°. Figure 6.27 shows the UGW response of the T(0,1) wave mode reflected from the transducer rings and the far end of the pipe. The peak amplitudes are acquired and illustrated in Figure 6.28 based on the corresponding number of transducers rings. It can be seen that the amount of reflection off the transducer rings does not change significantly as the number of rings increase from 1 to 3. According to the results illustrated in Figure 6.27 and Figure 6.28, the primary reflection off the transducer rings is initiating from the first ring and the effect of the two other rings are mainly scattering of the T(0,1) wave mode passing through. The effect of the adding rings causes the T(0,1) wave mode (a %100 reflection from the far end of the pipe) to decay respectively. When the number of rings increases from 1 to 3 the amount of energy scattering from the transducer rings increases accordingly. The amount of energy being transmitted through the pipe after interacting with transducer rings is supressed up to %24 and/or 2.38 dB as a result of two added rings. Subsequently the SCNR of the T(0,1) wave mode dropped 2.94 dB when 2 rings of transducers are added to the tool.
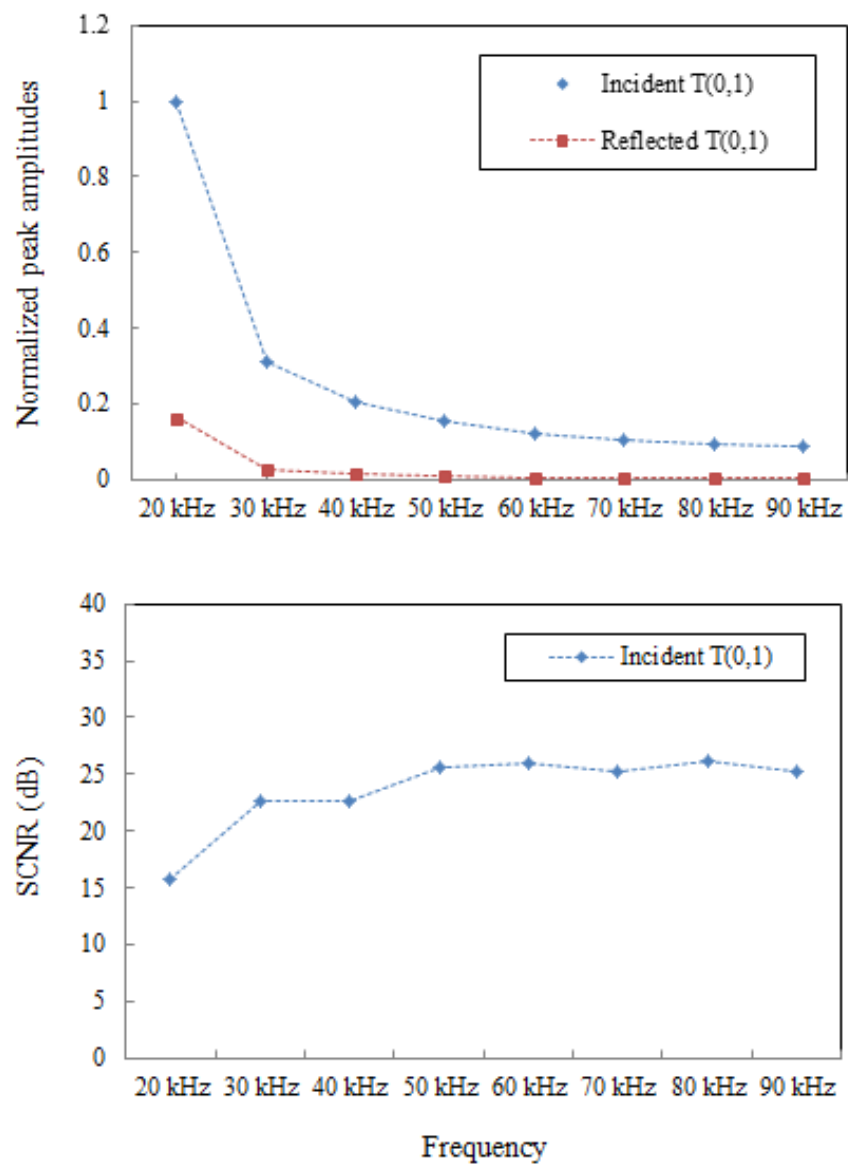
Figure 6.24: (Top) Peak amplitude,(bottom) SCNR of the wave modes against frequencies
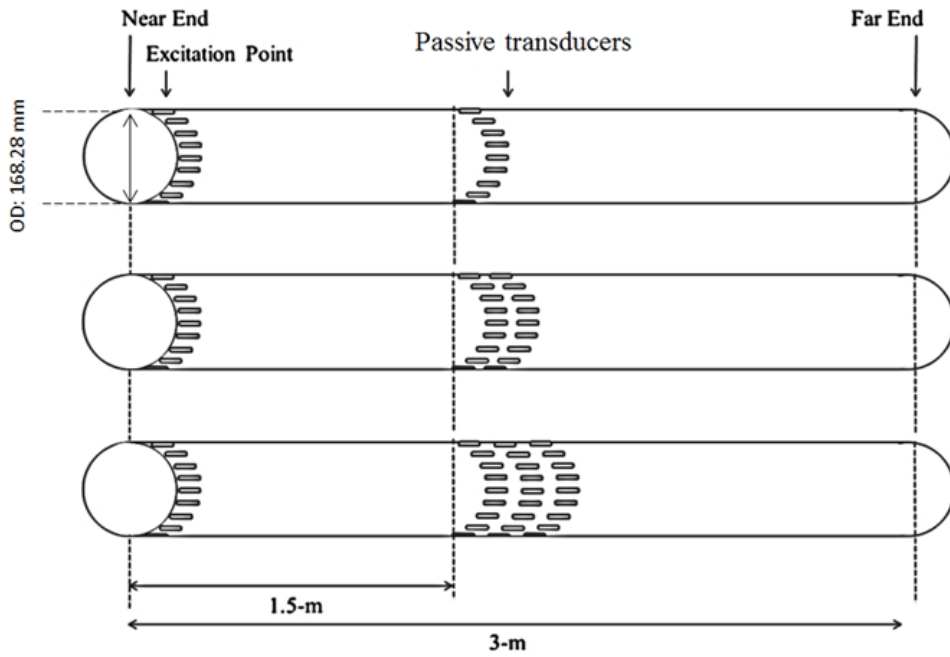
Figure 6.25: Setup considered for the multiple rings

Figure 6.26: Phantom Teletest collar tool (left) and coupled to the 6 schedule 40 inch pipe (right)
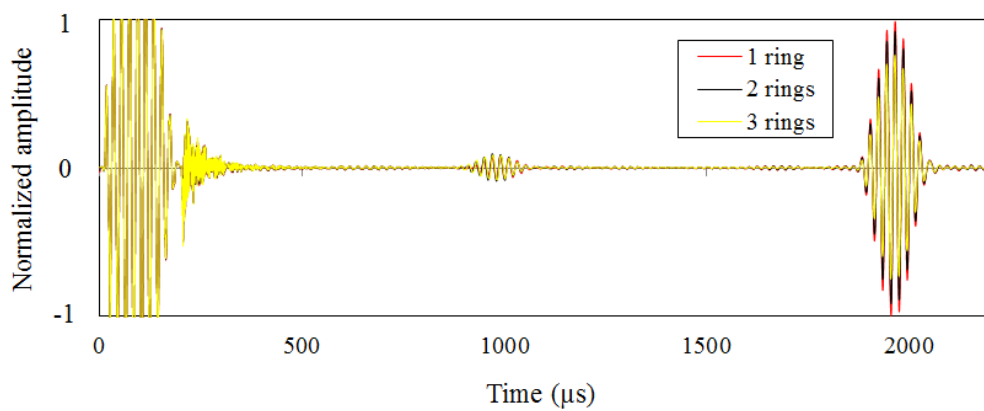

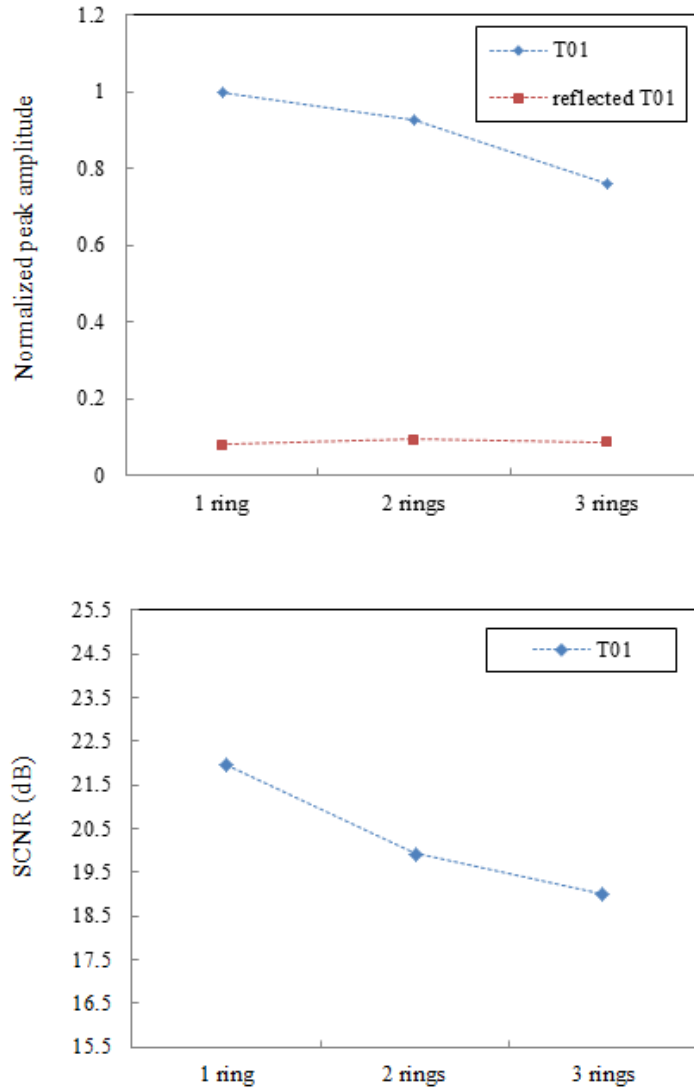Figure 6.27: UGW response of (black line): 1 ring, (blue line): 2 rings, (red line): 3-rings

Figure 6.28: Variation of the amplitude of T(0,1) wave mode while interacting with different transducer rings

6.7.5   Recommendations for practical applications of UGWs

In this chapter the UGWs interacting with the transducer rings have been quantified at the incremental forces commonly used for UGW inspection of pipelines. The results indicate that the reflected wave modes off the transducer rings appear with the SCNR of (up to) 25.7 dB at 50 kHz, 40 psi. The quantified responses could be used to predict the effect of the phenomenon in different scenarios when employing UGWs for inspections. The scenarios in which the phenomenon may have disruptive effects are highlighted in below:

a) *Research laboratory experiments*

In research/laboratory experiments, the length of the structures under investigation are normally shorter than the length of the structures in field inspections. Therefore, the wave modes could interact with the transducer rings and appear in the UGW response superposing with different features in the structures (*e.g.* artificial defects, welds, stands, *etc.*) causing possible wrong measurements. In order to avoid the problem, careful experimental setup should be considered to predict the ToA (equation provided in (6.2)) of the reflected wave modes off the transducer rings using *a priori* knowledge of the group velocity dispersion curve. Therefore any possible superposition with the responses initiated from the structural features and possible wrong measurements could be avoided.

b) *UGW inspection of pipelines*

The on-site inspections of pipelines are normally performed using pulse-echo UGW excitations up to 100 metres. It is understood that the UGWs interacting with the transducer rings can appear in reverberation scenarios where the UGWs interact with the structural elements and reflect back towards the transducer rings. This can be predicted by the amount of reflection a structural feature can produce *e.g.*, pipe end/flange: %100 reflector, standard weld: %20 reflector, *etc.* Therefore, the UGWs interacting with the transducers can be identified based on the SCNR sensitivity[26] of the commercially available UGW systems and/or contribute to the coherent noise [9], [123], [124], [125], [126].

For instance, if a structural feature produces %R reflection ($(20log_{10}R/100)dB$) and assuming that the SCNR of the UGWs interacting with transducers is SdB,

---

[26]The SCNR sensitivity of the commercially available UGW systems varies upon the application of the inspection. According to best of author's knowledge, this value can approximately vary between 20 to 50 dB depending on the type of structure under investigation, transducer coupling, transducer efficiency, type of UGW unit, etc.

the overall SCNR after the reverberation between the transducer and the structural feature will be $S + 2((20log_{10}(0.0R)))$.

6.8   Chapter summary

In this chapter the occurrence of mode conversion has been verified due to the effect of the transducer being coupled on the waveguide which subsequently acted as a non-axisymmetric feature on an aluminium rod. The UGWs interacting with the transducers contributing as a component of the coherent noise existing in the UGW response were quantified. It was demonstrated that in the operating frequency region, the mode conversions happen from flexural to longitudinal and and vice versa.

The FE modelling performed was experimentally validated and it was demonstrated that the transducer has to be a 3D geometric feature in order to achieve an accurate UGW response. Therefore, it is highly recommended that a 3D geometric transducer is to be used for modelling practical UGW applications rather than using a single point excitation. A further iteration of the presented FE model can introduce a force parameter to quantitatively predict the effects of force on mode conversions from transducers. This could be beneficial for future UGW array design. Despite the fact that the FEA procedure used throughout the chapter reaches a closer agreement between the theoretical predictions and experimental results; it should be taken into account that the computation time increases by approximately from %50 to %75 on ABAQUS software depending on the type of mesh and modelling specifications.

Further results indicated that the amplitude of the mode converted signal increases non-linearly with respect to the incremental forces. This amplitude at the lowest force (*i.e.* 5 N) was negligible and was masked by the noise initiating from the ringing of the transducer.

A frequency-sweep excitation was also performed to examine the frequency dependency of the coupling dependent mode conversion. It was illustrated for each operational frequency that has been excited (20 kHz to 100 kHz), the mode conversion behaviour which is instigated by wave mode reflections off the transducer is always present.

The 3D-LDV was used as a non-contact receiver and the superposed wavepacket, could be separated to its constituent elements, L(0,q) & F(β,q). Therefore, the existing wave modes in the waveguide were identified and supported the FE

models and experimental validations.

The UGWs interacting with the piezoelectric transducer rings have been studied on a 6 inch schedule 40 pipe. It was demonstrated that in the operating frequency region, the T(0,1) wave mode scatters (from SCNR of 27.4 dB to 25.6 dB at 10 to 40 psi applied pressure) when interacting with the transducer ring. The empirical results indicated that the amplitude of the reflected T(0,1) wave mode off the transducer ring increases with respect to the incremental forces. A frequency-sweep excitation was also performed to examine the frequency dependency of the coupling dependent reflections of the T(0,1) wave mode. It was illustrated for each operational frequency that has been excited (20 kHz to 90 kHz), the reflections which is instigated by wave mode reflections off the transducer is always present.

Further investigations were conducted to quantify the effect of multiple rings on the UGW response. The results indicated that the primary reflection off the transducer rings is initiating from the first ring and the effect of the two other rings are mainly scattering of the T(0,1) wave mode passing through. The amount of energy being transmitted through the pipe after interacting with transducer rings is supressed up to %24 as a result of two added rings. Subsequently the SCNR of the T(0,1) wave mode dropped 2.94 dB when 2 rings of transducers are added to the tool.

In conclusion, the impact of coupling dependent reflections and mode conversions, which was studied throughout the chapter, can potentially become a disruptive matter in the practical application of UGW inspection techniques. Additionally, the unexpected pulse can be superposed with discontinuities along the structure and causing possible wrong measurements. Resolving the aforementioned problem may lead to considerable reduction in the coherent noise, improvements in UGW monitoring systems and greater confidence in measurements. Thus, further research needs to be conducted in an attempt to compensate the effect of this phenomenon through novel UGW signal processing techniques and/or UGW array and transducer design on different type of structures.

Chapter 7

Conclusions and Recommendations for Future Works

7.1 Main findings of this thesis

The aim of the work presented in this thesis was to develop advanced signal processing techniques to enable quantitative wave mode identification in the multimodal UGW response. Two signal processing techniques were developed to identify different longitudinal and flexural UGW modes in superposed wave-packets in order to ease the structural feature detection process. Unwanted wave modes appearing in the UGW response were identified to be caused by reflections and mode conversions from transducer coupling. The phenomenon was studied in detail with useful recommendations for future works.

7.1.1 Signal processing techniques applied to multimodal ultrasonic guided wave signal

A Frequency-Sweep Examination (FSE) technique was introduced and shown to be a promising technique for structural feature detection in complex UGW inspections. According to the signal synthesis and experimental findings, the proposed signal processing technique is useful for ToA/group velocity extraction and wave mode identification of superposed UGWs. The technique obtained the number of wave modes present with accurate quantitative information allowing a portion of group velocity dispersion curve to be computed. It is also expected to be best

suited for one dimensional structures *e.g.* rods, bars, pipes, rails, *etc.* as it requires frequency-sweep measurement using the pulse echo technique. Therefore, further validations maybe required for the other types of structures.

The advantage of the proposed technique over the two dimensional Fourier transform methods is on performing pulse-echo frequency-sweep excitations of UGWs rather than several pitch-catch measurements which can be time a consuming and/or expensive process.

The assumption of a known propagation distance is a drawback of the technique which needs to be taken into account in field inspection as well as the one presented by TFR methods. In addition, the time domain separation has not been performed in this thesis as the research was mainly focused on wave mode identification in which was achieved in Fourier domain. Customized filtering in FSS domain can be a possible solution to such a requirement for future research directions. The future work on this topic can focus on empirically plotting the entire phase and group velocity dispersion curves assuming that the length of the structure is unknown. In addition, based on the empirical results the FSE technique showed promise for wave mode identification of multimodal UGW response including up to three wave modes simultaneously. Further works can also be focused on investigations on other types of structures where more than three wave modes are of concern. Since the validation of the technique was carried out using an aluminium rod, the technique is best suited for UGW testing of one dimensional structures such as pipes, rods, bars, rails *etc.* which further validations may be required for these types of structures.

Beside the FSE technique, an Iterative technique comprising Dispersion Compensation (IDC) using pulse compression was proposed. The technique extracted the ToA and iteratively searched for the propagation distance of individual wave modes using *a priori* knowledge of group velocity dispersion curves. Signal synthesis for a single modal case and a multimodal case successfully extracted the ToA and the propagation distance of individual wave modes. According to the experimental results, the ToA and the corresponding propagation distance of individual wave modes could be extracted with up to %5.8 error. Moreover, considerable SNR improvements in the signal synthesis and experimental validation were achieved for individual wave modes.

It was empirically demonstrated that the proposed technique is best suited for the identification of dispersive wave modes (*e.g.* F(1,1) wave mode) and may not successfully derive the propagation distance of the fundamental longitudinal wave

mode (L(0,1)) since it experienced very low dispersion in the operating frequency region. However, in such regard, the sharp peaks for the non-dispersive wave modes appear at a constant time in the frequency range of interest. This peak represents the ToA of the longitudinal wave mode, L(0,1) and can be converted to the propagation distance since the group velocity dispersion is known.

During the experimental validations the dispersion compensated responses were cross-correlated with the signal generated by the Teletest unit (Figure 5.10). Therefore, it is also expected that the errors in the extraction of the propagation distance to be further reduced if the dispersion compensated responses are cross-correlated with the signal generated by the transducer which could pave the way to future works on this topic. In addition, since the dispersion compensation technique is highly dependent on the accuracy of the dispersion curve, the precision of the extracted quantitative information such as ToA and the propagation distance are expected to be improved if the dispersion curves are experimentally acquired.

The application of the IDC technique was compared with FSE technique. The ToAs calculated by the two aforementioned techniques were given with close agreements. The IDC and FSE technique use *a priori* knowledge of the propagation distance and the group velocity dispersion curve respectively to measure the ToA of the individual wave modes. Thus the two techniques could be combined to compute the dispersion curve and also enhance the SNR at the same time in an automated computerized process with no manual intervention which is aimed for the future directions of the subject

7.1.2 Ultrasonic guided waves interacting with piezoelectric transducers

The aforementioned signal processing techniques identified unwanted wave-packets in the UGW response which were studied to be caused by scattering from the piezoelectric transducer. The occurrence of mode conversion has been verified due to the effect of the transducer being coupled on the waveguide which subsequently acts as a non-axisymmetric feature. It was quantified that the UGWs interacting with the transducers contribute to the UGW response as one of the components of the coherent noise. It was demonstrated that in the operating frequency region, the mode conversions off the transducer take place from flexural to longitudinal and vice-versa. The FE model performed was empirically validated and it was demonstrated that the transducer has to be a 3D geometric feature in order to achieve an accurate UGW response. Thus it is recommended that a 3D geometric transducer is to be used for modelling practical UGW applications rather than using a single point excitation. A further iteration of the presented FE model can introduce a force parameter to quantitatively predict the effects of force on mode conversions from transducers. This could be beneficial for future UGW array design. Despite the fact that the FEA procedure used throughout the chapter reaches a closer agreement between the theoretical predictions and experimental results; it should be taken into account that the computation time increases by approximately %75 on ABAQUS software.

Empirical results indicated that the amplitude of the mode converted signal increases non-linearly with respect to the incremental forces. This is due to the contact area between two elastic bodies which is proportionally equivalent to the normal force applied to it by a power of a $\frac{1}{3}$. This amplitude at the lowest force (*i.e.* 5 N) was negligible and the signal was masked by the noise initiating from the ringing of the transducers. In this case due to the low level of force applied to the transducer, the coupling was affected and the UGW response experienced a relatively long ringing phenomenon.

A frequency-sweep excitation was also performed to examine the frequency dependency of the coupling dependent mode conversion. It was illustrated for each operational frequency that has been excited (20 kHz to 100 kHz), the mode conversion behaviour which is instigated by wave mode reflections off the transducer is always present.

The 3D-LDV was used as a non-contact receiver and the superposed wave-packet, could be separated to its constituent elements, L(0,q) & F(β, q). Therefore,

the existing wave modes in the waveguide were identified and supported the FE models and experimental validations.

The phenomenon has also been investigated on a 6 inch schedule 40 pipe considering torsional excitation of the UGWs, T(0,1) wave mode. It was demonstrated that in the operating frequency region, the T(0,1) wave mode scatters (from SCNR of 27.4 dB to 25.6 dB at 10 to 40 psi applied pressure) when interacting with the transducer rings. The empirical results indicated that the amplitude of the reflected T(0,1) wave mode off the transducer ring increases with respect to the incremental forces. A frequency-sweep excitation was also performed to examine the frequency dependency of the coupling dependent reflections of T(0,1) wave mode. It was demonstrated for each operational frequency that has been excited (20 kHz to 100 kHz), the reflections which is instigated by wave mode reflections off the transducer is always present.

The quantified responses could be used to predict the effect of the phenomenon in different scenarios when employing UGWs. The scenarios that the phenomenon may have disruptive effects were categorized as 'research laboratory experiments' and 'field inspections'. In the research laboratory experiments the length of the structures under investigation are normally shorter than the length of the structures in field inspections. Therefore, the wave modes could interact with the transducer rings and appear in the UGW response superposing with different features in the structures (*e.g.* artificial defects, welds, stands, etc.) causing possible wrong measurements of the structural features. In order to avoid the problem, careful experimental setup should be considered to predict the ToA of the reflected wave modes off the transducer rings and avoid any possible superposition with the responses initiated from the structural features.

In field inspections it is expected that the UGWs interacting with the transducer rings can appear in reverberation scenarios where the UGWs interact with the structural elements and reflect back towards the transducer rings. This can be predicted by the amount of reflection a structural feature can produce *e.g.*, pipe end/flange: %100 reflector, standard weld: %20 reflector, etc. Therefore, the UGWs interacting with the transducers can be identified based on the SCNR sensitivity of the commercially available UGW systems and/or contribute to the coherent noise.

It is intended to perform the future studies of the reported phonomenon on other types of structrue such as, pipes with different thickness/length, plates, bars, *etc.* Resolving the aforementioned problem may lead to considerable reduction in the

coherent noise, improvements in UGW monitoring systems and greater confidence in measurements. Thus, further research needs to be conducted in an attempt to compensate the effect of this phenomenon through novel UGW signal processing techniques and/or UGW array and transducer design.

Chapter 8

References

[1] G. Chen, X. Wang, J. Wang, J. Liu, T. Zhang, W. Tang, "Damage investigation of the aged aluminium cable steel reinforced (ACSR) conductors in a high-voltage transmission line," *Elsevier, Engineering Failure Analysis*, vol. 19, pp. 13-21, 2012.

[2] D. Siegert, P. Brevet, "Fatigue of stay cables inside end fittings: High frequencies of wind induced vibrations," in *Proceedings of OIPEEC technical meeting*, September 2003.

[3] L. Garverick, Corrosion in the petrochemical industry, USA: ASM International, 1995, pp. 277-281.

[4] Associated Press, "The press democrat," 26 September 2014. [Online]. Available: http://www.pressdemocrat.com/news/2889538-181/officials-concerned-about-rod-corrosion. [Accessed 30 01 2015].

[5] NACE International corrosion safety (A NACE International White Paper), Corrosion control plan for bridges, Houston, USA: NACE Internationa, 2012 , pp. 1-30.

[6] P. Hopkins, "The structural integrity of oil and gas transmission pipelines," Comprehensive Structural Integrity, vol. 1, pp. 3-7, 2003.

[7] ASME B36.10M-2004, p. 1.

[8] The United States Department of Justice, "United States V. BP Products North America (D. ALASKA)," October 2010. [Online]. Available: http://www.justice.gov/enrd/3509.htm. [Accessed 29 01 2015].

[**9**] Plant Integrity Ltd., "Teletest Focus Long Range Ultrasonic System Specification," TWI, Cambridge, United Kingdom, 6th Feb. 2007.

[**10**] S. Odenwald, "Space weather," STEM Resource Development National Institute of Aerospace, [Online]. Available: http://www.solarstorms.org/Spipeline.html. [Accessed 29 01 2015].

[**11**] G. White, "The telegraph," 1 April 2009. [Online]. Available: http://www.telegraph.co.uk/finance/newsbysector/energy/oilandgas/5091013/US-sues-BP-over-Prudhoe-Bay-oil-spill.html. [Accessed 29 01 2015].

[**12**] CNN news, "NTSB: Design flaw led to Minnesota bridge collapse," CNN US, 15 November 2008. [Online]. Available: http://edition.cnn.com/2008/US/11/14/bridge.collapse/#cnnSTCPhoto. [Accessed 29 01 2015].

[**13**] P. Catton, "Long Range Ultrasonic Guided Waves for the Quantitative Inspection of Pipelines," *Brunel University PhD Thesis*, pp. 2-140, 2009.

[**14**] G. Gautschi, "Piezoelectric Sensorics: Force, Strain, Pressure, Acceleration and Acoustic Emission Sensors, Materials and Amplifiers," Springer, 1st edn, 2002.

[**15**] J. Krautkramer, H. Krautkramer, "Ultrasonic testing of materials," Newyork, Springer Verlag, 4th edn, 1990.

[**16**] Plant Integrity Ltd., TWI, 2015. [Online]. Available: http://www.plantintegrity.com/. [Accessed 29 01 2015].

[**17**] TWI Ltd., "Successful inspection beyond pipe bends using Teletest®," 2015. [Online]. Available: http://www.twi-global.com/news-events/case-studies/successful-inspection-beyond-pipe-bends-using-teletest-525/. [Accessed 29 01 2015].

[**18**] J. L. Rose, "Successes and Challenges in Ultrasonic Guided Waves for NDT and SHM," in *Proceedings of the National Seminar & Exhibition on Non-Destructive Evaluation*, Dec. 10-12, 2009.

[**19**] W. Ostachowicz, P. Kudela, M. Krawczuk, A. Zak, "Introduction to the Theory of elastic Waves," in *Guided Waves in Structures for SHM*, Chichester, West Sussex, United Kingdom, John Wiley & Sons Ltd., 2012, pp. 1-46.

[20] Waves In Solids (WINS) LLC, "Applications of Long Range Ultrasound: Benefits, Limitations, and Technology Comparisons," 6 May 2010. [Online]. Available: http://www.slideshare.net/subash_j/guided-wave-ultrasound-principles-and-apllications. [Accessed 2015 01 2015].

[21] H. Meitzler, "Mode coupling occurring in the propagation of elastic pulses in wires," *Journal of Acoustical Society of America*, vol. 33, no. 4, pp. 435-445, 1961.

[22] H. Lamb, "On Waves in An Elastic Plate," *Proceedings of the Royal Society of London Series A*. 93, no. 651, pp. 114-128, 1971.

[23] D. C. Worlton, "Experimental confirmation of Lamb waves at megacycle frequencies," *Journal of Applied Physics*, vol. 32, pp. 697-971, 1961.

[24] B. Pavlakovic, M. J. S. Lowe, D. N. Alleyne, P. Cawley, "Disperse:A general purpose program for creating dispersion curves," in *Review of Progress in Quantitative Nondestructive Evaluation. vol. 16, D. O. Thompson and D. E. Chimenti, Eds. New York: Plenum*, p. 185-192, 1997.

[25] NDT Education Resource Center, Iowa State University, 2001-2014. [Online]. Available: www.ndt-ed.org. [Accessed 04 09 2014].

[26] P. Cawley, D. N. Alleyne, "The use of Lamb Waves for the Long-Range Inspection of Large Structures," *Elsevier Ultrasonics*, vol. 34, no. 2, p. 1996, 287-290.

[27] A. H. Nuttal, "Some Windows with Very Good Sidelobe Behaviour," *IEEE Transactions on Acoustics, Speech and Signal Processing*, vol. 291, no. 1, pp. 84-91, 1998.

[28] J. Y. Stein, Digital signal processing: A computer science perspective, New York: John Wiley & Sons, Inc., 2000.

[29] S. R. Taghizadeh, "Digital Signal Processing Case Study: Part-3 Discrete-Time Signals & Systems," University of North London , 2000.

[30] J. J. Benedetto, I. Konstantinidis, M. Rangaswamy, "Phase-Coded waveforms and their designs," *IEEE Signal Processing Magazine*, vol. 26, no. 1, pp. 22-31, 2009.

[**31**] S. W. Golomb, G. Gong, "Signal Design for Good Correlation For Wireless
        Communication, Cryptography, and Radar," Cambridge, United Kingdom,
        Cambridge University Press, 2005.

[**32**] J. R. Klauder, A. C. Price, S. Darlington, W. J. Albersheim, "The Theory
        and Design of Chirp Radars," *Bell Labs Technical Journal*, vol. 39, no. 4, pp.
        745-708, 2013.

[**33**] T-H. Gan, D. A. Hutchins, R. J. Green, M. K. Andrews, P. D. Harris, "Non-
        contact, high-resolution ultrasonic imaging of wood samples using coded
        chirp waveforms," *IEEE Trans. on Ultrasonics, Ferroelectrics and Frequency
        Control*, vol. 52, no. 2, pp. 280-288, 2005.

[**34**] D. Hutchins, P. Burrascano, L. Davis, S. Laureti, M. Ricci, "Coded wave-
        forms for optimised air-coupled ultrasonic nondestructive evaluation," *Else-
        vier Ultrasonics*, vol. 54, pp. 1745-1759, 2014.

[**35**] S. W. Smith, "Chapter 11: Fourier Transform Pairs, chirp signals," in
        The Scientist and Engineer's Guide to Digital Signal Processing, San Diego,
        United States, California Technical Publishing, 1997, pp. 209-225.

[**36**] T. Smyth, "CMPT 468: Frequency Modulation (FM) Synthesis," School of
        Computing Science, Simon Fraser University, Burnaby BC, Canada, 2013.

[**37**] J. Watkinson, "The Art of Digital Audio," London, United kingdom, Focal
        Press, edn 1, 1988, pp. 122-135.

[**38**] R. E. Crochiere, L. R. Rabiner, "Interpolation and Decimation of Digital
        Signals— A tutorial review," Proceedings of the IEEE, vol. 69, no. 3, pp.
        300-330, 1981.

[**39**] C. Langton, "Complex to real," 2014. [Online]. Available: http:
        //complextoreal.com/tutorials/tutorial-6-3-dft-fft-part-5. [Ac-
        cessed 12 09 2014].

[**40**] J. W. Cooley, J. W. Tukey, "An algorithm for the machine calculation of
        complex Fourier series," *Mathematics of Computation*, vol. 19, p. 297-301,
        965.

[**41**] L. Cohen, "Time-frequency distributions-A review," *Proceedings of the IEEE*,
        vol. 77, no. 7, pp. 941-981, 1989.

[**42**] P. Flandrin, P. Goncalv, "Geometry of Affine Time-Frequency Distributions," *Applied and computational harmonic analysis*, vol. 3, no. 10, pp. 10-39, 1996.

[**43**] L. Rayleigh, "On Waves Propagated Along the Plane Surface of An Elastic Solid," Proceedings of the London Mathematical Society, vol. 17, pp. 4-11, 1887.

[**44**] H. Helmholtz, On the Sensations of Tone, New York: Dover Publications, 1954.

[**45**] H. Lamb, The Dynamical Theory of Sound, New York: Dover Publication, 1960.

[**46**] I. Viktorov, Rayleigh and Lamb Waves - Physical Theory and Applications, New York: NY: Plenum Press, 1967.

[**47**] M. G. Silk, K. F. Bainton, "The propagation in metal tubing of ultrasonic wave modes equivalent to lamb waves," *Elsevier Ultrasonics*, vol. 17, no. 1, pp. 11-19, 1979.

[**48**] W. Böttger, H. Schneider, W. Weingarten, "Prototype EMAT system for tube inspection with guided ultrasonic waves," *Elsevier, Nuclear Engineering and Design*, vol. 102, no. 3, pp. 369-376, 1987.

[**49**] P. Mudge, A. M. Lank, D. N. Alleyne, "Long Range Method of Detection of Corrosion under Insulation in Process Pipework," in *5th European Union Hydrocarbons Symposium*, Edinburg, 26-28 November 1996.

[**50**] P. Cawley, D. N. Alleyne, "The use of Lamb Waves for the Long-Range Inspection," *Elsevier Ultrasonics*, vol. 34, no. 2-5, pp. 287-290, 1996.

[**51**] J. L. Rose, "A Baseline and Vision of Ultrasonic Guided Wave Inspection Potential," *Journal of Pressure Vessel Technology*, vol. 124, no. 3, pp. 273-282, 2002.

[**52**] R. B. Thompson, S. C. Lee, J. F. Smith, "Relative Anisotropies of Plane Waves and Guided Modes in Thin Orthotropic Plates: Implication for Texture Characterization," *Elsevier Ultrasonics*, vol. 25, pp. 133-137, 1987.

[53] J. J. Ditri, J. L. Rose, "Excitation of Guided Elastic Wave Modes in Hollow Cylinders by Applied Surface Tractions," *Journal of Applied Physics*, vol. 72, pp. 2589-2597, 1992.

[54] D. N. Alleyne, M. Lowe, P. Cawley, "The Inspection of Chemical Plant Pipework Using Lamb Waves: Defect Sensitivity and Field Experience," *Review of Progress in Quantitative Nondestructive Evaluation, eds., D. O. Thompson and D. E. Chimenti*, Vols. 15, Plenum Press, New York, NY, pp. 1859-1866, 1996.

[55] S. P. Pelts, J. L. Rose, "Source Influence Parameters on Elastic Guided Waves in an Orthotropic Plate," *Journal of Acoustical Society of America*, vol. 99, no. 4, pp. 2124-2129, 1996.

[56] H. J. Shin, J. L. Rose, "Guided Wave Tuning Principles for Defect Detection in Tubing," *Journal of Nondestructive Testing and Evaluation*, vol. 17, no. 1, pp. 27-36, 1998.

[57] D. N. Alleyne, M. J. S. Lowe, P. Cawley, "The Reflection of Guided Waves From Circumferential Notches in Pipes," *Journal of Applied Mechanics* , vol. 65, no. 3, pp. 635-641, 1998.

[58] B. Pavlakovic, M. J. S. Lowe, D. N. Alleyne, P. Cawley, "Disperse:A general purpose program for creating dispersion curves," in *Review of Progress in Quantitative Nondestructive Evaluation*, vol. 16, no. D. O. Thompson and D. E. Chimenti, Eds. New York: Plenum, pp. 185-192, 1995.

[59] R. Sicard, J. Goyette, D. Zellouf, "A numerical dispersion compensation technique for time recompression of Lamb wave signals," *Elsevier Ultrasonics*, vol. 40, no. 1-8, pp. 727-732, 2002.

[60] P. Wilcox, "A Rapid Signal Processing Technique to Remove the Effect of Dispersion from Guided Wave Signals," *IEEE transactions on ultrasonics ferroelectrics and frequency control*, vol. 50, no. 4, pp. 419-427, 2003.

[61] L. Liu, F. G. Yuan, "A Linear Mapping Technique for Dispersion Removal of Lamb Waves," *Structural Health Monitoring*, vol. 9, no. 1, pp. 75-86, 2009.

[62] B. Xu, L. Yu, V. Giurgiutiu, "Lamb Wave Dispersion Compensation in Piezo-electric Wafer Active Sensor Phased-Array Applications," in *SPIE Health*

Monitoring of Structural and Biological Systems III conference, San Diego, USA, March 2009.

[**63**] B. Xu, L. Yu, V. Giurgiutiu, "Advanced methods for time-of-flight estimation with application to lamb wave structural health monitoring," in *7th International Workshop on Structural Health Monitoring*, Palo Alto, USA, 2009.

[**64**] W. Sachse, Y-H. Pao, "On determination of phase and group velocities of dispersive waves in solids," *Journal of Applied Physics*, vol. 49, no. 8, pp. 4320-4327, 1978.

[**65**] D. Alleyne, P. Cawley, "A Two-Dimensional Fourier Transform Method for the Measurement of Propagating Multimode Signal," *Journal of the Acoustical Society of America*, vol. 89, no. 3, pp. 1159-1168, 1991.

[**66**] D. N. Alleyne, "The nondestructive testing of plates using ultrasonic Lamb waves," *Imperial College London Ph.D. Thesis*, pp. 1-231, 1991.

[**67**] H. Prosser, M. D. Seale, "Time-Frequency analysis of the dispersion of Lamb modes," *Journal of Acoustical Society of America*, vol. 105, no. 5, pp. 1841-1847, 1999.

[**68**] J. G. Minonzio, M. Talmant, and P. Laugier, "Measurement of guided mode phase velocities using multi-emitters and multi-receivers arrays in contact and transmission matrix analysis: Application to cortical bone evaluation," in *IEEE International Ultrasonics Symposium Proceedings*, Rome, Italy, 2009.

[**69**] K. Xu, D. Ta, W. Wang, "Multiridge-Based Analysis for Separating Individual Modes From Multimodal Guided Wave Signals in Long Bones," *IEEE Transactions on Ultrasonics, Ferroelectrics, and Frequency Control*, vol. 57, no. 11, pp. 2480-2490, 2010.

[**70**] R. Mallet, "Signal Processing for Non-Destructive Testing," *Brunel University London Engineering Doctorate Thesis*, pp. 1-242, 2007.

[**71**] X. Song, D. Ta, W. Wang, "Analysis of superimposed ultrasonic guided waves in long bones by the joint approximate diagonalization of eigen-matrices algorithm," *Elsevier Ultrasound in Medicine & Biology*, vol. 37, no. 10, pp. 1074-13, 2011.

[**72**] K. Xu, D. Ta, P. Moilanen, W. Wang, "Mode separation of Lamb waves based on dispersion compensation method," *Journal of Acoustical Soiety of America*, vol. 131, no. 4, pp. 2714-2722, 2012.

[**73**] L. Zeng, J. Lin, "Chirp-based dispersion pre-compensation for highresolution Lamb wave inspection," *Elsevier NDT&E International*, vol. 61, pp. 35-44, 2013.

[**74**] T. Misaridis, J. A. Jensen, "Use of Modulated Excitation Signals in Medical Ultrasound. Part 1: Basic Concepts and Expected Benefits," *IEEE Transactions on Ultrasonics, Ferroelectrics and Frequency Control*, vol. 52, no. 2, pp. 177-191, 2005.

[**75**] R. E. Challisand, V.G. Ivchenko, "Sub-threshold sampling in a correlation-based ultrasonic spectrometer," *Measurement Science and Technology*, vol. 22, no. 2, 2011.

[**76**] K. Thornicroft, "Ultrasonic Guided Wave Testing of Pipelines using a Broadband Excitation," *Brunel University London, PhD Thesis*, pp. 1-145, 2015.

[**77**] T-H. Gan, D.A. Hutchins, D.R. Billson, D.W. Schindel, "The use of broadband acoustic transducers and pulse-compression techniques for air-coupled ultrasonic imaging," *Ultrasonics*, vol. 39, no. 3, pp. 181-194, 2001.

[**78**] T-H. Gan, D. A. Hutchins, R. Green, "Non-Contact, High resolution Ultrasonic Imaging of Wood Samples Using Coded Chirp Waveforms," *IEEE Transactions on Ultrasonic, Ferroelectrics and Frequecy Control*, vol. 52, no. 2, pp. 280-288, 2005.

[**79**] M. Garcia-Rodriguez, Y. Yañez, M.J. Garcia-Hernandez, J. Salazar, A. Turo, J.A. Chavez, "Application of Golay codes to improve the dynamic range in ultrasonic Lamb waves air-coupled systems," *NDT&E International*, vol. 43, no. 8, pp. 677-686, 2010.

[**80**] M. Ricci, L. Senni, P. Burrascano, R. Borgna, S. Neri, M. Calderini, "Pulse-compression ultrasonic technique for the inspection of forged steel with high attenuation," *Insight Non Destructive Testing and Condition Monitoring*, vol. 52, no. 2, pp. 91-95, 2012.

[**81**] J. E. Michaels, S. J. Lee, A. J. Croxford and P. D. Wilcox, "Chirp excitation of ultrasonic guided waves," *Elsevier Ultrasonics*, vol. 53, p. 265-270, 2012.

[**82**] H. Zhang, S. Wub, D. Ta, K. Xu, W. Wang, "Coded excitation of ultrasonic guided waves in long bone fracture assessment," *Elsevier Ultrasonics*, vol. 54, no. 5, pp. 1203-1209, 2014.

[**83**] Z. Zhou, B. Maa, J. Jianga, G. Yub, K. Liub, D. Zhangb, W. Liub, "Application of wavelet filtering and Barker-coded pulse compression hybrid method to air-coupled ultrasonic testing," *Nondestructive Testing and Evaluation*, vol. 29, no. 4, pp. 297-314, 2014.

[**84**] K. Toiyama, T. Hayashi, "Pulse Compression Technique Considering Velocity Dispersion of Guided Wave," in *34th Annual Review of Progress in Quantitative Nondestructive Evaluation. AIP Conference Proceedings*, Volume 975, pp. 587-593, 2008.

[**85**] P. Cawley, D. N. Alleyne, "The use of Lamb Waves for the Long-Range Inspection of Large Structures," *Elsevier Ultrasonics*, vol. 34, no. 2, pp. 287-290, 1996.

[**86**] T. J. Terrell, L-K.Shark, Digital signal Processing: A Student's Guide, London, United Kingdom: Macmillan Press Ltd., Ch-1, pp. 10-12, 1996.

[**87**] J. Watkinson, The Art of Digital Audio, London, United kingdom: Focal Press, edn. 1, pp. 122-135, 1988.

[**88**] Mathworks, "MATLAB Mathematics: User's Guide (R2013a)," Retrieved June 10, 2013, pp. 7-20 to 7-35, from 2011. [Online]. Available: `http://www.mathworks.co.uk/help/pdf_doc/matlab/math.pdf`. [Accessed 10 June 2013].

[**89**] R. E. Crochiere, L. R. Rabiner, "Interpolation and Decimation of Digital Signals— A tutorial review," *Proceedings of the IEEE*, vol. 69, no. 3, pp. 300-330, 1981.

[**90**] P. Cawley, D. Alleyne, "Paractical long range guided wave inspection- managing complexity," Feb. 2004. [Online]. Available: `http://www.ndt.net/article/mendt03/4/4.htm`. [Accessed 10 9 2013].

[**91**] A. V. Oppenheim, R. W. Schafer, Digit Signal Processing, London, United Kingdom: Prentice Hall International Inc., edn. 1, pp. 239-242, 1975.

[**92**] P. Wilcox, M. J. S. Lowe, P. Cawley, "The Effect of Dispersion on Long-Range Inspection Using Ultrasonic Guided Waves," *NDT&E International*, vol. 34, no. 1, pp. 1-9, 2001.

[**93**] E. P. Papadakis, "Effect of multimode guided-wave propagation on ultrasonic phase velocity measurements: problem and remedy," *Journal of the Acoustical Society of America*, vol. 45, no. 6, pp. 1547-1555, 1969.

[**94**] E. Pardo, J.L. San Emeterio, M.A. Rodriguez, A. Ramos, "Noise reduction in ultrasonic NDT using undecimated wavelet transforms," *Elsevier Ultrasonics*, vol. 44, pp. 1063-1067, 2006.

[**95**] M.A. Rodriguez, J.L. San Emeterio, J.C. Lazaro, A. Ramos, "Ultrasonic flaw detection in NDE of highly scattering materials using wavelet and Wigner-Ville transform processing," *Elsevier Ultrasonics*, vol. 42, no. 9, pp. 847-851, 2014.

[**96**] B. Engineer, "The Mechanical and Resonant Behaviour of a Dry Coupled Thickness-Shear PZT Transducer used for Guided Wave Testing in Pipe Line," *Brunel University London Ph.D. thesis*, pp. 2-109, 2013.

[**97**] D. Hutchins, P. Burrascano, L.Davis, S. Laureti, M. Ricci, "Coded waveforms for optimised air-coupled ultrasonic nondestructive evaluation," *Elsevier Ultrasonics*, vol. 54, no. 7, pp. 1745-1759, 2014.

[**98**] W. B. Na, H. S. Yoon, "Wave-attenuation estimation in fluid-filled steal pipes: the first longitudinal guided wave mode," *Russian journal of nondestrcutive testing*, vol. 43, no. 8, pp. 549-554, 2007.

[**99**] R. Sanderson, S. D. Smith, "The application of finite element modelling to guided wave testing system," *Review of Quantitative Nondestructive Evaluation*, vol. 22, p. 256.263, 2003.

[**100**] K. Sezawa, "Report: Anomalous dispersion of elastic surface waves," *Earthquake Research Institute*, vol. 16, pp. 225-233, 1938.

[**101**] H. Cui, J. Trevelyan, Sh. Johnstone, "Anamalous Dispersion of Flexural Guided Waves in Clad Rods," *IEEE Transactions on Ultrasonics, Ferroelectrics, and Frequency Control*, vol. 58, no. 7, pp. 1525-1528, 2011.

[**102**] G. Edwards, "Corrosion detection in offshore risers using guided ultrasonic waves," in *26th International Conference on Offshore Mechanics and Arctic Engineering (OMAE 2007)*, San Diego, California, June, 2007.

[**103**] D. N. Alleyene, P. Cawley, "The Excitation of Lamb Waves in Pipes Using Dry-Coupled Piezoelectric Transducers," *Journal of Non-Destructive Evaluation*, vol. 15, no. 1, pp. 11-20, 1996.

[**104**] J. A. Greenwood, "On the DMT Theory," *Tribology Letters*, vol. 26, no. 3, pp. 203-204, 2007.

[**105**] K. L. Johnson, "Contact Mechanics," Cambridge, Cambridge University Press, 1987, pp. 1-468.

[**106**] D. N. Alleyne, M. J. S. Lowe, "The reflection of guided waves from circumferential notches in the pipe," *American Society of Mechanical Engineers*, vol. 65, no. 3, pp. 635 - 641, 1998.

[**107**] M. J. S. Lowe, R. E. Challis, C. W. Chan, "The transmission of Lamb waves across adhesively bonded lap joints," *The Journal of Acoustical Society of America*, vol. 107, no. 3, pp. 1333-1345, 2000.

[**108**] A. Demma, P. Cawley, M. Lowe, A. G. Roosenbrand, "The reflection of the fundamental torsional mode from cracks and notches in pipes," *The Journal of Acoustical Society of America*, vol. 114, no. 2, pp. 611-625, August 2003.

[**109**] Y. Cho , "Estimation of ultrasonic Guided Wave Mode Conversion in a plate with thickness variation," *IEEE transactions on ultrasonics ferroelectrics and frequency control*, vol. 47, no. 3, pp. 591-602, 2000.

[**110**] Y. Cho, J. L. Rose, "A boundary element solution for a mode conversion study," *The Journal of Acoustical Society of America*, vol. 99, no. 4, pp. 2097-2109, 1996.

[**111**] B. Morvan, N. Wikie-Chancellier, H. Duflo, A. Tinel, J. Duclos, "Lamb wave reflection at free edge of a plate," *The Journal of Acoustical Society of America*, vol. 113, no. 3, pp. 1417-1425, 2002.

[**112**] Y. Jiangong, W. Bin, H. Cunfu, "Guided circumferential waves in orthotropic cylindrical curved plate and the mode conversion by the end-reflection," *Elsevier Applied Acoustics*, vol. 68, no. 5, p. 594-602, 2007.

[**113**] I. Bartoli, S. D. Lanza F. L. Scalea, M. Fateh, E. Viola, "Modeling guided wave propagation with application to the long-range defect detection in railroad tracks," *NDT&E International*, vol. 38, no. 5, pp. 325-334, 2005.

[**114**] M. J. S. Lowe, D. N. Alleyne, P. Cawley, "The reflection of guided waves from circumferential notches in the pipe," *American Society of Mechanical Enginners*, vol. 65, no. 3, pp. 635-641, 1998.

[**115**] P. Cawley., D. N. Alleyne, C. W. Chan (1994) 'Inpsection of pipes', WO 96/12951, 20-10-1994.

[**116**] P.D. Wilcox, M.J.S. Lowe, P. Cawley, "Mode and Transducer Selection for Long Range Lamb Wave Inspection," *Journal of Intelligent Material Systems and Structures*, vol. 12, pp. 553-564, 2002.

[**117**] M. J. S. Lowe, P. Cawley, "Long Range Guided Wave Inspection Usage - Current Commercial Capabilities and Research Directions," Department of Mechanical Engineering, Imperial College, London, 2006.

[**118**] J. L. Rose, "Ultrasonic Guided Waves in Structural Health Monitoring," *Key Engineering Materials*, Vols. 270-273, pp. 14-21, 2004.

[**119**] J. L. Rose, "An Introduction to Ultrasonic Guided Waves," in *4th Middle East NDT Conference and Exhibition*, Kingdom of Bahrain, Dec. 2007.

[**120**] P. Cawley and D. N. Alleyne, "Paractical long range guided wave inspection-managing complexity," Feb. 2004. [Online]. Available: http://www.ndt.net/article/mendt03/4/4.htm. [Accessed 09 10 2013].

[**121**] D. E. Oliver, "Tutorial: 3D Scanning Vibrometery for Structural Dynamics Measurements," Polytec, Hamburg, Germany, 2007.

[**122**] R. Behrendt, S. Heuer, H. Steger, "3D Scanning Laser Vibrometry," Polytec, Hamburg, Germany, 2005.

[**123**] Plant Integrity Ltd., "Teletest LRUT operator level 1 training manual notes," Pi Ltd., Cambridge, England, 2009.

[**124**] J-W. Cheng, S-K Yang, P-H.Lee, C-J. Huang, "Attenuation of Guided Wave Propagation by the Insulation Pipe," Available from: http://www.intechopen.com/books/petrochemicals/

attenuation-of-guided-wave-propagation-bythe-   Petrochemicals, Dr Vivek Patel (Ed.), ISBN: 978-953-51-0411-7, InTech. [Online].

[**125**] BS EN 583-1, Non-destructive testing - Ultrasonic examination - Part 2: Basic requirements for guided wave testing of pipes, pipelines and structural tubulars.

[**126**] A. Demma, D. N. Alleyne , "Guided Waves: Standardization and Certification," in *6th International Conference on Certification and Standardization NDT* , Valencia, Spain, June 13th - 14th, 2011.

Appendix A

Additional results for Chapter 4

As was highlighted in Chapter 4, Section 4.3 & 4.4, 512 frequencies were synthesized and experimented respectively. Three chosen/sample frequencies before and after sampling rate conversion are illustrated here. The Figures A.1 to A.14 illustrate the effect of sampling rate conversion in time domain and Fourier domain (synthesis and experimental). It can be observed that after sampling rate conversion, beyond f_0, 20 kHz, the UGW signals experience different shifts in time domain and their frequency converts back to f_0, 20kHz.

A.1 Effect of Sampling Rate Conversion, Signal Synthesis
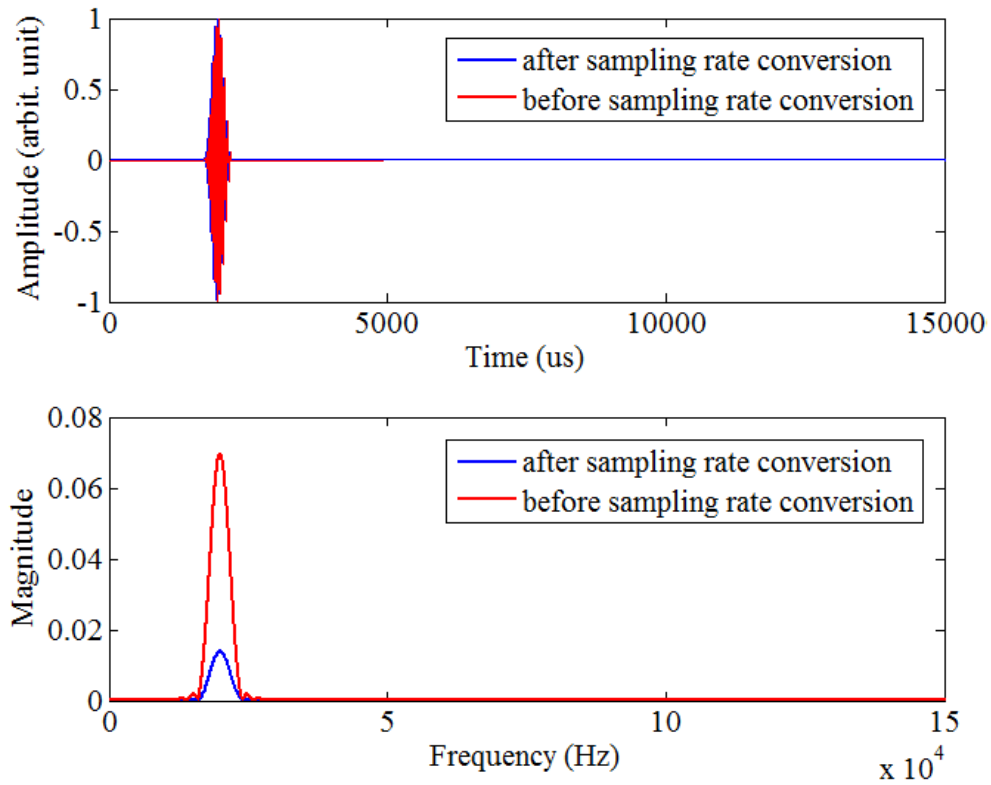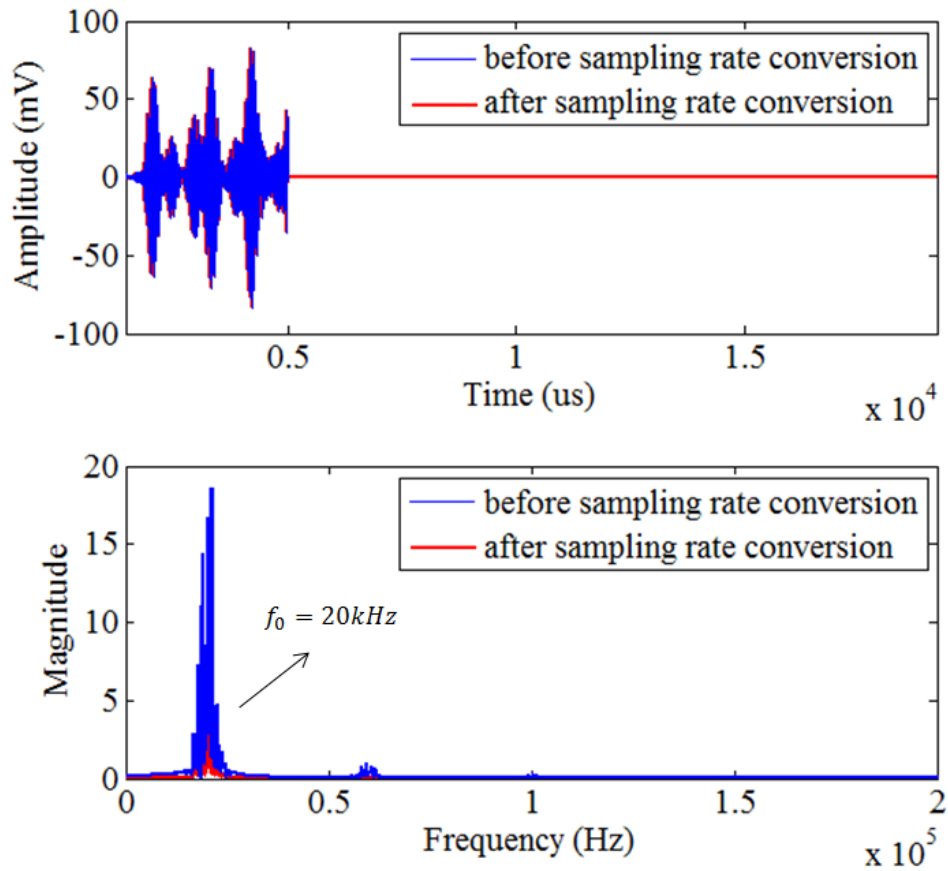

Figure A.1: Before and after sampling rate conversion of synthesized L(0,1) wave mode where the operating centre frequency is 20 kHz. (top) time domain response, (bottom) frequency domain of (top).
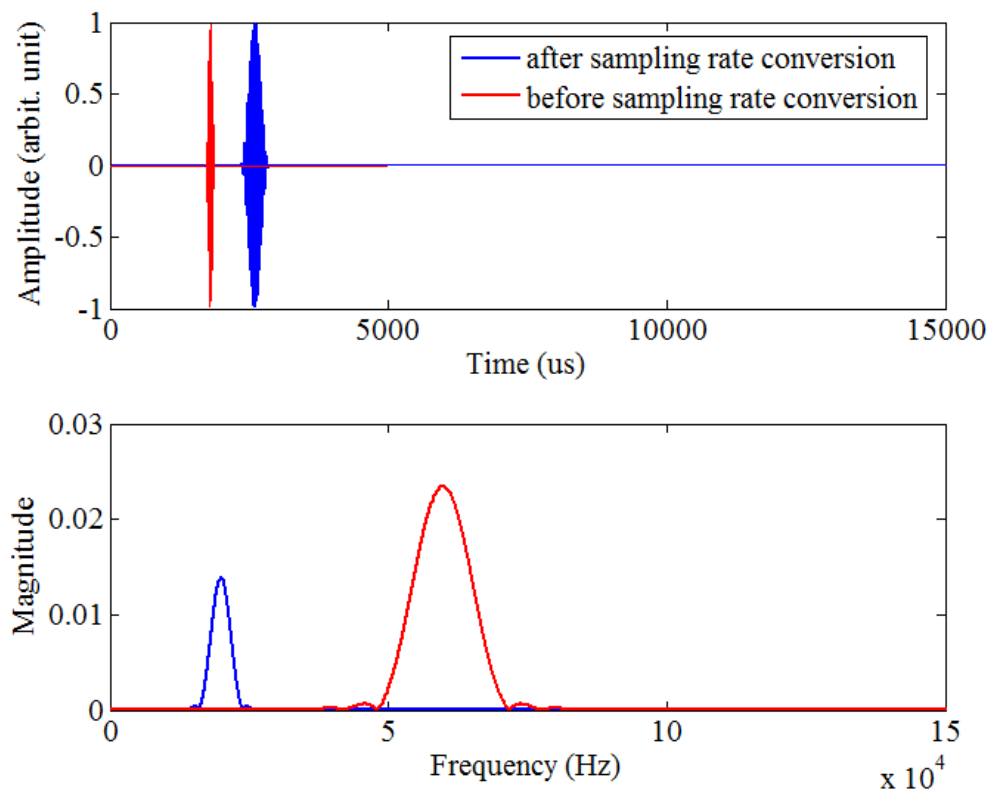
Figure A.2: Before and after sampling rate conversion of synthesized L(0,1) where the operating centre frequency is 60 kHz. (top) time domain response, (bottom) frequency domain of (top)
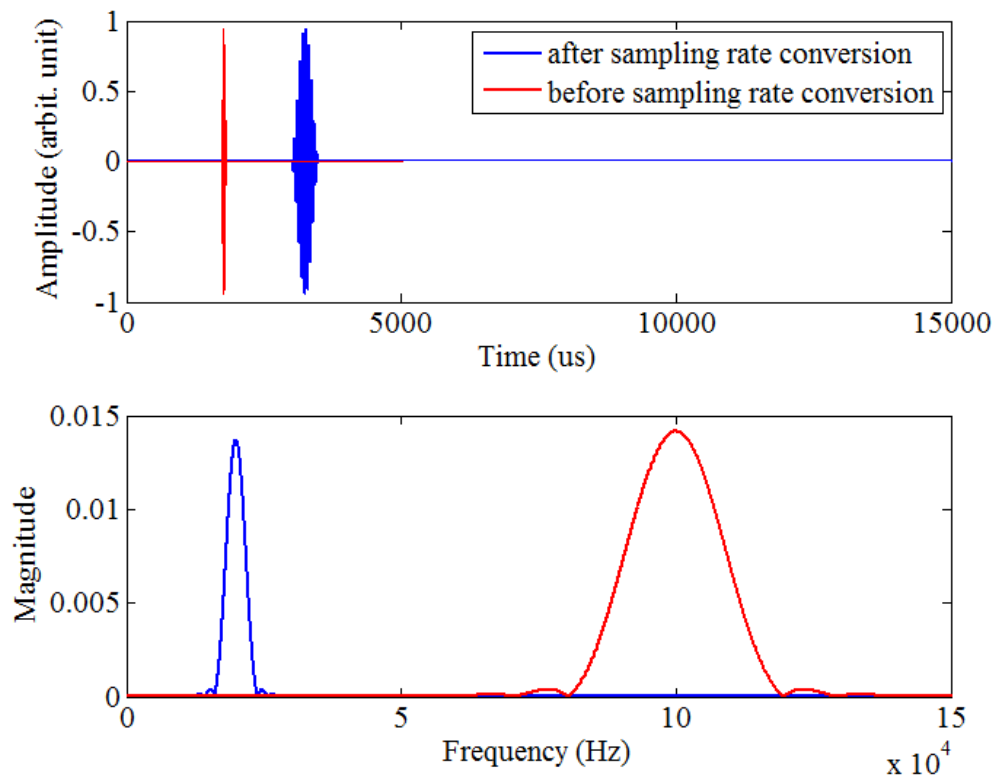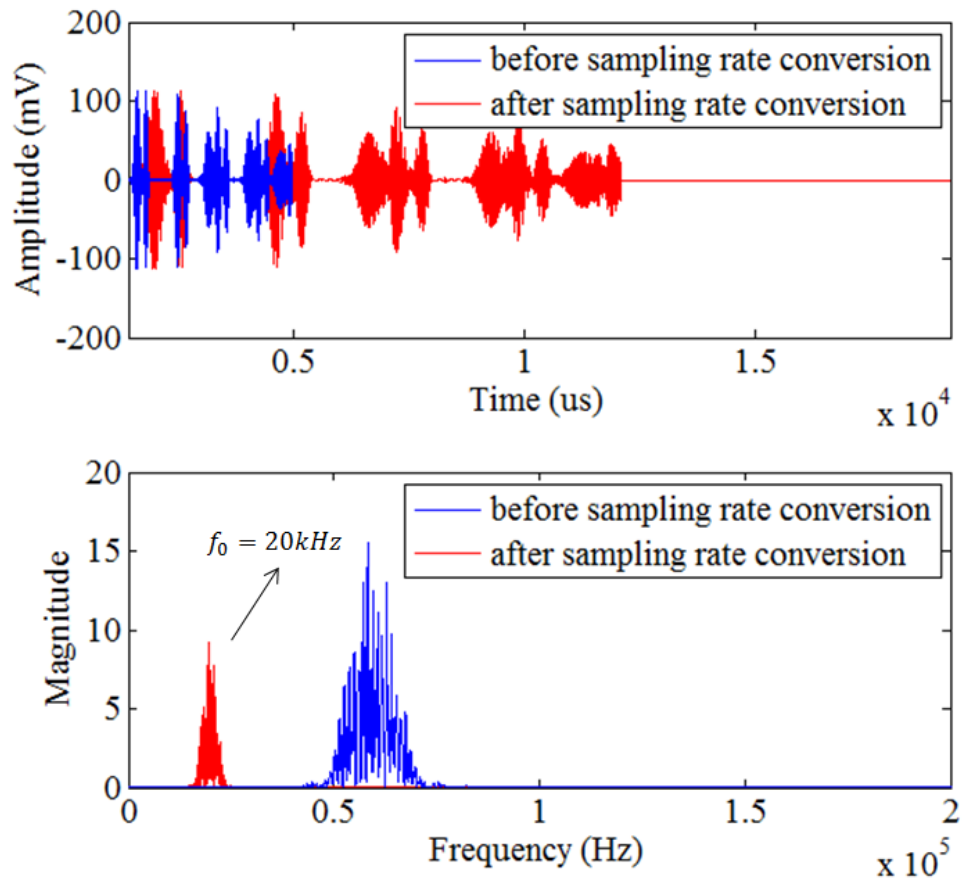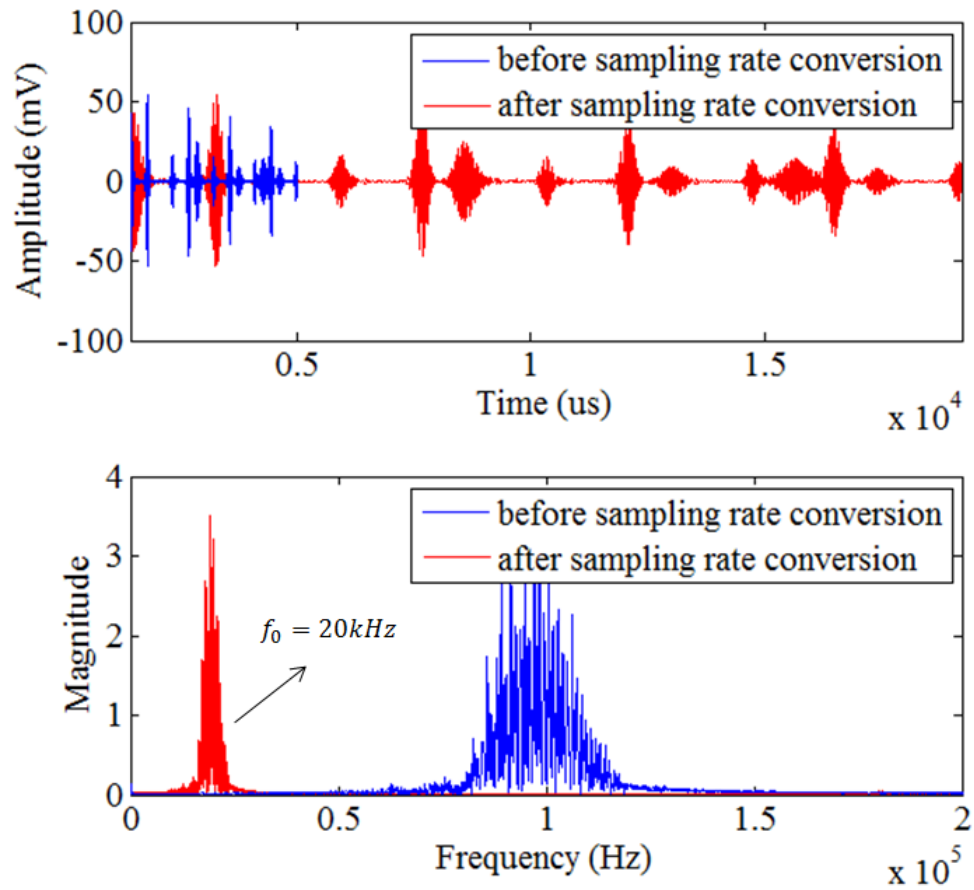
Figure A.3: Before and after sampling rate conversion of synthesized L(0,1) where the operating centre frequency is 100 kHz. (top) time domain response, (bottom) frequency domain of (top)
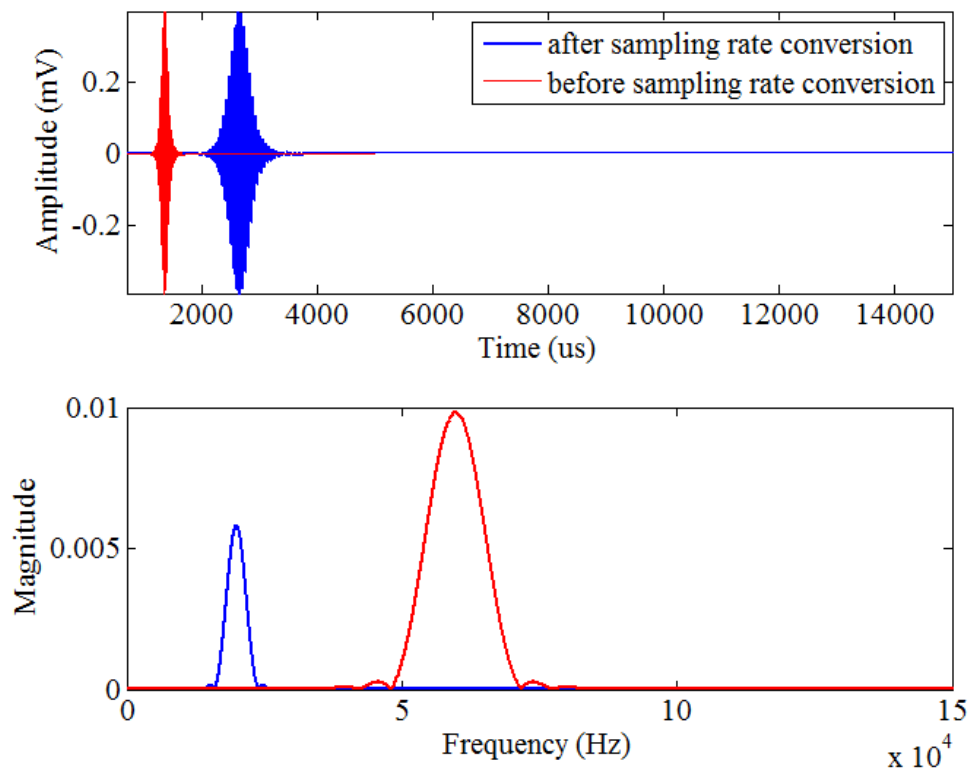
Figure A.4: Before and after sampling rate conversion of synthesized F(1,1) wave mode where the operating centre frequency is 60 kHz. (top) time domain response, (bottom) frequency domain of (top)
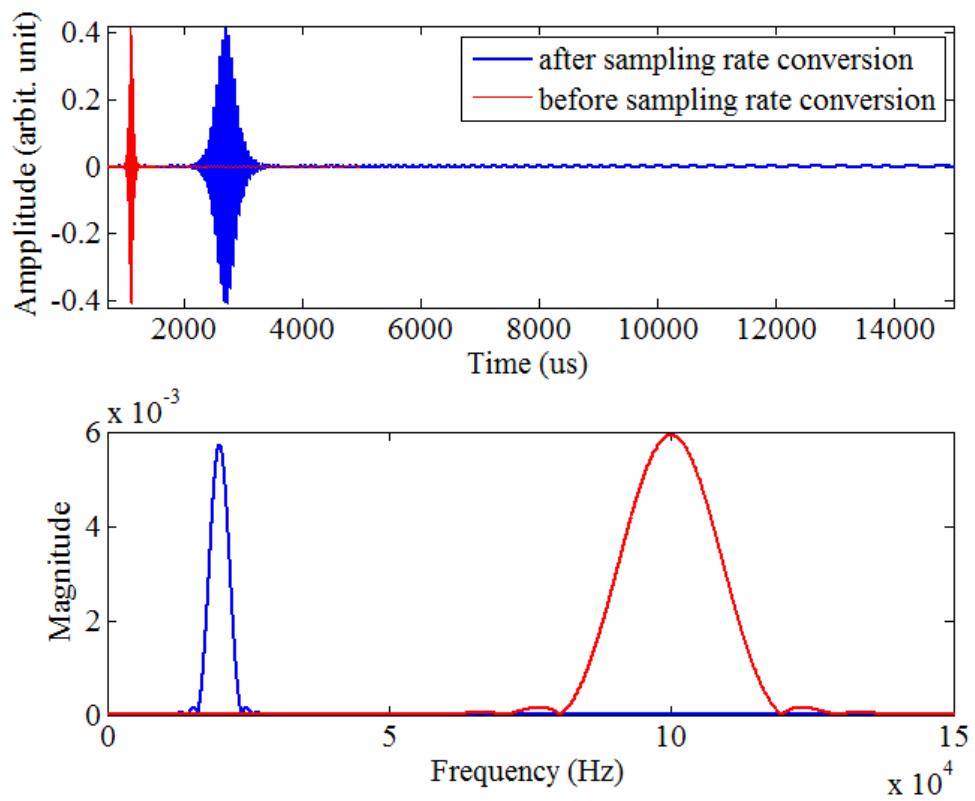
Figure A.5: Before and after sampling rate conversion of synthesized F(1,1) wave mode where the operating centre frequency is 100 kHz. (top) time domain response, (bottom) frequency domain of (top)

A.2 Effect of Sampling Rate Conversion, Experimental result

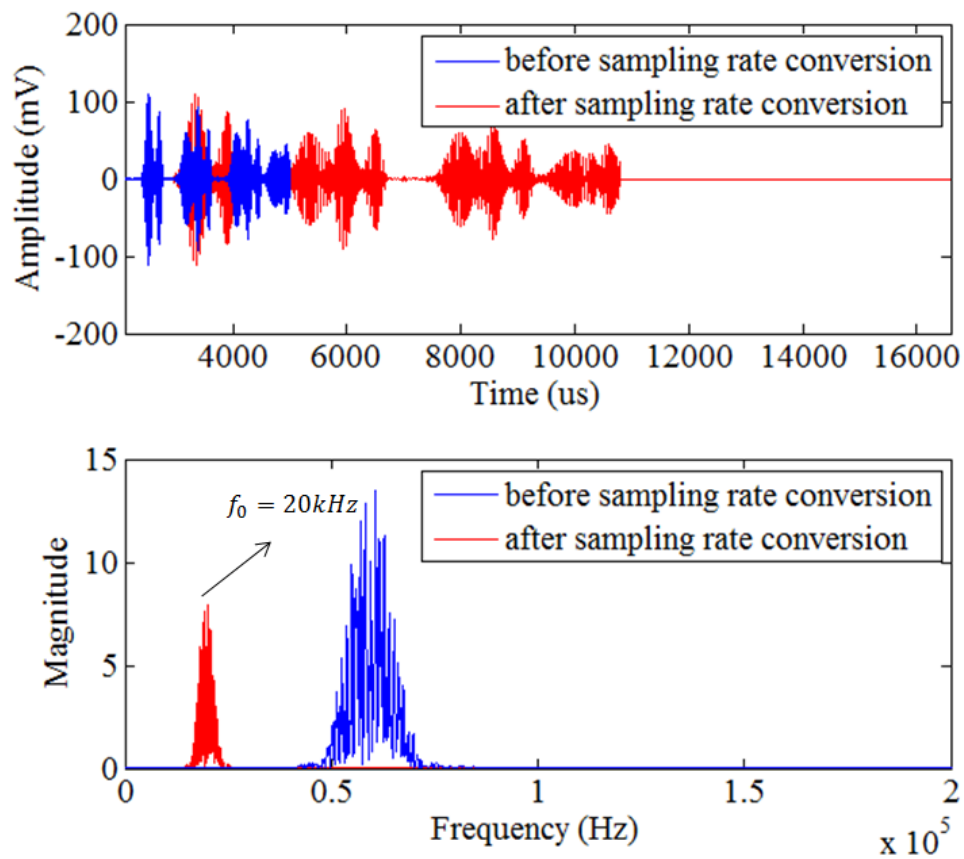When the application of sampling rate conversion is in the range of $[860\mu s : 5000\mu s]$:
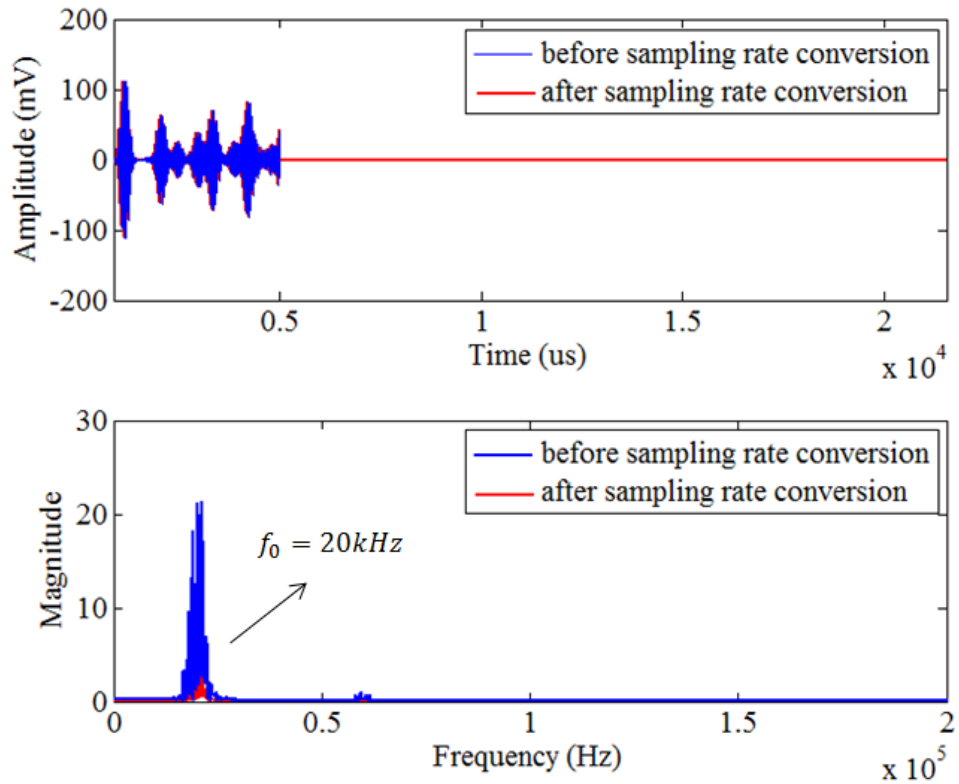
Figure A.6: Before and after sampling rate conversion of experimental acquisition where the operating centre frequency is 20 kHz. (top) time domain response, (bottom) frequency domain of (top)
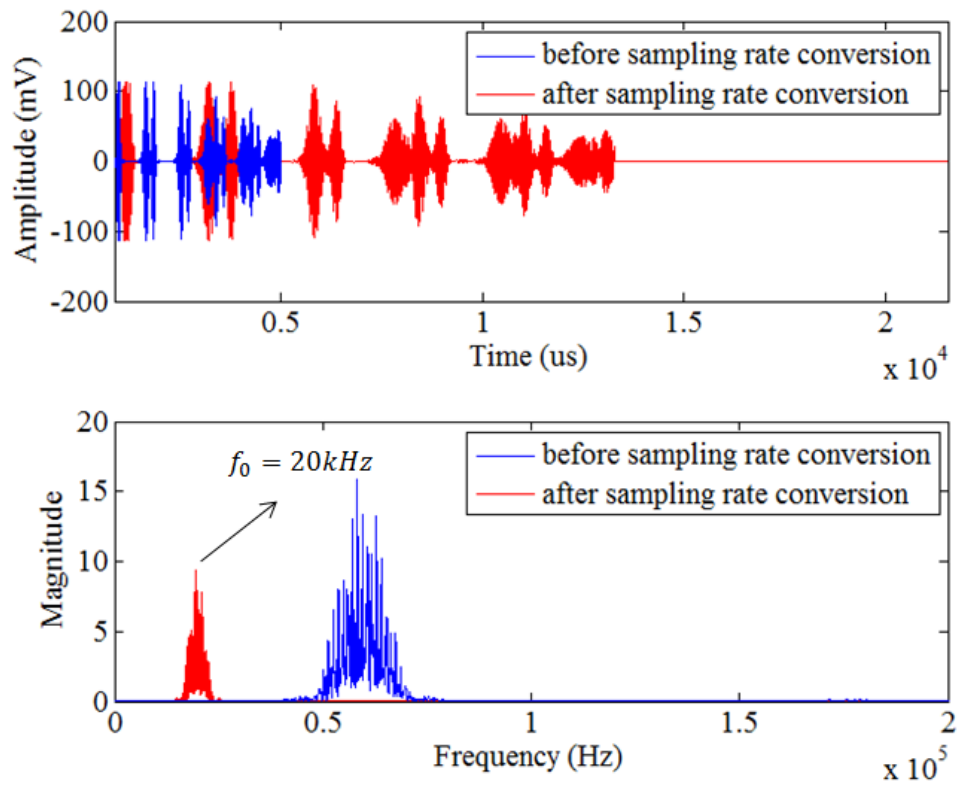
Figure A.7: Before and after sampling rate conversion of experimental acqusition where the operating centre frequency is 20 kHz. (top) time domain response, (bottom) frequency domain of (top)
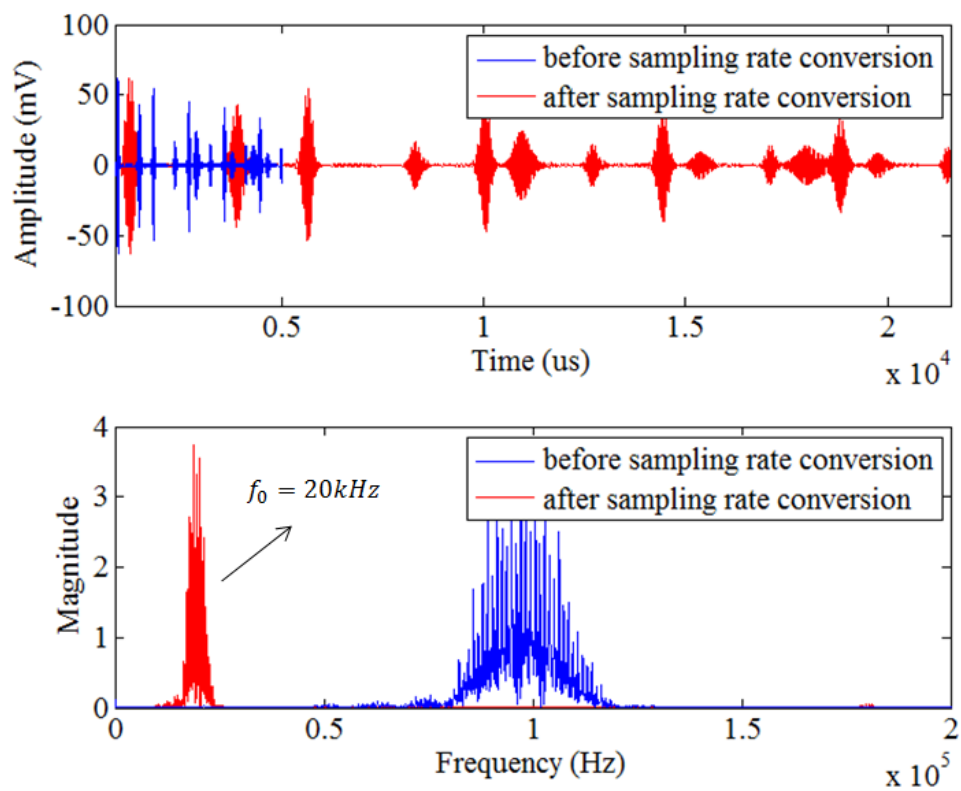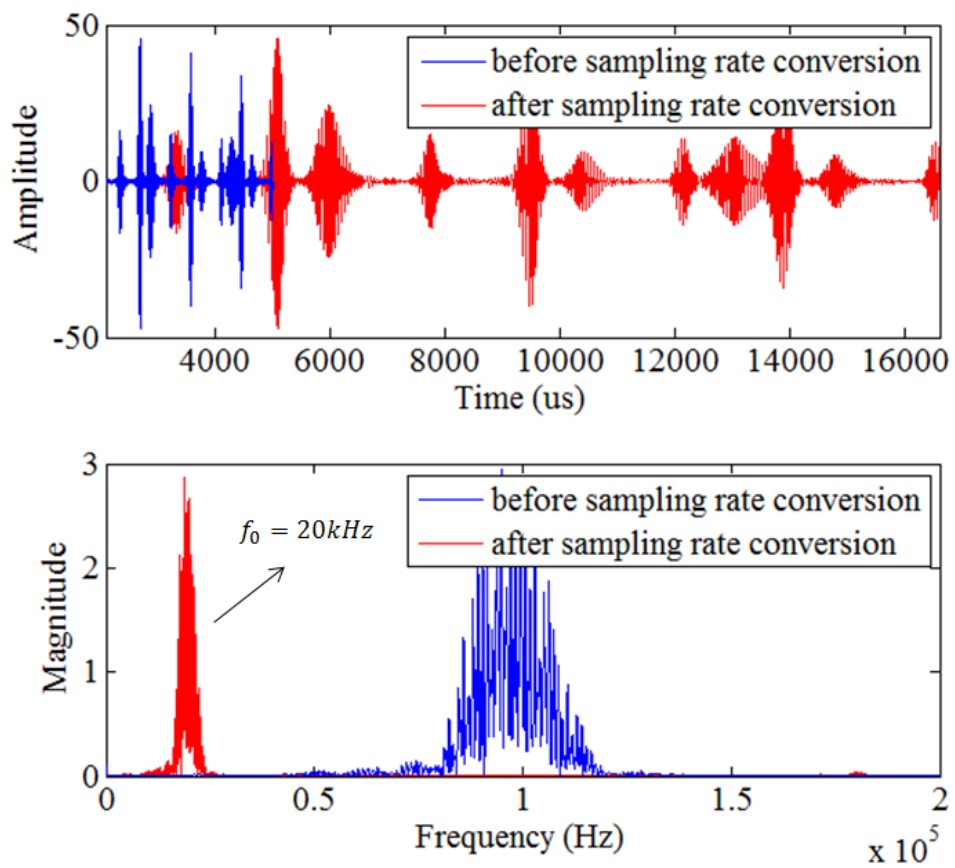
Figure A.8: Before and after sampling rate conversion of experimental acquisition where the operating centre frequency is 100 kHz. (top) time domain response, (bottom) frequency domain of (top)

When the application of sampling rate conversion is in the range of $[1450 \mu s : 5000 \mu s]$:

Figure A.9: Before and after sampling rate conversion of experimental acquisition where the operating centre frequency is 20 kHz. (top) time domain response, (bottom) frequency domain of (top)

Figure A.10: Before and after sampling rate conversion of experimental acquisition where the operating centre frequency is 60 kHz. (top) time domain response, (bottom) frequency domain of (top)

Figure A.11: Before and after sampling rate conversion of experimental acquisition where the operating centre frequency is 100 kHz. (top) time domain response, (bottom) frequency domain of (top)

When the application of sampling rate conversion is in the range of $[1450\mu s : 2100\mu s]$:
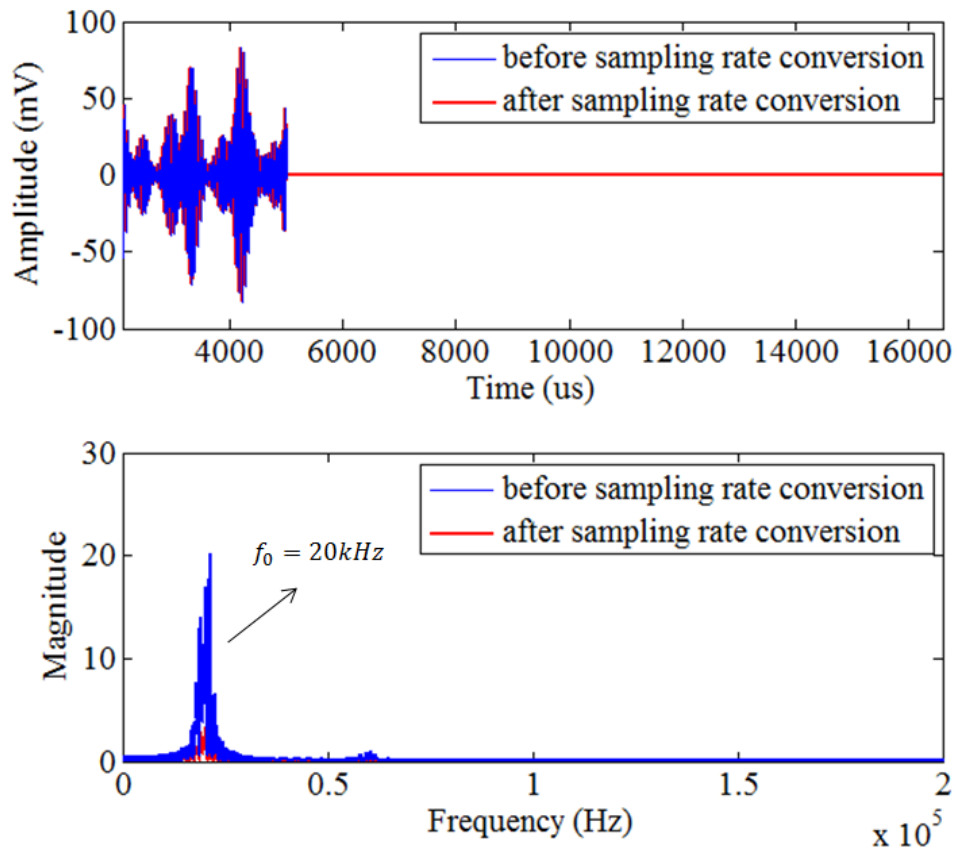
Figure A.12: Before and after sampling rate conversion where the operating centre frequency is 20 kHz. (top) time domain response, (bottom) frequency domain of (top)

Figure A.13: Before and after sampling rate conversion of experimental acquisition where the operating centre frequency is 60 kHz. . (top) time domain response, (bottom) frequency domain of (top)

Figure A.14: Before and after sampling rate conversion of experimental acquisition where the operating centre frequency is 100 kHz. (top) time domain response, (bottom) frequency domain of (top)

Appendix B

Additional results for Section 6.5.1

Results obtained using FSE and IDC based pulse compression techniques

Based on the setup described in Figure 6.8, the response coming from the aluminium rod under investigation were heavily superposed and could not be directly identified in the frequency range of 20 to 60 kHz. The responses are illustrated in Figure B.1 & B.2. Therefore the presences of the mode converted signal have been identified with the aid of the signal processing techniques developed in previous chapters (FSE in Chapter 4 and IDC in Chapter 5) as shown in Figures B.3 to B.10.
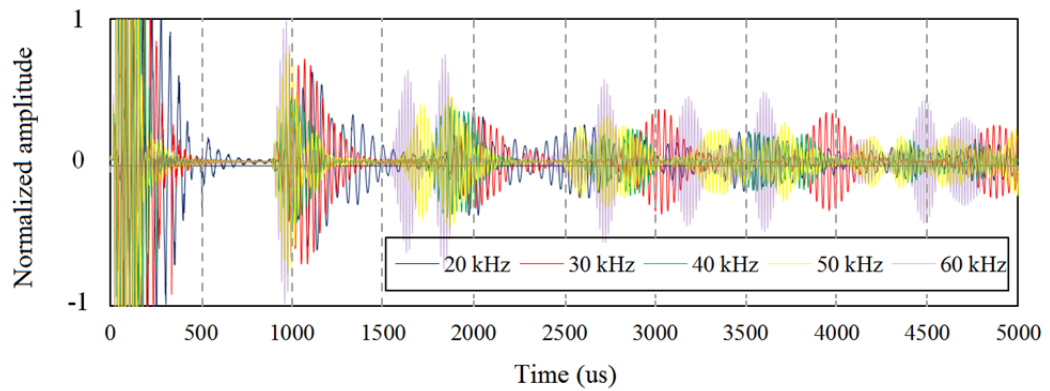
Figure B.1: Sample UGW response for different centre frequencies (narrowband)
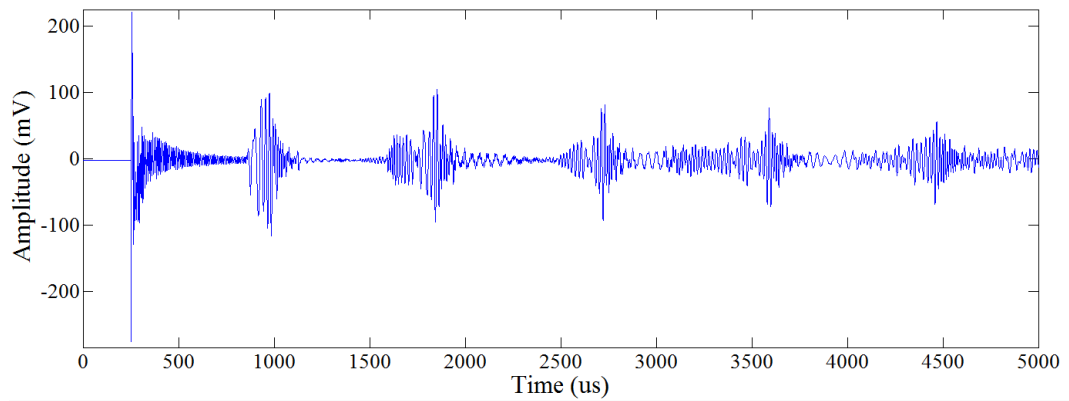
Figure B.2: Sample UGW response (broadband)

30 kHz centre frequency:
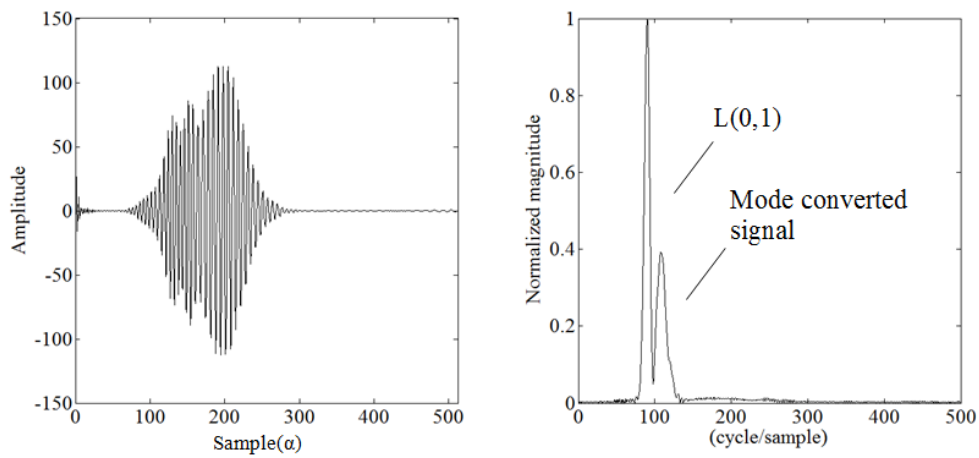
Figure B.3: FSE: a sample (left) ASW and (right) FSS for 30 kHz, illustrating identified L(0,1) wave mode and the mode converted signal.
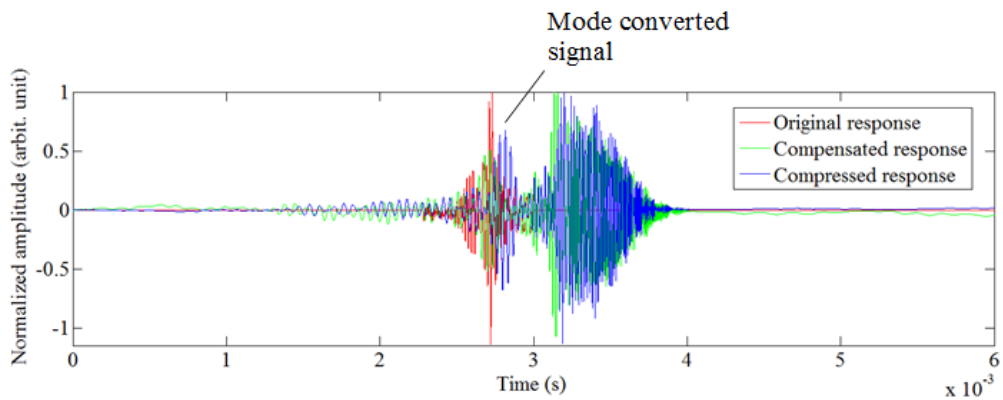
Figure B.4: IDC: Identification of the mode converted signal at 30 kHz.
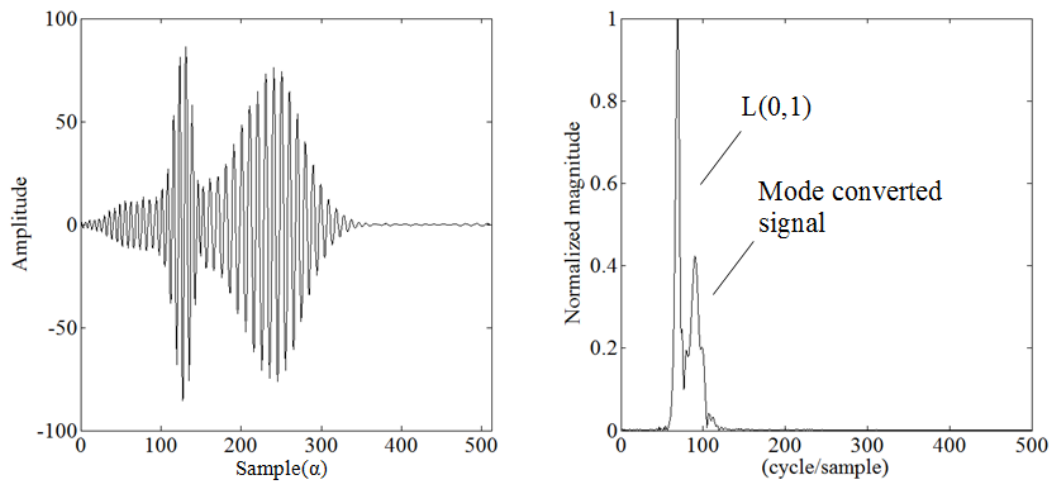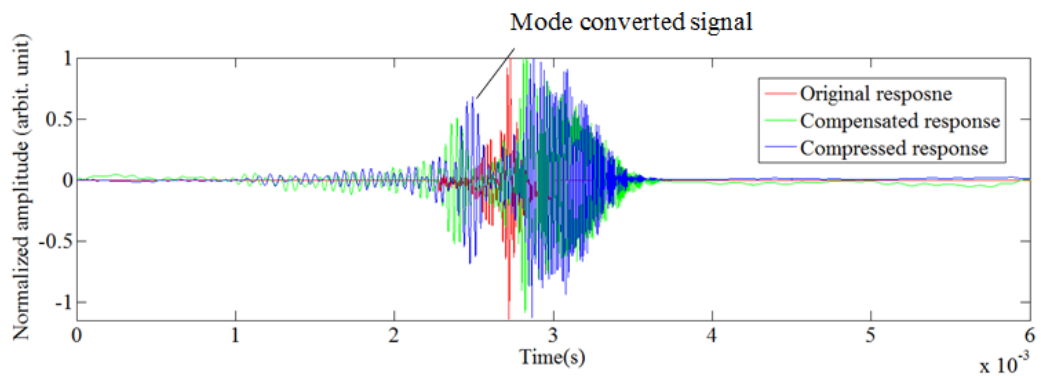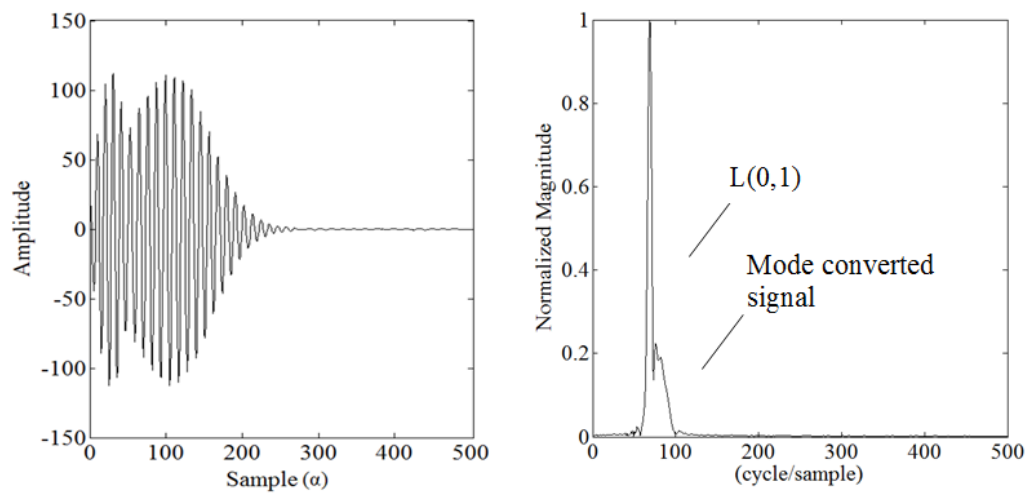
40 kHz centre frequency:

Figure B.5: FSE: a sample (left) ASW and (right) FSS for 40 kHz, illustrating identified L(0,1) wave mode and the mode converted signal.
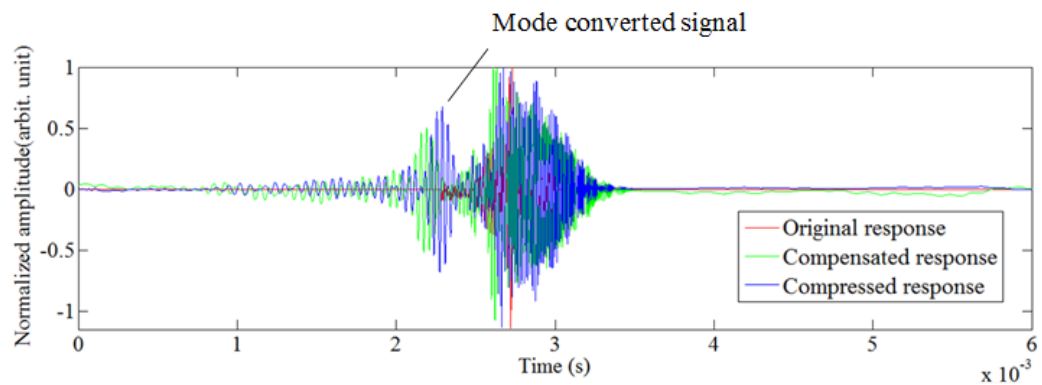

Figure B.6: IDC: Identification of the mode converted signal at 40 kHz.
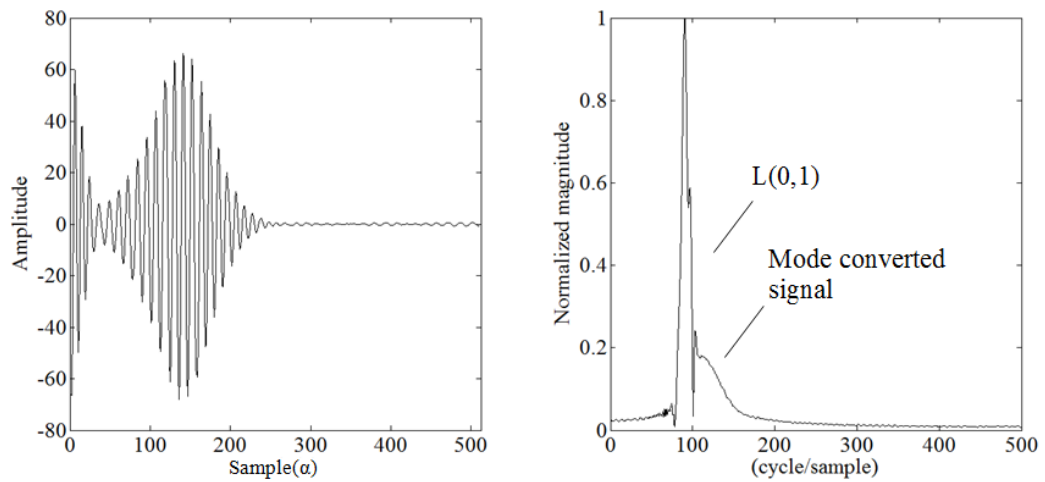
50 kHz centre frequency:

Figure B.7: FSE: a sample (left) ASW and (right) FSS for 50 kHz illustrating identified L(0,1) wave mode and the mode converted signal.

Figure B.8: IDC: Identification of the mode converted signal at 50 kHz.

60 kHz centre frequency:

Figure B.9: FSE: a sample (left) ASW and (right) FSS for 60 kHz illustrating identified L(0,1) wave mode and the mode converted signal.
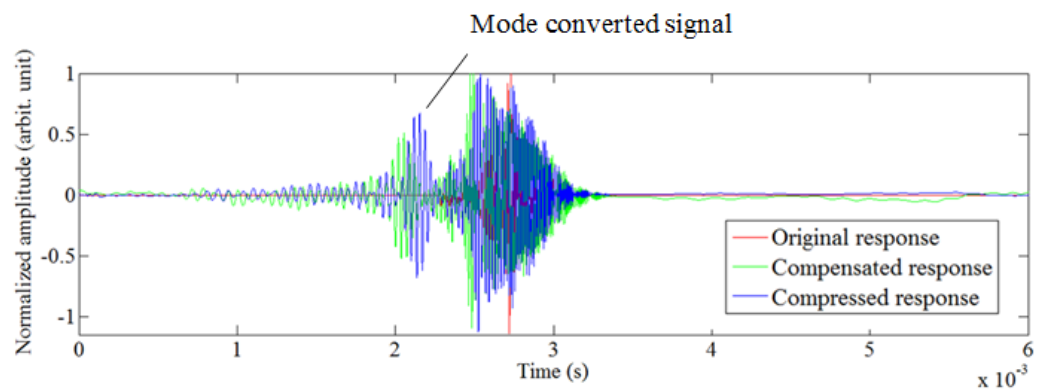

Figure B.10: IDC: Identification of the mode converted signal at 60 kHz.

Appendix C

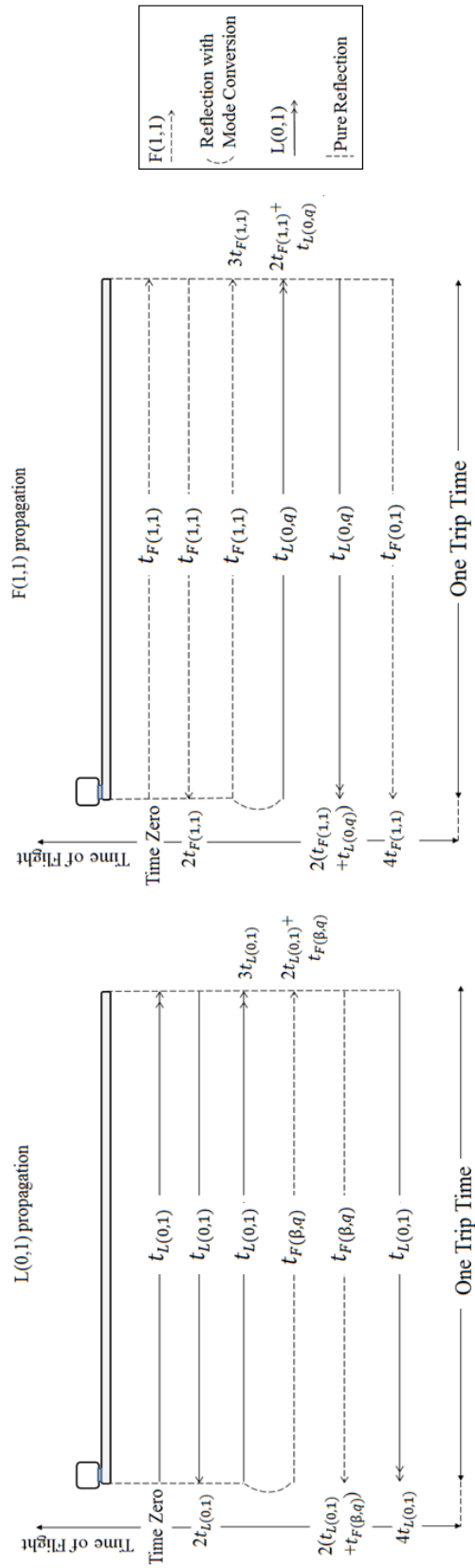# Travel path of the L(0,q) and F(β,q) wave modes when interacting with the piezoelectric transducer

Figure C.1: Time of Arrival analysis of the the wave modes of interest propagating in the rod and predicting the ToA of the mode converted signals, L(0,q) & F(β,q).

"Nothing in the world is granted to someone for free. Humans spend money for their needs. They spend time and express gratitude to others in order to gain honour.

You spent four years of your life, youth, emotions, being far from your beloved family and friends at home to claim expertise in the field that you are interested in and pave the way to success in life."

<div align="right">

Mr. Manouchehr Fateri,
A fatherly advice to his son

</div>